People's Democratic Republic of Algeria
Ministry of Higher Education and Scientific Research
University of El Oued
Faculty of Technology
Department of Processes Engineering and Petrochemicals

Submitted in partial fulfilment of the requirements for the degree of

LMD doctorate

Specialty: Chemical Engineering

Option: Pharmaceutical Engineering

Titled

Optimisation des Conditions D'élaboration d'une Electrode Modifié Verre ITO/ Semi-Conducteur /Dérivés Ferrocèniques

Submitted by

Gamil Gamal Qasem Hasan

Graduation Data: 14 November 2024

Composition of the jury

Khelef Abdelhamid	**Pr**	**University of El Oued**	**Supervisor**
Adel Sakri	**Pr**	**University of Biskra**	**Examiner**
Hachemi Ben Temam	**Pr**	**University of Biskra**	**Examiner**
Abdelghani Serouti	**MCA**	**University of El Oued**	**Examiner**
Ferhat Mohammed Fouad	**Pr**	**University of El Oued**	**President**
Laouini Salah Eddine	**Pr**	**University of El Oued**	**Invited**

2024/2025

People's Democratic Republic of Algeria
Ministry of Higher Education and Scientific Research
University of El Oued
Faculty of Technology
Department of Processes Engineering and Petrochemicals

Submitted in partial fulfilment of the requirements for the degree of

LMD doctorate

Specialty: Chemical Engineering

Option: Pharmaceutical Engineering

Titled

Optimisation des Conditions D'élaboration d'une Electrode Modifié Verre ITO/ Semi-Conducteur /Dérivés Ferrocèniques

Submitted by

Gamil Gamal Qasem Hasan

Graduation Data: 14 November 2024

Composition of the jury

Khelef Abdelhamid	**Pr**	**University of El Oued**	**Supervisor**
Adel Sakri	**Pr**	**University of Biskra**	**Examiner**
Hachemi Ben Temam	**Pr**	**University of Biskra**	**Examiner**
Abdelghani Serouti	**MCA**	**University of El Oued**	**Examiner**
Ferhat Mohammed Fouad	**Pr**	**University of El Oued**	**President**
Laouini Salah Eddine	**Pr**	**University of El Oued**	**Invited**

2024/2025

Dedication

To my family and friends, whose unwavering support, encouragement, and belief in me have been my greatest source of strength.

To my mentors, whose wisdom, guidance, and inspiration have shaped my journey.

And to all the dreamers and innovators, may this work serve as a humble contribution toward a brighter and more promising future.

Acknowledgements

I would like to begin by expressing my gratitude to Prof. Khelef Abdelhamid for his unwavering support throughout my years as a PhD student. As my supervisor, he not only made this dissertation possible but also nurtured my growth as a scientist within his group. I am also deeply thankful to Chabiaa Nacer for the invaluable discussions; it has been an honor to work with such an exceptional chemist. I extend my heartfelt thanks to Prof. Laouini Salah Eddine for his significant scientific contributions and to Prof. Touhami Lanez for his assistance on countless occasions.

I owe my warmest thanks to the members of the BBCM and VTRS laboratories. I had the privilege of meeting many fantastic individuals and superb scientists, each of whom taught me something valuable. In particular, I want to thank Mohammed Althamthami, who was one of the first to mentor my work; I am deeply grateful for all I have learned from him.

A special thanks to my lab mates over the years, especially Hamdi Ali Mohammed, who supported me through this four-year journey.

To all my friends, both those I met in EL Oued and those I left in Biskra, thank you. Your presence made this journey meaningful. Lastly, I extend my deepest appreciation to my father for his unconditional support and his contribution to this thesis with a beautiful layout. To my mother and siblings, thank you as well.

Abstract

This work aims to improve the conditions for the development of a modified electrode based on indium tin oxide (ITO) glass / semiconductors / ferrocene derivatives. It falls within the field of material chemistry, a domain that focuses on the development of materials and their applications, particularly in photovoltaic cells, due to their connections with several sectors such as organometallics, semiconductors, superconductors, ceramics, glass, and optical fibers.

A modified electrode of indium tin oxide, semiconductors, and ferrocene derivatives was designed and applied to evaluate its potential in energy and environmental applications. For this purpose, silver nanoparticles were deposited on ITO glass using the cyclic voltammetry technique at different scan speeds to achieve optimal optical and electrical properties. The formation of a uniform silver crystalline layer with high light transmission properties in the visible range was confirmed by various characterization techniques such as SEM (scanning electron microscopy), XRD (X-ray diffraction), FTIR (Fourier-transform infrared spectroscopy), and UV-Vis (UV-visible spectroscopy). Electrochemical results showed that deposition rates were higher at lower scan rates.

A thin layer of N-(ferrocenylmethyl) aniline (NFMA) was also fabricated on fluorine-doped tin oxide (FTO) glass using two methods (immersion and electrochemical deposition). The results showed an amorphous structure with a uniform distribution of particles, which conferred favorable optical properties and significant hydrophobicity. The fabricated electrode also demonstrated efficiency in the decomposition of hydrogen peroxide into H_2O and O_2, as well as in the degradation of methylene blue under solar irradiation.

Finally, a thin layer of NFMA was electrochemically developed on a thin Cu_2O/ITO layer. The results showed an amorphous structure with a uniform particle distribution and promising optical properties. The electrode also demonstrated high efficiency in the degradation of Rose Bengal under solar irradiation.

Keywords

Ferrocene derivatives, thin film, modified electrode, ITO, photovoltaic.

Résumé

Ce travail vise à améliorer les conditions d'élaboration d'une électrode modifiée à base de verre d'oxyde d'indium-étain (ITO) / semi-conducteurs / dérivés ferrocènique. Il s'inscrit dans le cadre de la chimie des matériaux, un domaine qui se concentre sur le développement des matériaux et leurs applications, notamment dans les cellules photovoltaïques, en raison de leurs liens avec plusieurs secteurs, tels que les organométalliques, les semi-conducteurs, les supraconducteurs, les céramiques, les verres et les fibres optiques.

Une électrode modifié d'oxyde d'indium-étain, semi-conducteurs et les dérivés ferrocènique a été conçue et appliquée pour évaluer son potentiel dans des applications liées à l'énergie et à l'environnement. Pour cela, des nanoparticules d'argent ont été déposées sur du verre ITO en utilisant la technique de voltampérométrie cyclique à différents vitesse de balayage afin d'obtenir des propriétés optiques et électriques optimales. La formation d'une couche cristalline uniforme en argent avec des propriétés de transmission lumineuse élevées dans le domaine du visible a été confirmée par diverses techniques de caractérisation, telles que la MEB (microscopie électronique à balayage), la DRX (diffraction des rayons X), la FTIR (spectroscopie infrarouge à transformée de Fourier) et l'UV-Vis (spectroscopie UV-visible). Les résultats électrochimiques ont montré que les taux de dépôt étaient plus élevés à des vitesses de balayage plus faibles.

Une couche mince de N-(ferrocenylméthyl) aniline (NFMA) a également été fabriquée sur du verre d'oxyde d'indium dopé au fluor (FTO) en utilisant deux méthodes (immersion et dépôt électrochimique). Les résultats ont montré une structure amorphe avec une distribution uniforme des particules, ce qui a conféré des propriétés optiques favorables et une forte hydrophobicité. L'électrode élaborée a également montré une efficacité dans la décomposition du peroxyde d'hydrogène en H_2O et O_2, ainsi que dans la dégradation du bleu de méthylène sous irradiation solaire.

Enfin, une couche mince de NFMA a été développée par méthode électrochimique sur une couche mince de Cu_2O/ITO. Les résultats ont montré une structure amorphe avec une distribution uniforme des particules et des propriétés optiques prometteuses. L'électrode a également démontré une grande efficacité dans la dégradation du rose bengale sous irradiation solaire.

Mots clé

Dérivés ferrocéniques, couche mince, électrode modifié, ITO, photovoltaïque.

ملخص

يهدف هذا العمل الى تحسين ظروف تصنيع قطب كهربائي معدّل من زجاج أكسيد القصديرالإنديوم (ITO) /أشباه الموصلات/مشتقات الفيروسين والذي يندرج ضمن تخصص كيمياء المواد الذي يهتم بتطوير المواد وتطبيقاتها خصوصا في الخلايا الكهروضوئية وذلك نظرا لارتباطها بعدة مجالات نذكر منها: العضويه معدنيه، أشباه الموصلات، الموصلات الفائقة، السيراميك، الزجاج، والألياف البصرية.

تم تصميم وتطبيق قطب كهربائي يدمج بين أكسيد الإنديوم والقصدير ، أشباه الموصلات، ومشتقات الفيروسين لتقييم إمكانياته في التطبيقات المتعلقة بالطاقة والبيئة.، لذلك قمنا بترسيب جسيمات الفضة النانوية على زجاج ITOباستخدام تقنية الفولتامتري الحلقي بمعدلات مسح مختلفة من اجل الوصول الى خصائص بصرية وكهربائية مثلى. تم التحقق من تكوين طبقة بلورية فضية احادية ذات خصائص نقل ضوئي عالية في نطاق الضوء المرئي باستخدام تقنيات توصيف متعددة مثلSEM ، XRD، FTIR، و .UV-Vis كما أشارت النتائج الكهروكيميائية إلى أن معدلات الترسيب كانت أعلى عند تقليل معدلات المسح.

كما تم تصنيع طبقة رقيقة من-N (فيروسينيل ميثيل) أنيلين (NFMA) على زجاج أكسيد القصدير المطعّم بالفلور (FTO) باستخدام طريقتين (الغمر والترسيب الكهروكيميائي). أظهرت النتائج هيكلاً غير متبلور مع توزيع موحد للجسيمات والذي اعطى خصائص بصرية ملائمة وميزة كارهة للماء بشكل كبير. كما أظهر القطب المصنع فعالية في التحفيز الكهروكيميائي لتحلل بيروكسيد الهيدروجين إلى H_2O وO_2 ، وكذلك في تحلل صبغة الميثيلين الأزرق تحت إشعاع الشمس.

اخيرا تم تطوير طبقة رقيقة بطريقة كهروكيميائية من NFMA على طبقة رقيقة من Cu_2O/ITO حيث أظهرت النتائج هيكلاً غير متبلور وتوزيعًا موحدًا للجسيمات مع خصائص بصرية واعدة كما أظهر القطب فعالية كبيرة في تحلل صبغة روز بنغال تحت إشعاع الشمس.

الكلمات المفتاحية

المشتقات الفيروسينية ، أغشية رقيقة ، قطب معدل . ITO ، خلايا كهروضوئيه.

.

Table of Contents

List of Figures

List of Tables

Statement of Original Authorship

This thesis has not been previously submitted for any awards at this or any other higher education institution. As far as I know and believe, the thesis does not include any content that has been previously published or written by someone else, except where due reference is made.

Signature: Gamil Gamal Qasem Hasan

Date: October 4th, 2024

Introduction General

Introduction General

Nanoparticles are nanoscale solid particles composed of pure metals or their compounds, typically synthesized through chemical or mechanical techniques [1]. Among various nanomaterials, metal nanoparticles have garnered attention for their potential applications in flexible devices, where their electrical and optical properties could contribute to the development of transparent conductors. Flexible devices offer enhanced adaptability for everyday use due to their lightweight, affordability, and ease of storage and transport. However, developing transparent conductors that combine optical transparency with electrical conductivity remains challenging. Key materials under investigation include ITO, FTO, Aluminium Zinc Oxide (AZO), carbon nanotubes, silver nanowires, graphene, metal networks, and graphene oxide[2-4].

Among the discussed electrodes, ITO thin films are the most effective transparent conducting materials, widely used in commercial devices due to their low sheet resistance of 10 ohms/sq., over 90% optical transmittance, and uniformity across large areas. However, ITO films face limitations in high-performance flexible electronic devices, as they can increase electrical resistance and reduce overall performance. [5, 6]. The conductivity of semiconductors allows movement in response to an electric field. ITO thin films are recognized as highly degenerate n-type semiconductors[7].

Deposition methods include spraying, evaporation, dip coating, chemical vapor deposition, and spin coating[8-12], with electrodeposition being the most cost-effective, productive, and versatile[12]. The material offers a wide electrochemical potential range, high-temperature stability, and low toxicity. Using aqueous solutions simplifies electrochemical testing, allowing plating baths to operate at various concentrations and temperatures without toxic fumes. Silver is widely used in sensors, microelectronics, jewellery, and antimicrobial applications[13, 14].

Despite a decade of research on nanoscale materials using conventional inorganic semiconductors like metal oxides[15], chalcogenides [16], and silicon [17], performance goals remain unmet. The challenge lies in finding semiconductors with high efficiency, cost-effectiveness, stability, scalability, optoelectronics, and tunability[18, 19]. Organic semiconductors (OSs) with π-conjugation offer a solution

due to their ability to be organized at the molecular level[20, 21], enabling precise control of processability and optoelectronic properties, allowing cost-effective production of high-performance devices[22]. The interaction between OSs and liquid electrolytes is important in applications like photocatalytic reactors, electrochemical instruments, and photoelectrochemical cells[23-25].

Ferrocene derivatives are standard systems due to ferrocene's structural stability, ease of modification via reversible single electron transfer (Fc^{+}/Fc), low oxidation/reduction potential, and the simple organization of self-assembled monolayers (SAMs) [26, 27]. Ferrocene easily oxidizes to ferrocenium (Fc^{+}), and the $FcH^{+/0}$ redox pair is commonly used as a reference in non-aqueous electrochemical operations [28-30]. Most research has focused on alkane thiols conjugated to gold and terminated with ferrocene.

A recent study by Wong *et al*.[31] found that self-assembled ferrocene-alkanethiol monolayers exhibit strong ion coupling under oxidized conditions, extending chain lengths beyond 1 nm, confirmed by electrochemical and XPS measurements. The formation of ferrocene derivatives depends on the functional group used[32].

Gélinas *et al*, [33] proposed incorporating a combination of redox ionic liquids, specifically ferrocene and ethyl viologen, into the electrolyte of electrochromic devices. The electrolyte is applied as a thin layer between two FTO glass electrodes to enhance electrochemical and transport properties.

Ferrocene derivatives with a transition metal show excellent properties for degrading organic pigments in wastewater, Their electron donor-acceptor conjugated structure makes them non-toxic, stable, and water-insoluble, ideal for use as heterogeneous Fenton catalysts[34, 35]. Additionally, ferrocene derivatives are stable in solution and are commonly used in modified electrodes for H_2O_2 detection due to their fast and efficient response to various electroactive chemicals[36-38].

This study aims to deposit N-(Ferrocenylmethyl)aniline (NFMA)/semiconductor films onto ITO glass electrodes via electrochemical deposition (ECD) and immersion methods to develop multifunctional transparent electrochemical electrodes for physical, chemical and medical application. The resulting NFMA/FTO Ag/ITO and

NFMA/Cu_2O/ITO films were characterized using various techniques, and electrochemical measurements were also performed. These films were then applied in wastewater treatment and H_2O_2 detection.

This dissertation is organized into three chapters:

Chapter 1: Reviews the literature on organometallic and inorganic thin-film materials, including their classification, properties, fabrication methods, and applications.

Chapter 2: Describes the materials and methods for the electrodeposition of AgNPs on ITO, NFMA on FTO, and NFMA/Cu_2O/FTO. It also covers their characterization, hydrogen peroxide splitting, methylene blue, and Rose Bengal removal.

Chapter 3: Discusses the results and applications of AgNPs/ITO, NFMA/FTO, and NFMA/Cu_2O/FTO.

Conclusion: Summarizes the findings and suggests future research directions.

Chapter 1
Overview and Literature

Chapter 1: Overview and Literature

1.1 THIN FILMS IN NANO-SCALE DEVICES

Thin films technology is the basis for considerable challenging technological developments. Since then, thin film technology has been widely operated in numerous fields, such as communication, energy, medicine and food[39]. Thin films defined as materials with thicknesses ranging from nanometers to a few micrometers (**Figure 1.1**). Like many nanoscale materials, thin films have unique optical, electrical, magnetic, dielectric, and optoelectronic capabilities compared to bulk materials[40].

Thin films are used to developing the surface structure to improve performance of mechanical, physical and chemical properties by modifying the near-surface region[41]. Material mainly consists of a bulk and at least one surface. Its bulk properties may be superior, but the fundamental properties may be inferior because the surface interacts with the surrounding environment. One solution is to add another material with higher surface qualities to its surface, combining superior surface and bulk properties[42].

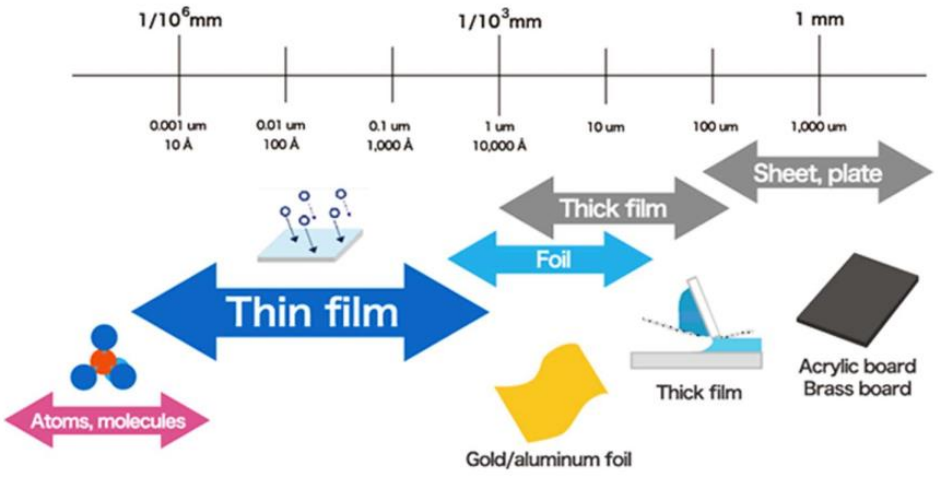

Figure 1.1. Illustrate the size of materials and thin film scale thin film[43] .

1.2 THIN FILMS DEPOSITION TECHNIQUES

Throughout the years, an extensive array of materials has been synthesized in the form of thin films, owing to their profound technological relevance and the substantial scientific focus on exploring and optimizing their properties. This has led to the versatile application of thin films across a wide range of fields, spanning from

nanostructured components and devices to large-scale coatings, such as those utilized on multi-square-meter surfaces like window glass. The deposition techniques used for fabricating these films are typically classified into three major categories, depending on whether the process is primarily chemical, physical, or a combination of both,[44], as depicted in **Figure 1.2**.

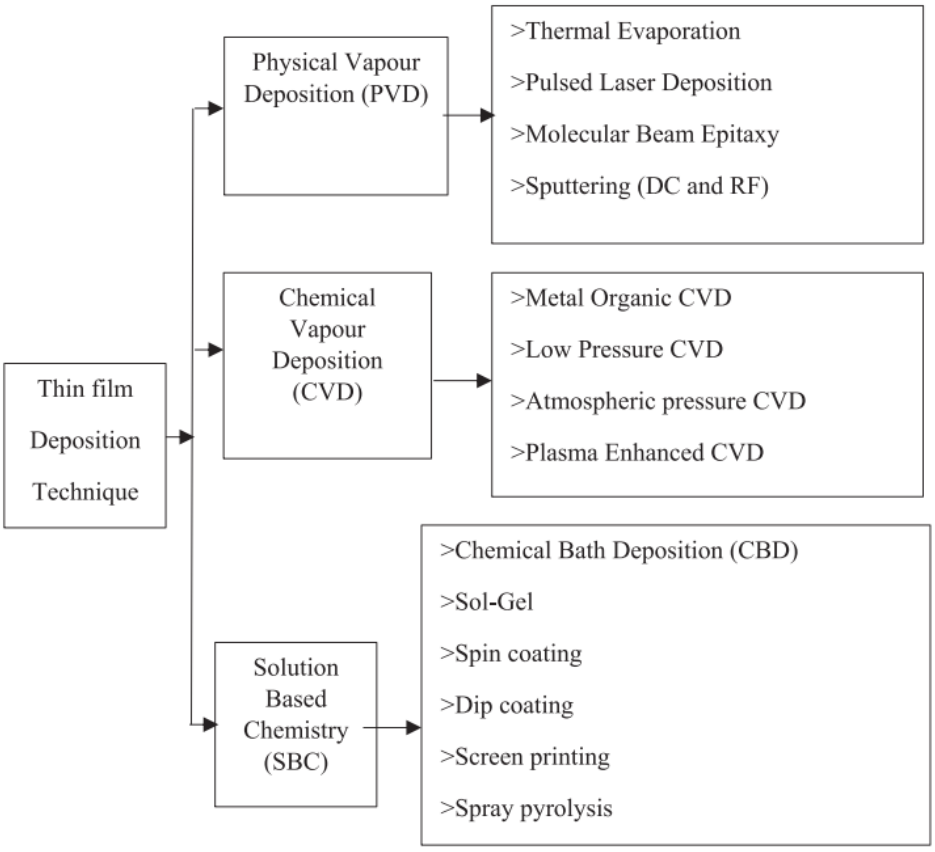

Figure 1.2. Diagram of Various Thin films deposition techniques[45].

1.2.1 Physical vapour deposition (PVD)

The fundamental characteristic of Physical Vapor Deposition (PVD) lies in the vaporization and subsequent condensation of the desired target material. This process can be accomplished through two distinct approaches: thermal and athermal methods (**Table 1.1**). In the thermal process, external thermal energy is employed to evaporate or sublimate the target material. Conversely, the athermal process involves the use of ionized gas molecules to induce evaporation of the target material within a vacuum environment. Based on these processes, PVD techniques can be categorized, as illustrated in the **Figure 1.3.**

Table 1.1 Type of physical vapour deposition techniques [46].

Physical vapour deposition (PVD)	
Thermal process	***Athermal process***
• **Thermal deposition**	• Direct current diode sputtering
• **Electron beam deposition**	• Radio frequency sputtering
• **Molecular beam epitaxy deposition**	• Magnetron sputtering
• **Pulsed laser deposition**	• Unbalanced magnetron sputtering

The procedure encompasses four distinct stages[47]:

- The material to be deposited is evaporated using a high-energy source like an electron beam or ions, causing atoms to be released from the surface;
- The resulting vapor is then conveyed to the target substrate for coating;
- During the transport phase, a reaction occurs between the metal atoms and a suitable reactive gas (e.g., oxygen, nitrogen, or methane);
- Finally, the coating is deposited onto the surface of the substrate.

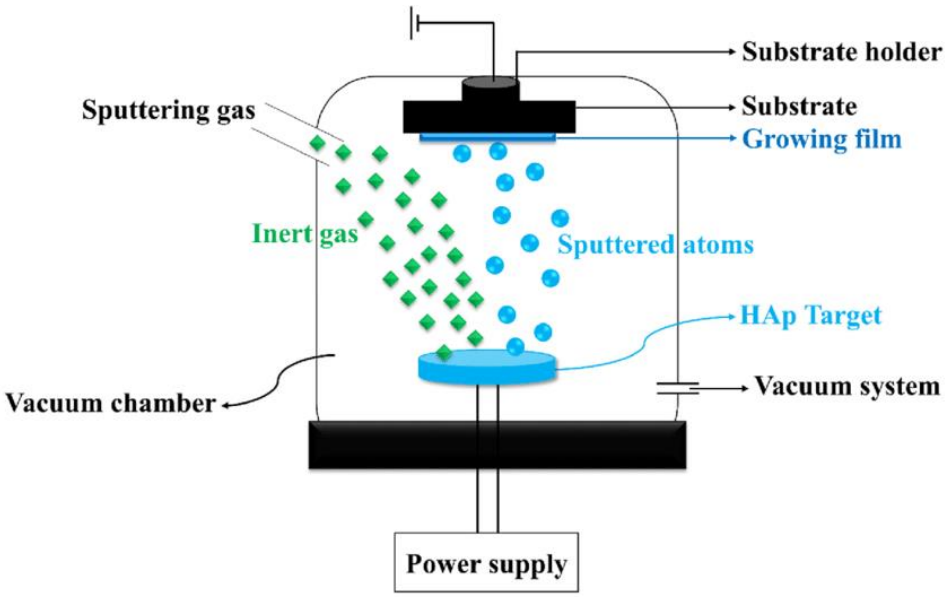

Figure 1.3. The process steps involved in a Physical vapour deposition[48].

1.2.2 Chemical vapour deposition (CVD)

Chemical Vapor Deposition (CVD) is a manufacturing process where a solid material is applied onto a substrate from a gaseous phase, typically mixed with carrier gases. This technique differentiates itself from Physical Vapor Deposition (PVD) by utilizing solid precursors and vaporizing the material to be deposited from a solid target onto the substrate. There are several different procedures for chemical vapor deposition (CVD), including as atmospheric pressure CVD, low pressure CVD, metal-organic CVD, plasma-assisted CVD, laser CVD (LCVD), photochemical vapor deposition, chemical vapor infiltration, and chemical beam epitaxy. The main techniques for chemical vapor deposition (CVD) include thermal CVD, plasma-enhanced CVD (PECVD), and laser CVD (LCVD). Each of these approaches necessitates the use of volatile precursors, which experience chemical composition alterations during the deposition process [49].

The Chemical Vapor Deposition (CVD) method generally encompasses four primary stages that facilitate the creation of thin films[50]:

At the beginning, the reactant gasses (depicted as blue circles) are introduced into the reactor (shown as step a). Afterwards, there are two possible routes for the reactant gases: direct diffusion through the boundary layer (step b) and adsorption onto the substrate (step c). In another scenario, the reactant gases can engage in gas-phase reactions (step d), resulting in the creation of intermediate reactants (green circles) and by-products (red circles). These substances are subsequently deposited onto the substrate through diffusion (step b) and adsorption (step c). Surface diffusion and heterogeneous reactions, specifically step e, take place on the surface of the substrate prior to the formation of thin films or coatings, as shown in **Figure 1.4**. Ultimately, the residual substances and unreacted components are released from the surface and discharged from the reactor as emissions (step f). The entire procedure is referred to as chemical vapor deposition (CVD).

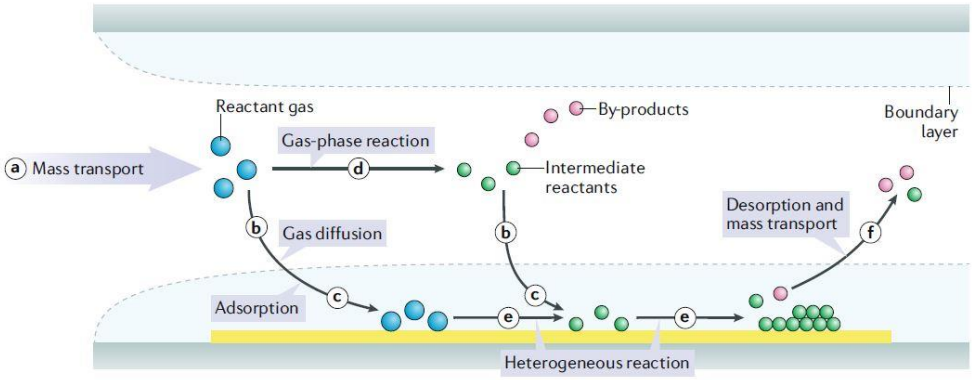

Figure 1.4. Illustration representing fundamental elementary stages of a standard CVD process[50].

1.3 Thin Film Growth

Thin-film growth is an extensively researched discipline, with several growth processes accessible, starting from ultra-high vacuum systems (UHV) to chemical deposition techniques. A film or coating, in general, is a surface region with a different composition and properties than the underlayer. Typically, the film is generated by depositing one material on top of another, and the body coated by the film is referred to as the substrate. In addition, thin-film growth usually happens under thermodynamically stable conditions, which atomic species dynamics may even constrain. It allows the growth of novel atomic configurations with unique features that do not exist in bulk. Furthermore, the reduced dimensionality enables the use of quantum mechanical effects that would otherwise be impossible to achieve.

Therefore, the term "thin-film" should only be used for films that have such a small thickness that it affects the physical properties of the layer in some manner. The range of objectives pursued by thin film applications is quite wide. They play a crucial role in a diverse range of technological disciplines. They are widely utilized in spintronics devices, optical applications, coatings, semiconductors, and corrosion prevention. Many of these applications require intricate development procedures.

Thin films are also essential in physical science since they enable the investigation of the distinctions between (quasi-)two-dimensional states of matter and three-dimensional. Changes in layer thickness may influence chemical reactivity or metal conductivity[51].

1.4 Nucleation and film growth

Nucleation on the surface of a sample occurs when vapor or liquid phase atoms are deposited at coverages (θ), leading to sufficiently high 2D dispersion pressures. This causes local density variations in the 2D gas, resulting in the formation of stable clusters or nuclei. In this context, "stable" refers to clusters that are more likely to grow and coalesce rather than separate or disperse on the substrate. These stable nuclei serve as the foundational structures for further growth and play a crucial role in determining the material's eventual surface properties and overall morphology [52, 53]. There are three forms of film growth, as appear in **Figure 1.5.**

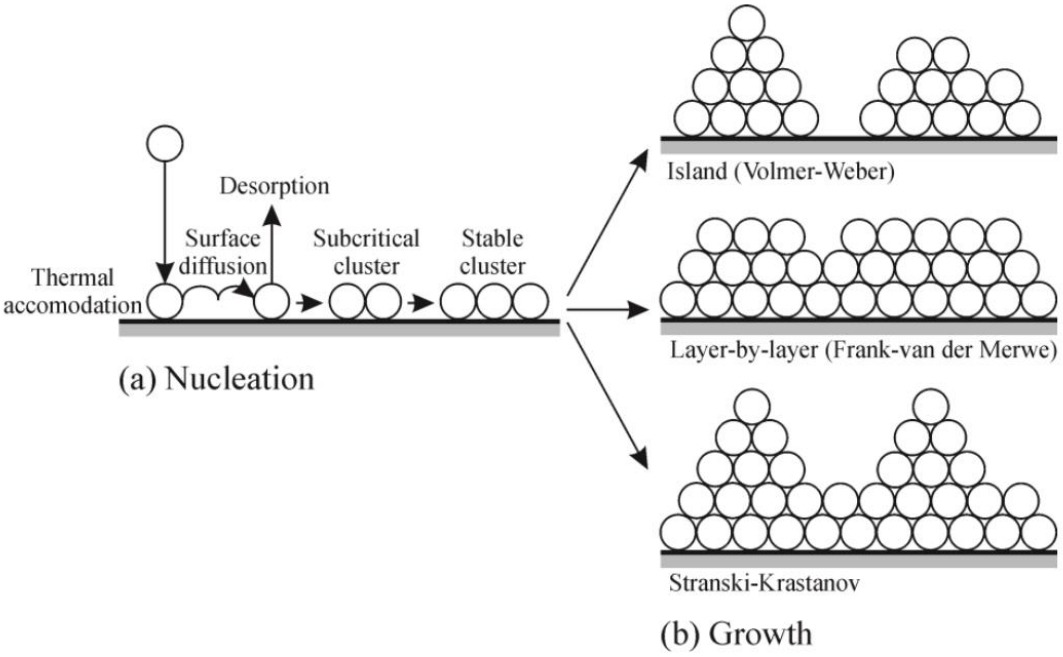

Figure 1.5. Schematic representation of (a). Nucleation of thin films and (b).Modes of thin films growth[54].

The balance between the surface energies of the substrate (γ_s), film (γ_f), and film-substrate interface(γ_i) governs microstructural change during growth at the conditions near-thermodynamic equilibrium[52]. **Figure 1.5** Illustrate the Specific epitaxial growth is that $\gamma_s \geq \gamma_f + \gamma_i$, which indicates that the film thoroughly wets the sample in order to underestimate the surface energies and consequently grows in a layer-by-layer technique[55]. In the case of islands where if $\gamma_s < \gamma_f + \gamma_i$ the surface energy is somewhat underestimated by clustering up and growing islands or mounds of the deposit. In the third method of growth, the film initiates to grow in

A layer-by-layer technique initially forms thin films, but after reaching a critical thickness, strain relaxation allows three-dimensional islands to grow on top of the initial layers. Strain relaxation can occur coherently or incoherently, leading to the formation of misfit dislocations beneath the islands to relieve strain energy. This growth mode is known as Stranski-Krastanov. It involves the transition from a two-dimensional layer-by-layer growth to three-dimensional island formation, driven by the balance between strain energy and surface energy, commonly observed in epitaxial film deposition systems[56].

1.5 Transparent Conducting Oxides (TCOS)

Transparent conducting oxide (TCO) thin films find extensive application in display devices, energy harvesting photovoltaic devices, and various emerging flexible optoelectronic devices. These TCOs exhibit a distinctive coexistence of seemingly contradictory optical and electrical characteristics, which confer significant advantages for a broad spectrum of optoelectronic device applications[57]. It is believed that the presence of diverse defects in TCO systems is responsible for the desirable and adjustable structural, surface, optical, and electrical properties[58]. These defects play a crucial role in modulating the interconnected optical and electrical features of metal oxide systems[59].

In order for a material to demonstrate this characteristic, it must not absorb light in the wavelength range of 380 nm (3.26 eV) to 780 nm (1.59 eV), meaning it must possess an optical bandgap greater than 3.2 eV. Materials with both high electrical conductivity and optical transparency are the foundation of various essential technologies, such as flat panel displays, solar energy harvesting, and other opto-electronic devices[60]. Several Transparent Conductive Oxide (TCO) materials, including In_2O_3, SnO_2, CdO, $CdIn_2O_4$, and ZnO, are known for their n-type conductivity, although p-type TCO materials exist, their properties are inferior to those of n-type TCOs[61-63].

The n-type conductivity in ITO and FTO arises from the presence of shallow donor states near the conduction band due to chemical doping. The excess or donor electrons thermally ionize into the host conduction band at room temperature. With further doping, a degenerate gas of current-carrying electrons is created, resulting in high electrical conductivity and far infra-red absorption (Drude-like behavior), while

still maintaining optical transparency in the visible region as the conduction band remains intact[64, 65].

1.5.1 Band Gap Structure of Solids

Band theory is based on the behavior of valence electrons, while the influence of core electrons, which are contained, can mostly be ignored. The symmetry of the interaction between adjacent orbitals is characterized by the wave vector k, satisfying the Blöch relationship, which allows electronic wave functions within the solid to adopt periodic arrangements of atomic orbitals throughout the entire structure. Consequently, these wavefunctions become stationary solutions to the Schrödinger equation, subject to periodic boundary conditions for an electron, resulting in undisturbed electron movement (no scattering) in the crystal when the Bloch relationship is met. The scattering phenomena arise from defects, phonons, electron-electron interactions within the crystal, and boundaries.

While free atoms possess discrete energy levels in the form of atomic orbitals, the energy states available to electrons in solids form bands. In conductive metals, the Fermi level intersects a partially filled band, permitting some electrons to occupy unoccupied states (**Figure 1.6a**).

Electricity conduction takes place in the material when the momentum of the electron's changes, and a net drift velocity can only occur if there are vacant states inside the band. Consequently, materials with completely filled bands do not exhibit electrical conductivity under weak external forces. However, at elevated temperatures, same materials can become conductive as electrons are able to transition into conducting states located above the energy gap. Conversely, solid insulators have electrons confined to the valence band, which is separated by a substantial energy gap from the conduction band, also referred to as the band gap (**Figure 1.6b**)[60].

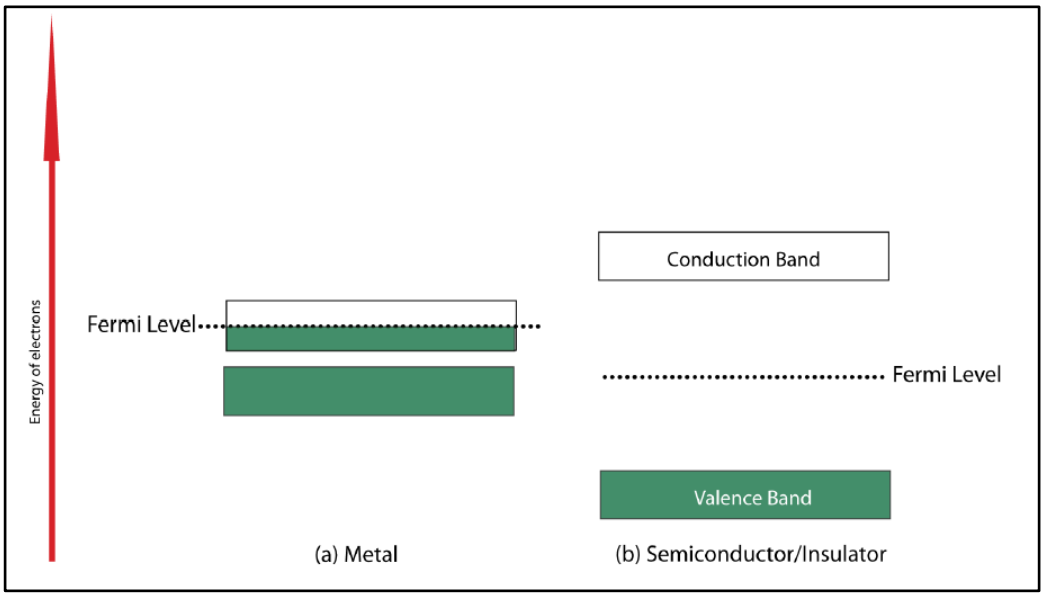

Figure 1.6. Energy bands for solids (a) Metal (b)Semiconductor/Insulator[60]

1.5.2 Chemical solution deposition (CSD)

Chemical Solution Deposition (CSD) is a versatile coating technique characterized by the interaction between the substrate surface and the components dissolved in a solution. The method takes its name from chemical vapor deposition, highlighting the fundamental principle of material deposition through chemical reactions.

CSD is classified as a soft solution-processing technique, offering several advantages, including simplicity of setup and operational convenience. It can be performed under atmospheric pressure and at relatively low temperatures, typically below 373 K. This allows for the deposition of a wide range of materials without the need for specialized equipment or conditions, making it accessible for various applications in materials science and engineering [66].

Although the CSD reaction can be expedited by hydrothermal and electrochemical reactions, the simple CSD process has the advantage of not necessitating excessive heating or electrochemical power, rendering it more advantageous for industrial applications[67]. Simple CSD can be employed with low heat-resistant materials, substrates of complex shapes, and porous materials. As a result, CSD is gaining attention as a cost-effective and environmentally friendly coating process[67]. However, the utilization of CSD in industries is limited because it is often challenging to achieve a uniform coating[68].

In many cases, instead of a continuous coating, dots or islands tend to form on the substrate due to the preferential growth of existing nuclei over the formation of new nuclei. To achieve a homogeneous coating, precise control of the deposition conditions is essential[69].

Figure 1.7 provides a comprehensive description of the standard chemical solution deposition (CSD) technique and its regularly employed modifications. The procedure commences with the preparation of appropriate precursors, typically salts such as carboxylates or other metallo-organic compounds such alkoxides (Section 2). The precursors are dissolved in suitable solvents and combined in a stoichiometric ratio to attain the required composition of the ultimate film. Modifications to the composition may be required in situations where there are losses of components due to volatility (such as PbO), diffusion into the substrate (such as Bi loss from SBT), or purposeful divergence from stoichiometry to create secondary phases or native point defects. Chemical stabilizers and additional processing processes, such as refluxing, can be used to alter the characteristics of the coating solution (Section 3).

The next step involves depositing the coating solution onto the substrate using techniques like spin coating with a rotating substrate, spray coating with a misted solution, or dip coating in a solution bath (Section 4). Subsequently, the wet film is dried (Section 5), followed by pyrolysis (Section 6) and crystallization. Optional post-annealing can be performed to further enhance densification or manipulate the microstructure (Section 7).

Pyrolysis refers to the conversion of solid organic materials into gases and liquids through indirect heat, excluding air or oxygen. The temperature range for pyrolysis typically falls between 400-800 °C. The term "thermolysis" is sometimes used interchangeably with pyrolysis. While both processes involve the volatilization and decomposition of solid organic materials through heat, "pyro" derives from the Greek word for fire, while "thermo" accurately denotes heat. Therefore, the term "thermolysis" is predominantly used in the context of CSD technology to describe the decomposition of the organic matrix in the presence of air or oxygen. In **Figure 1.7**, some processing steps such as gel formation and organic removal are not explicitly separated.

The wet film undergoes a controlled heating procedure to convert it into the desired crystalline film. This process can be done using a hot plate and traditional

furnace or a rapid thermal annealing (RTA) oven. The thermal processing settings differ according on the selected CSD route and film deposition technique. If the desired film thickness is not attained during the initial coating cycle, the deposition and heating process sequence is repeated in order to generate films that are thicker. After achieving the appropriate thickness, a further thermal treatment at a higher temperature can be used to trigger crystallization, enhance the microstructure, or raise the density of the film[66].

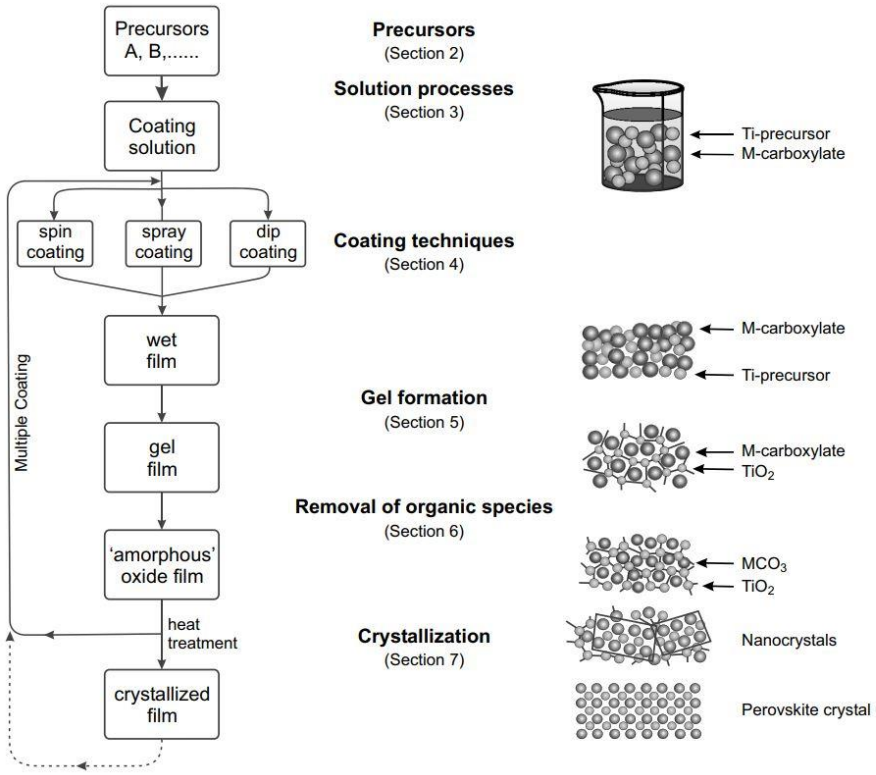

Figure 1.7. A flowchart illustrating common solution processing routes for thin film fabrication. The simplest route is represented by a solid line (—), while alternative pathways are indicated by dashed lines (....)[66].

1.5.3 Electrochemical deposition (ECD)

The electrochemical deposition technique is an extremely valuable strategy for producing nanostructured electrocatalysts for oxygen reduction reaction (ORR). By manipulating the electrochemical deposition conditions, the surface characteristics, configurations, and dimensions of the electrocatalysts can be precisely regulated on conducting materials. Additionally, a notable advantage of the electrochemical deposition method is the absence of any capping reagent, surfactant, or dispersing agent, which significantly simplifies the synthesis procedures[70].

The reduction reaction produces a solid thin film on the surface of an electrically conducting electrode. In **Figure 1.8**, the electrochemical cell consists of three electrodes: the counter electrode, the working electrode, and the reference electrode. The counter electrode, which is connected to the electrochemical analyzer and the working electrode, regulates the electric current in the ECD system. Typically, the counter electrode has a larger surface area than the working electrode to ensure stable current flow and diffusion to the working electrode.

The working electrode transfers electrons to the electrolyte solution, enabling the thin layer to be deposited by the reduction reaction. The electrode is linked to both the electrochemical analyzer and the reference cell, which regulate and modify the desired potential and cycle time during the reduction reaction. The electrolyte facilitates electron transport and oxidation reactions at this location, allowing for precise control over the thickness and structure of the film being deposited.

The reference electrode is used to ascertain and quantify the potential of the working electrode cell. It establishes communication with the electrochemical analyzer in order to modify the potential of the working electrode accordingly[71, 72].

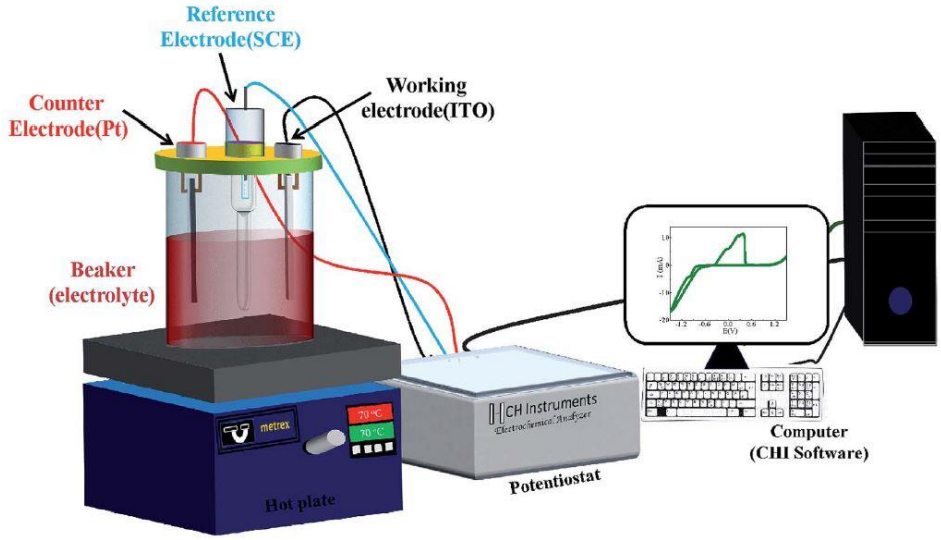

Figure 1.8. Schematic of the electrochemical deposition[73].

1.6 INORGANIC THIN FILMS

Historically, metal oxide nanoparticles have found extensive use across various applications, encompassing energy storage devices, catalysis, sensors, environmental remediation, and numerous others. Nonetheless, these nanoparticles exhibit

remarkable surface properties and microstructural attributes that render them significant for pollutant adsorption purposes. Due to the presence of active sites and a substantial surface area, they demonstrate enhanced efficacy in adsorption processes[74].

Experimental findings have demonstrated that metal oxide thin films exhibit exceptional properties in terms of optics, morphology, composition, electrical characteristics, and acoustical behaviors, making them highly suitable for deployment in these aforementioned areas. The deposition of these films on various substrates has been accomplished using a range of methods such as DC magnetron sputtering[75] , chemical bath deposition[76] , electro-deposition [77] , sol-gel spin coating[78] , pulsed laser deposition[79] , spray pyrolysis [80] , thermal evaporation deposition[81] , molecular beam epitaxy[82] , and chemical vapor deposition[83] .

1.6.1 Silver thin film.

The microelectronics industry is highly interested in depositing thin and uniform conductive films that conform well to complex three-dimensional structures with a high aspect ratio, which is a result of semiconductor device miniaturization[84, 85]. Consequently, a significant challenge lies in achieving a uniform filling of metallic films into these structures. Silver is particularly attractive for microelectronic applications due to its low electrical resistivity[86-88]. Additionally, its exceptional optical properties make it suitable for various applications such as optical coatings, mirrors, and sensors, while its chemical reactivity is utilized in antibacterial surfaces. An increasing number of these applications require the growth of ultra-thin silver layers that conform precisely, posing a challenge for most deposition methods[89]. Currently, line-of-sight methods, particularly physical vapor deposition (PVD) are utilized to produce silver films with superior electrical conductivity and minimal critical thickness [90-92].

Among these methods, sputtering with Al and Cu doping enables the production of ultra-thin silver films with excellent morphological and electrical properties without the need for a seed layer[93-95]. However, line-of-sight techniques face limitations when it comes to complex three-dimensional shapes like trenches and encounter challenges in achieving uniformity on non-flat substrates. Non-line-of-sight approaches such as chemical vapor deposition (CVD) and atomic layer deposition

(ALD) often result in non-conductive coatings for thicknesses below 20-50 nm[85, 96-100].

AgNPs possess unique characteristics, including significant surface energies, quantum confinement effects, high electron accumulation, and strong responses to visible light[101]. These properties make them highly desirable for various applications, such as electrochemical nitrate sensors, high-performance energy devices, transparent conductors, and solar cells. Recent research has focused on the importance of silver NPs from both theoretical and practical perspectives[102]. The development of flexible devices has gained attention due to their lightweight, low cost, and ease of storage and transportation[103]. However, creating transparent conducting materials with conflicting qualities like optical transparency and electrical conductivity is a challenging task. Prominent materials in this field of research include indium tin oxide (ITO), fluorine-doped tin oxide (FTO), aluminum zinc oxide (AZO), silver nanowires, carbon nanotubes, graphene, graphene oxide, and metal networks[104].

1.6.2 Copper oxide thin film

Cu_xO semiconductors have garnered significant attention in academic research and practical applications of nano or optoelectronic devices. This is primarily due to their remarkable characteristics such as chemical stability, non-toxicity, abundance, potential for particle size manipulation, outstanding catalytic properties, and ability to meet the cost-effective manufacturing requirements under normal conditions. Consequently, these semiconductors hold great promise for utilization in energy storage, conversion, and the development of advanced rechargeable lithium-ion batteries in the future [105-110].

In recent years, significant efforts have been directed towards the advancement of affordable energy conversion devices. Among the noteworthy outcomes of photovoltaic research is the application of copper oxide semiconductors in solar cells. Copper oxides, specifically Cu_2O and CuO, possess advantageous attributes such as low cost and widespread availability (**Figure 1.9)**. The potential utilization of Cu_2O in semiconducting devices has been acknowledged as early as 1920, with renewed interest emerging in the mid-1970s within the photovoltaic community[111].

The distinctive properties of copper oxides render them suitable for incorporation into thin film solar cells. For instance, Cu_2O exhibits non-toxic characteristics, theoretical solar efficiency ranging from 9% to 11%, and a straightforward and cost-effective process for semiconductor layer formation. Consequently, it stands as one of the most inexpensive and accessible semiconductor materials for solar cells. Additionally, cuprous oxide possesses a band gap of 2.0 eV, falling within the acceptable range for solar energy conversion, as semiconductor materials with band gaps between 1 eV and 2 eV are considered favorable for photovoltaic cells[112].

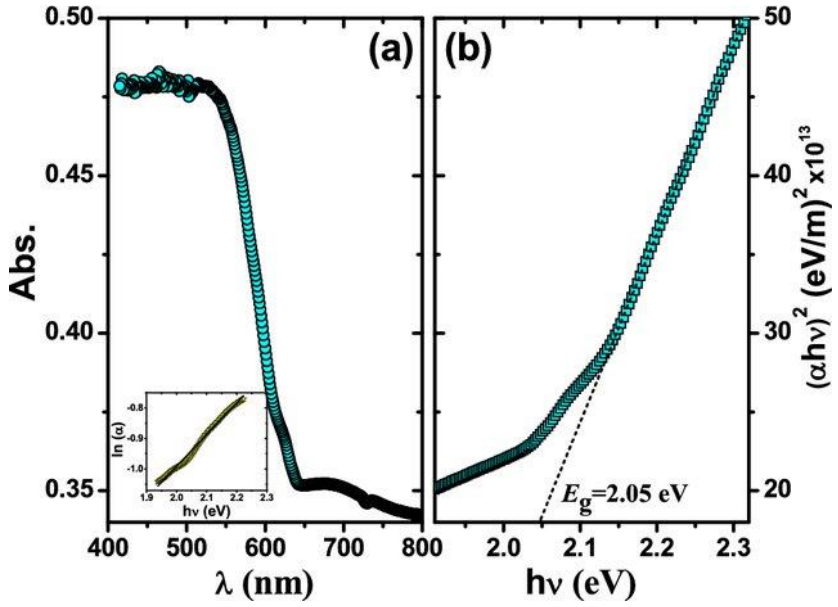

Figure 1.9. (a) The UV-Vis absorbance spectra of a Cu_2O thin film electrodeposited on an FTO substrate. (b) A plot was generated to display $(\alpha h\nu)^2$ as a function of photon energy ($h\nu$) for the corresponding Cu_2O thin film. By examining the linear portion of the graph, the x-intercept at $(\alpha h\nu)^2 = 0$ was identified, and the optical band gap (Eg) was obtained[113].

Various techniques exist for fabricating Cu_2O films on conducting substrates such as copper, including thermal, anodic, chemical oxidation, and reactive sputtering methods. Of particular interest is the electrodeposition method, which is attractive due to its cost-effectiveness and simplicity for deposition on either metal substrates or transparent conducting glass slides coated with highly conductive semiconductors like ITO, SnO_2, and In_2O_3. This approach opens up possibilities for the production of back wall or front wall cells. It is worth noting that the electrochemical preparation of Cu_2O thin films has garnered significant attention in recent years[114].

1.7 Organometallic Thin Films

Organometallic compounds, characterized by at least one bond between a metal and a carbon atom, represent a vital intersection of inorganic and organic chemistry. This interdisciplinary field has significantly advanced the understanding of chemical bonding mechanisms, particularly due to the distinctive bonding properties and intricate molecular structures of these compounds. Beyond their theoretical significance, organometallic compounds are invaluable in practical applications, especially in catalysis and organic synthesis[115].

organometallic compounds bring numerous advantages, such as enhanced reactivity, improved reagent efficiency, increased product yields, and reduced energy requirements and environmental impact. Their adaptability is particularly prominent in advanced technological domains, including nanotechnology and microelectronics. Here, they serve as essential precursors in synthesizing thin films for integrated circuits and other high-performance materials. This role highlights their pivotal contribution to advancing material science and electronic device innovation[116].

1.8 Metallocene

Metal-organic frameworks (MOFs) are exceptionally promising materials that hold great potential in diverse sectors such as electrocatalysis, electronics, and batteries[117, 118]. These structures are composed of arrays of inorganic nodes coupled by organic ligands in many dimensions. They provide a solution to the increasing demand for cleaner and sustainable energy storage[119, 120]. The fabrication of thin films of MOFs on conductive substrates has recently enabled their electrochemical characterization and expanded their applications in diverse areas (**Figure 1.10)**[119].

While initially most MOFs were regarded as electrical insulators, there have been reports of certain MOFs demonstrating efficient charge transport [121-123]. By carefully selecting ligands and nodes with appropriate electronic properties during MOF synthesis[122], it becomes possible to create extended structures with pathways for charge transport[123]. Additionally, postsynthetic modifications (PSMs) of existing MOFs have proven to be an effective strategy for incorporating electroactive components. In particular, the use of coordinatively unsaturated metal clusters has

been extensively employed to introduce redox-active species within the frameworks[124-126].

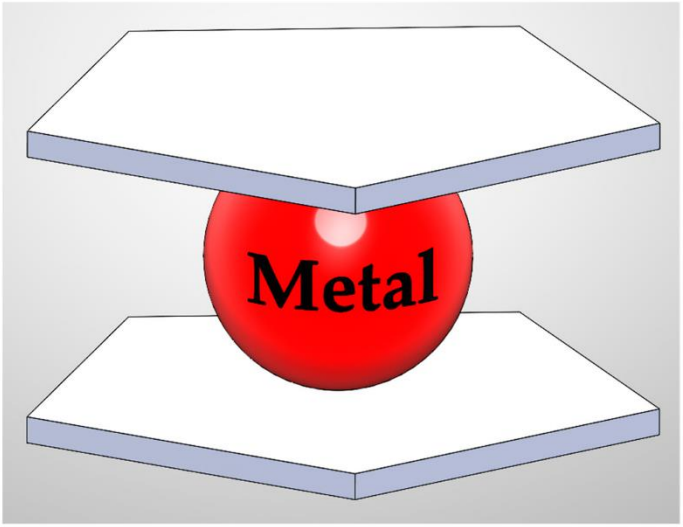

Figure 1.10. Metallocene Chemical structure[127] .

1.8.1 Ferrocene as electroactive material

Organometallic compounds have garnered significant attention in the realm of electro-active materials due to their distinct chemical and electrochemical attributes [128-133]. Among these compounds, ferrocene stands out as particularly noteworthy, owing to its exceptional properties. These properties include remarkable tolerance to oxygen and moisture as well as notable thermal stability[134-137]. Ferrocene derivatives are organic compounds widely regarded as standard systems due to several key factors. First, their structural stability, stemming from the unique ferrocene framework, provides a solid foundation for their use. Secondly, the straightforward modification process facilitates a reversible single electron transfer (Fc^{+}/Fc), making them versatile in various applications.

Additionally, these derivatives exhibit lower oxidation/reduction potentials, making them attractive for electrochemical procedures, especially in non-aqueous solutions, where the fully reversible $FcH^{+/0}$ redox pair serves as a typical reference, A significant advantage of ferrocene-derivatives lies in their simplicity for organizing self-assembled monolayers (SAMs)[26-30]. Ferrocene (Fc) and its polymers are frequently employed in the creation of biosensors due to their robustness in redox reactions and the ease with which derivatives can be synthesized. Fc is a resilient metal complex that features an iron (II) atom nestled between two cyclopentadienyl ligands.

A prime illustration of a biosensor that utilizes Fc is the amperometric glucose sensor. These sensors are assembled by affixing glucose oxidase (GOx) onto the surface of metal or carbon electrodes. The redox reaction of Fc is then linked with the glucose oxidation catalyzed by GOx, facilitating the electron transfer from the active center of GOx to the electrode[138, 139].

Fc-modified materials are commonly utilized to create thin films on electrode surfaces, which are integral in the construction of mediator-type biosensors. There are various methods typically used in the formation of Fc thin films, including in situ polymerization, layer-by-layer (LbL) deposition, and selective adsorption electrodeposition.

In 2014, Constantinescu *et al*,[140] ferrocene carboxaldehyde, or cyclopentadienyl(formylcyclopentadienyl)iron, were developed on silicon and glass substrates. This was achieved using a technique called matrix-assisted pulsed laser evaporation, with a Nd:YAG device operating at 266 nm (4ω).

The films demonstrated second harmonic generation capabilities when tested with a femtosecond Ti:sapphire laser. Similarly In the same year, Matei *et al*,[141] have explored the creation of high-quality, nanometric ferrocene thin films using a non-traditional method known as matrix-assisted pulsed laser evaporation (MAPLE). This process was conducted on silicon and ITO coated glass substrates using a Nd:YAG pulsed laser device. In 2015, Hod *et al*,[141] discuss the incorporation of ferrocene molecules into the wide-channel metal-organic framework (MOF) compound, NU-1000.

By applying this alteration as thin-film coatings on electrodes, the MOF becomes electroactive in close proximity to the ferrocenium/ferrocene (Fc+/Fc) redox potential. This phenomenon occurs as a result of the transfer of electrons (redox) between fixed $Fc^{+/0}$ entities. The observed transfer of electrons across different sites indicates the potential usefulness of the installed species as a mediator of electron transfer in photoelectrochemical or electrocatalytic systems.

In 2016, Rong *et al*,[142] conducted a study on anion absorption and charge transport in a polymer called PIM-EA-TB using electrochemical deposition. The researchers analyzed three situations: (i) the process of oxidizing ferrocene within a thin layer of PIM-EA-TB on a glassy carbon electrode, (ii) the process of reducing

protons absorbed within a thin layer of PIM-EA-TB on a platinum electrode, and (iii) the process of transporting anions and protons in a separate PIM-EA-TB membrane that is asymmetrically deposited, which acts as a current rectifier or "ionic diode" under the influence of an applied potential. The diameter and hydrophobicity (size and hydration energy) of the anion exhibited significant conflicting impacts in all instances.

In 2017, Cuartero *et al*,[143] did a study where they used cyclic voltammetry (CV) to analyze thin membranes doped with ferrocene molecules. These membranes were around 200 nm thick and were placed on glassy carbon (GC) substrate electrodes. This is illustrated in **Figure 1.11**. The membranes consisted of either plasticized poly(vinyl chloride) (PVC) or unplasticized poly(methyl methacrylate)/poly(decyl methacrylate) (PMMA-PDMA). It was discovered that the electrochemical oxidation behavior was irreversible, most likely because the degradation of ferrocene occurred at the interface between the GC and the membrane.

Additional investigations on the CV of ferrocene molecules were conducted on GC electrodes in organic solvents. These experiments utilized both chloride-based and chloride-free organic electrolytes. The results revealed that the presence of the chloride anion played a vital role in the irreversible electrochemical oxidation of ferrocene. The researchers examined the electrochemical oxidation process of redox compounds based on ferrocene in thin film electrodes made of both plasticized and unplasticized polymeric membranes.

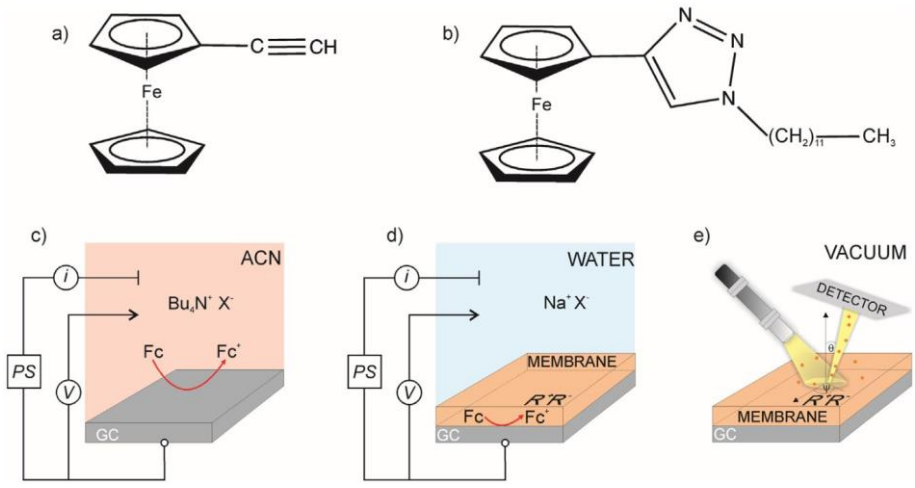

Figure 1.11. Displays the chemical structures of Fc-based compounds. (a) Ethynylferrocene, also known as ethynyl Fc, and (b) 1-dodecyl-1H-1,2,3-triazol-4-yl) ferrocene, also referred to as Lip Fc. (c) Cyclic voltammetry (CV) is performed using a three-electrode system on a glassy carbon (GC) rod or coupon shape. The solvent used is acetonitrile (ACN), and the solution contains either ethynyl Fc

or Lip Fc along with various lipophilic electrolytes that have different anions ($Bu_4N^+ X^-$). (d) Another CV experiment is conducted using a GC rod or coupon coated with a thin membrane layer. The membrane contains either ethynyl Fc or Lip Fc and a lipophilic electrolyte ($R^+ R^-$, ETH500). This coated electrode is then placed in contact with an aqueous solution containing a background electrolyte ($Na^+ X^-$). (e) The thin layer membrane-coated GC coupon is characterized using synchrotron radiation-X-ray photoelectron spectroscopy (SR-XPS) and near edge X-ray absorption fine structure (NEXAFS) techniques. These measurements are performed under ultra-high vacuum conditions, and depth profiles are obtained by alternating argon ion sputtering with SR-XPS/NEXAFS measurements[143].

In 2019, Liu *et al*,[144] developed a unique ferrocene-functionalized silver cluster (FcAgCs) using ultrasound treatment. The ultrasound synthesis method played a crucial role in facilitating and speeding up the synthesis of this remarkable structure. Single-crystal X-ray analysis revealed that the cluster is a cationic species consisting of four rhombic silver atoms and two isolated BF4- counter anions. The cluster demonstrated thermal stability greater than 200°C and was found to be sufficiently stable for the fabrication of FcAgCs/ITO thin films and exploration as electrochemical response materials. These properties led to its use in the preparation of thin films on ITO substrates using the spin coating method (**Figure 1.12**). Furthermore, the FcAgCs/ITO thin film electrode was used as a thin film electrochemical detector, showing a sensitive and rapid response in the detection of H_2O_2.

Deposition of ferrocene derivatives on FTO or ITO glasses showed high efficiency in various fields, improved the quality of the film, and prevented the migration of ions in the film. Ferrocene derivatives can also be coated on various surfaces and used to manufacture delicate devices such as low-cost multi-level organic memorizes [145-147].

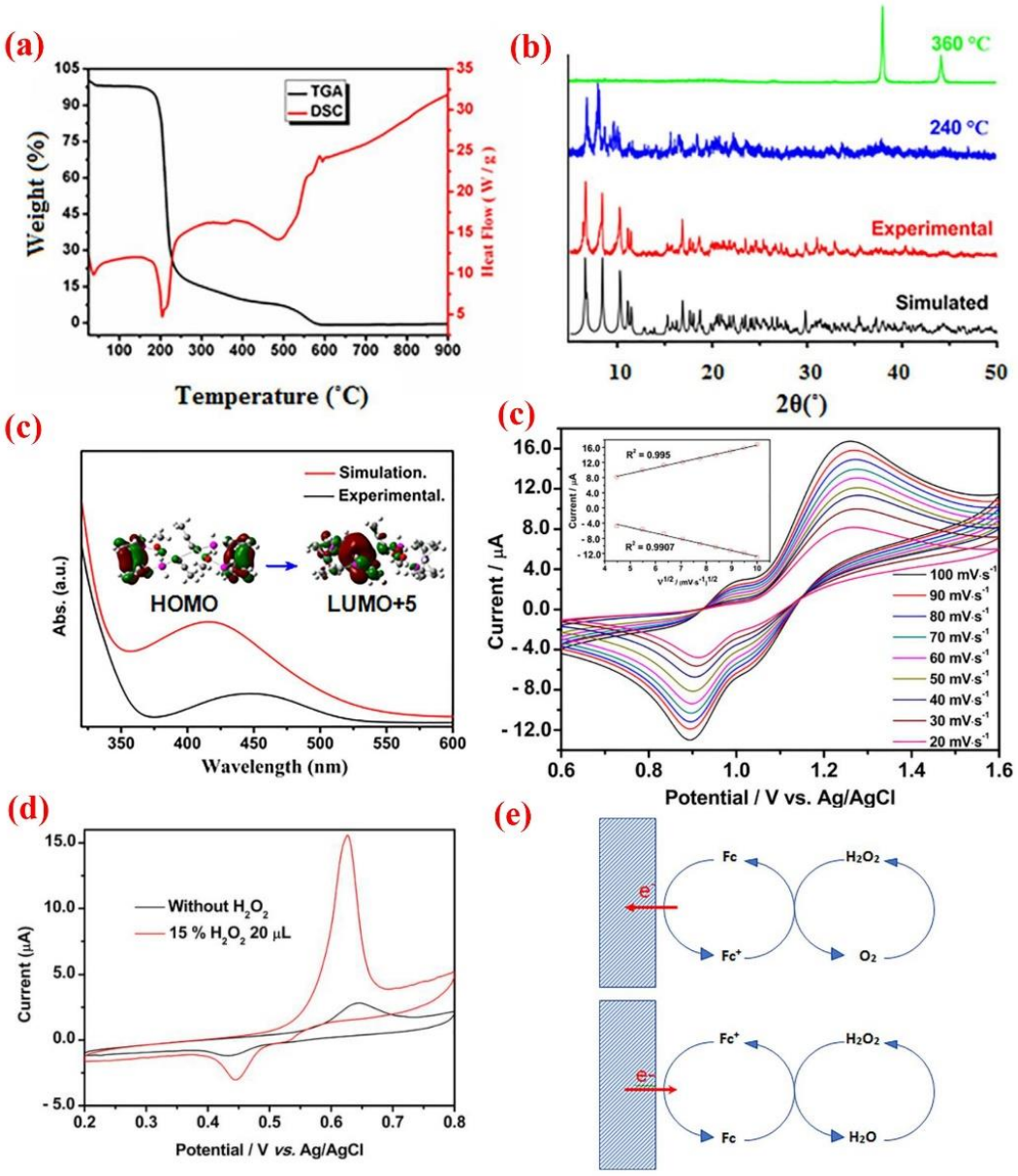

Figure 1.12. Displays the characterization and application of FcAgCs/ITO thin films. (a) The graph displays the TGA and DTA curves. (b) It presents the X-ray diffraction (XRD) pattern of cluster 1 after being heated at various temperatures. (c) The measured absorption is compared with the predicted spectra. The UV–vis diffuse reflectance spectra of the material indicates that the optical energy gap is 2.30 eV. (d) Cyclic voltammograms for compound 1 dissolved in dichloromethane solution with a concentration of 0.1 M nBu_4NPF_6 as the supporting electrolyte were obtained at different scanning rates. The voltammograms showed one pair of redox peaks with average potentials of Epa = 1.258 V and Epc = 0.893 V, followed by one quasi-reversible redox peak within the voltage range of 0.6 V to 1.6 V. The cyclic voltammograms (CVs) of the FcAgCs/ITO thin-film electrode were measured in a 0.1 M Na_2SO_4 solution, both without and with the addition of 15% H_2O_2 (20 µL). The scan rate is 100 mV/s. (e) The suggested process of electron transfer between the electrode and hydrogen peroxide in the presence of the Fc/Fc^+ couple. The anodic and cathodic peaks exhibit a shift to 0.63 and 0.44 V respectively, suggesting that the presence of H_2O_2 enhances both the anodic and cathodic processes[144].

Prior study has created mesoporous silica layers on ITO substrates for electrochemical cysteine detection. These layers were both unmodified and

functionalized with ferrocene, and featured vertical nanochannels. The electrodes, using ferrocenedimethanol ($Fc(MeOH)_2$) as a mediator, exhibited electron transfer rates that were three times higher for cysteine compared to glutathione, enabling the specific detection of cysteine. The sensitivity of cysteine concentrations ranging from 3-20 µM was demonstrated to be 1.28 mA M^{-1} using cyclic voltammetry and amperometry in flow injection study. The reproducibility of the measurements was found to be between 3-12%. The minimum detectable quantity of cysteine was 3 µM[148].

In 2022, Chou *et al*[149] demonstrated the successful immobilization of mononuclear Co^{II} chlorin complexes on conductive metal-oxide electrodes using electron-conducting molecular wires. These wires, featuring phenylene–ethynylene-based π-conjugation and linked permethylated α-cyclodextrin, enhanced electrocatalysis for the selective two-electron reduction of molecular oxygen to hydrogen peroxide (**Figure 1.13)**. The study compared electrochemical behaviors of ferrocene (Fc) molecules on ITO substrates with and without rotaxane encapsulation. Results showed that Co^{II} chlorin immobilized using rotaxane-encapsulated molecular wires exhibited significantly higher electrocatalytic activity and selectivity, with a turnover frequency for H_2O_2 production of 331 ± 75, compared to 82 ± 8 without rotaxane encapsulation.

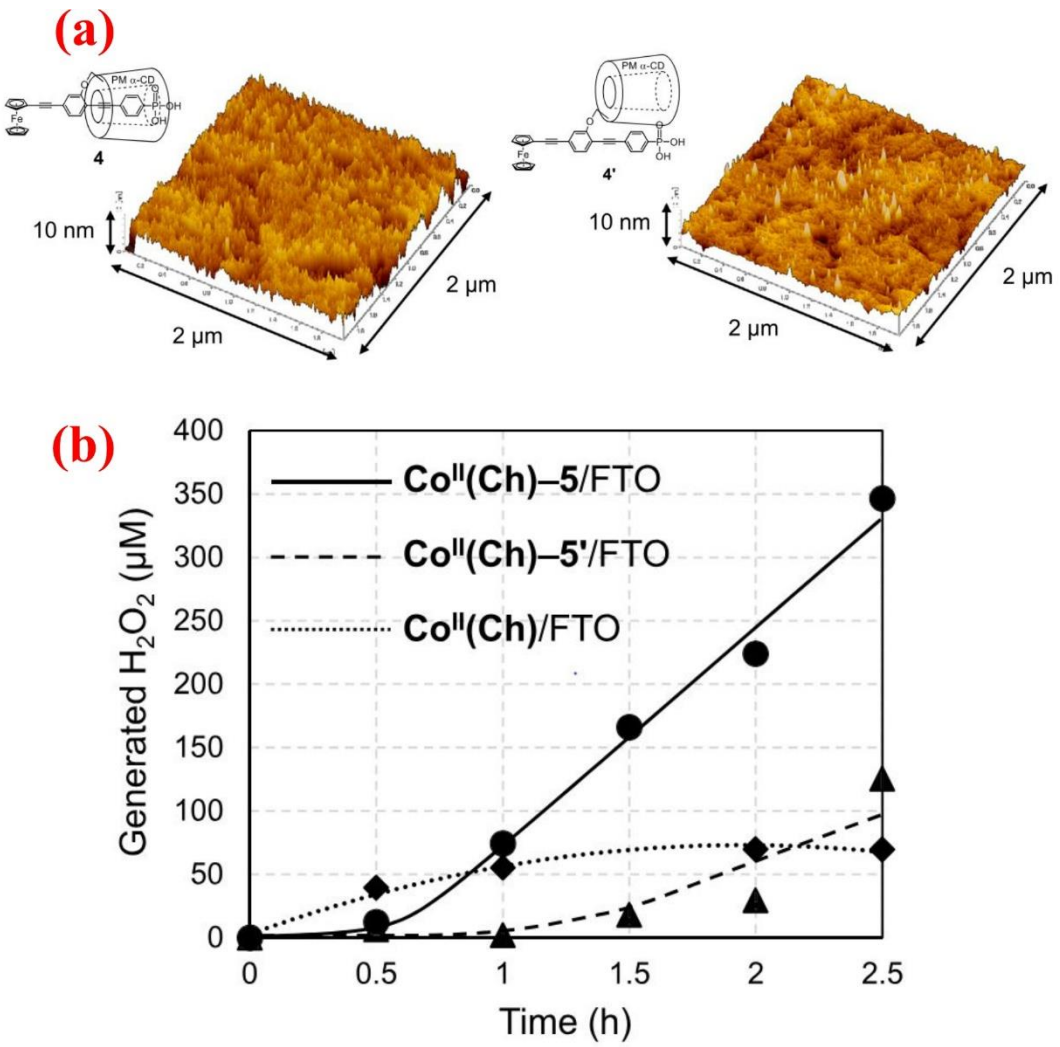

Figure 1.13. AFM images of the ITO substrate modified with (left) 4 and (right) 4' (b). H_2O_2 production of Co^{II}(Ch)–5/FTO (solid line), Co^{II}(Ch)–5'/FTO (dashed line), and Co^{II}(Ch)/FTO (dotted line) fabricated by the LB method[149].

Chapter 2
Experimental Techniques

Chapter 2: Experimental techniques

2.1 ELECTRODEPOSITION

Electrochemical deposition represents a highly adaptable and environmentally friendly approach employed in the fabrication of various nanomaterials. The electrochemical analysis pertains to the chemical reactions of samples or solutions when subjected to an applied electrical potential. The potentiostat, linked to electrodes immersed in an electrolyte, effectively monitors and regulates the rate of redox reactions.

The process occurs within a standard electrochemical cell, The potential is effectively controlled and measured between a reference electrode (R.E.) and the working electrode W.E (cathode), which is the sample. Simultaneously, an auxiliary electrode (C.E.) is positioned at the anode, and the current is quantified between this electrode and the cathode. During the plating process, voltage disparities induce redox reactions within the system, leading to the deposition of metal ions (M^{Z+}) onto the sample. Generally, the redox equation for a metal solution within a basic electrochemical cell is expressed by equation 2.1. At the anode, the metal ions undergo oxidation, transforming into M^{Z+}. These ions subsequently interact with other ion components present in the electrolyte and are drawn towards the negatively charged surface of the sample.

$$M^{Z+} + Ze^{-} \leftrightarrow M \qquad (2.1)$$

Given that the electrolyte comprises metal ions in an aqueous solution (aq), multiple reactions are possible[150], and one of the reactions that merits consideration is the reaction involving water:

$$2H_2O(l) + 2e^{-} \rightarrow H_2(g) + 2OH^{-}(aq) \qquad (2.2)$$

This process can be further broken down into two half-reactions, with each half-reaction occurring at one of the electrodes, namely the anode and the cathode[151]:

$$2H_2O(l) \rightarrow O_2 + 4H^{+}(aq) + 4e^{-} \qquad (2.3)$$

$$2H^{+}(aq) + 2e^{-} \rightarrow H_2(g) \qquad (2.4)$$

At the anode, hydrogen and oxygen act as the oxidants, accepting electrons, while water serves as the reductant, donating electrons. Conversely, at the cathode, hydrogen ions act as the oxidant, and gaseous hydrogen acts as the reductant. Over time, a dynamic equilibrium is achieved as the system reaches a balance between the ongoing reactions[151].

2.1.1 Cyclic voltammetry (CV)

Cyclic voltammetry is a technique that involves applying a potential to a working electrode, following a triangular waveform, and then observing the resulting flow of current. This method offers valuable and direct insights into the energetics of redox reactions, the dynamics and reversibility of electron transfer, and the rates of interconnected chemical reactions. It is widely utilized by both electrochemical experts and those without specialized knowledge in the field.

In the experimental setup depicted in **Figure 2.1**, the working electrode's potential is cyclically varied between two limits. This facilitates the successive oxidation and reduction of an electroactive species. This species can either be present in solution or adsorbed at the electrode's surface. By observing the current as a function of potential, researchers can generate unique current-potential voltammograms specific to the studied system.

Cyclic voltammetry finds diverse applications, spanning from unraveling complex reaction mechanisms to quantifying crucial analytes in environmental, industrial, and medical solutions. Recent technological advancements, including the use of microelectrodes, allow routine measurement of rapid electron transfer rates and even the identification of short-lived species lasting mere nanoseconds[152].

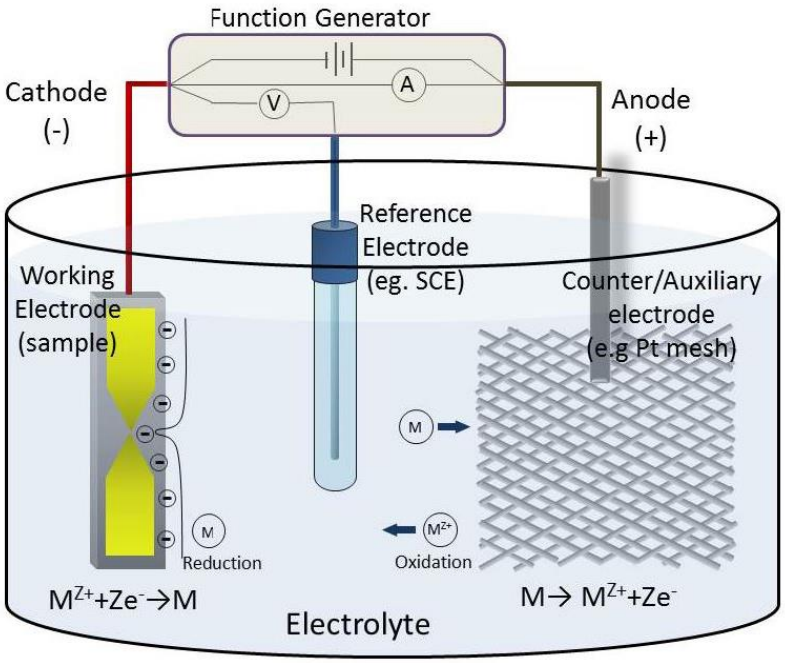

Figure 2.1. The conventional cell utilized for electrodeposition involves positioning the sample at the cathode, and the voltage measurement is referenced against a reference electrode[153].

Cyclic voltammetry (CV) offers a powerful approach for both qualitative and quantitative analysis by enabling the identification of multiple species in a single measurement and estimating their concentrations in solution. The current response observed during the application of potential arises from two primary processes: Faradaic current, which results from redox reactions occurring in the solution, and capacitive current, which is due to the charging of the electrochemical double layer at the electrode-solution interface.

In contrast to potential step techniques, CV plots the current response as a function of applied voltage, rather than time, providing a more comprehensive view of the electrochemical behaviour of the system. This technique is particularly advantageous for studying reversible reactions, where the species involved undergo continuous cycles of oxidation and reduction. The voltage is varied in a controlled manner using a triangular waveform, as illustrated in **Figure 2.2**. This waveform allows for the sequential and cyclic application of increasing and decreasing potentials, which facilitates the observation of both oxidative and reductive processes within the same experiment.

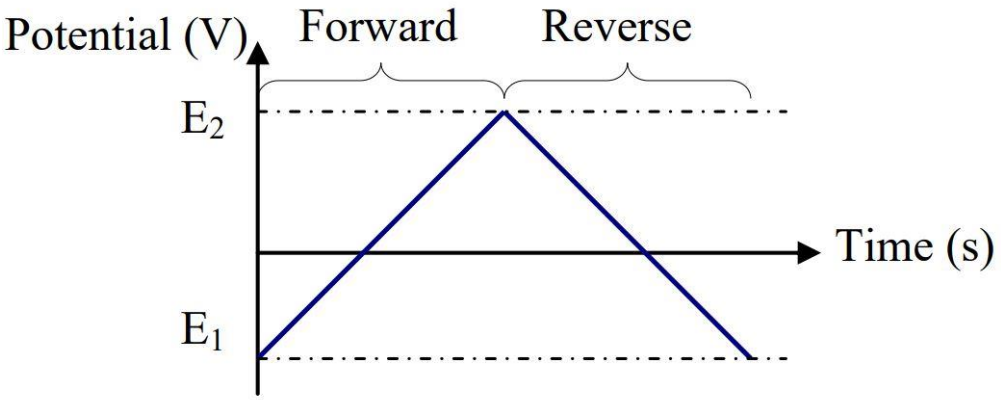

Figure 2.2. The applied potential to the cell as a function of time[154].

The diffusion layer formed at the surface of the macroelectrode displays a linear profile. The cyclic voltammogram obtained for a reversible electrochemical reaction using macroelectrodes (**Figure 2.3**) can be characterized as follows:

1. The peak current ratio at the anode (Ipa) and the cathode (Ipc) is unity (equal to one).

$$|Ip_a|/|Ip_c|=1 \qquad (2.5)$$

2. The peak currents exhibit a proportional relationship with the square root of the scan rate, $\upsilon^{(1/2)}$, as described by the Randles-Sevcik equation:

$$Ip_a = 0.4463zFCA\left(\frac{zFvD}{RT}\right)^{1/2} \qquad (2.6)$$

Which is simplified in:

$$Ip_a = 2.69*10^5 z^{3/2} CAD^{1/2} v^{1/2} \qquad (2.7)$$

Where z represents the quantity of electrons engaged in the reaction, F denotes Faraday's constant (96485 C/mol), C represents the bulk concentration (mol/dm^3), A signifies the electrode surface area in square decimeters (dm^2), υ indicates the scan rate (V/s), D represents the diffusion coefficient in square (dm^2/s), R symbolizes the universal gas constant (8.314 J/mol.K), T stands for the temperature in Kelvin (K), and Ipa refers to the anodic peak current in amperes (A).

3. The relationship between the peak potential and the redox couple potential, Ep can be described as follows:

$$E_p = (Ep_c + Ep_a)/2 \qquad (2.8)$$

4. When the reaction involves z electrons, the voltage difference between the two peak potentials can be approximated using the following estimation[154]:

$$Ep_c - Ep_a = 2.218RT / F \qquad (2.9)$$

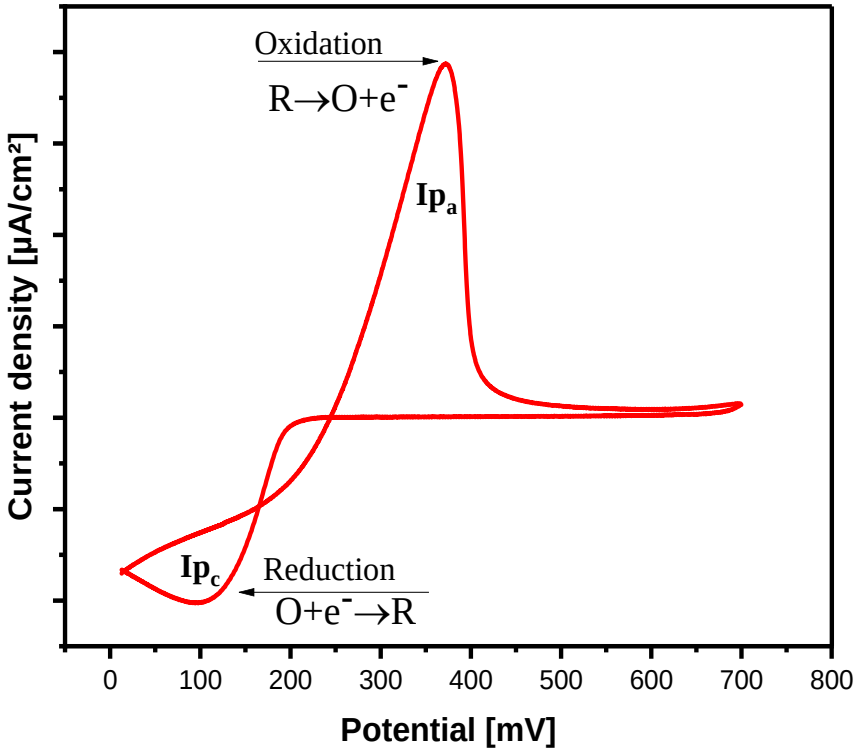

Figure 2.3. Illustrates a cyclic voltammogram of a reversible reaction employing a macroelectrode.

2.1.2 Chronoamperometry

Chronoamperometry is an electroanalytical technique that involves the application of a square-wave voltage to the working electrode over a specific period of time. The electrode current, measured over time, experiences fluctuations caused by the diffusion of an analyte from the surrounding fluid towards the surface of the sensor. Chronoamperometry is a technique used to investigate the relationship between current and time for processes that are controlled by diffusion and occur at an electrode [155].

Chronoamperometric experiments are performed using two primary setups: a single potential step, which entails applying a forward potential step and measuring the resulting current, or a double potential step, where a forward potential is applied and then returned to the initial value within a specified time interval. Cottrell's equation is used to describe the current measured at different time intervals following the

application of a high single potential step or a substantial overpotential in the context of reversible redox processes.

$$it = \frac{nFAC_0 D_0^{1/2}}{\pi^{1/2} t^{1/2}} \qquad (2.10)$$

The variables in the equation are defined as follows: n represents the number of electrons transferred in the redox reaction, F is Faraday's constant (96,485 C/equivalent), A represents the electrode surface area (cm^2), and C and D refer to the concentration (mol/cm^3) and diffusion constant (cm/s), respectively, of the electroactive species in the solution.

Figure 2.4 displays a chronoamperometry with two distinct steps. The potential step program involves a forward potential step (Ei) that reaches a secondary value (Es) within a specific time interval (τ). During the reverse potential step, the potential can either revert back to the starting value (Ei) or be modified to different values of E, depending on the experimental and system conditions. Usually, the electrical current for the opposite scanning potential conditions is also measured within the time interval τ[156].

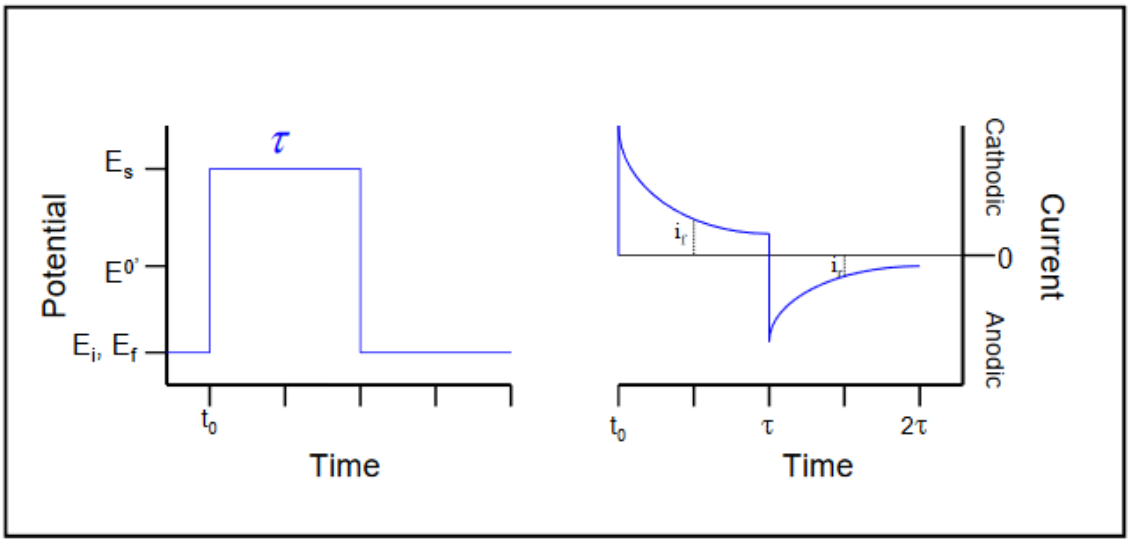

Figure 2.4. Double potential step chronoamperometry[156].

2.1.3 Electrochemical Impedance Spectroscopy (EIS)

Electrical impedance spectroscopy (EIS) represents a potent and versatile method applicable across a wide spectrum of fields, including microbiological analysis, corrosion monitoring, quality assurance of coatings, and the examination of solid electrolytes. The roots of EIS can be traced back to 1894 when it was employed

to determine the dielectric constant of aqueous electrolytes and various organic fluids. Nonetheless, it was not until the mid-1980s that EIS gained substantial traction, primarily due to the advent of computer-controlled digital instruments. These innovative tools facilitated swift and uncomplicated data acquisition and intricate data processing and analysis.

The interest in EIS surged significantly, resulting in a doubling of scientific publications related to EIS applications approximately every four to five years, culminating in over 1200 papers published by 2006. The inaugural EIS conference commenced in 1989 in Bombannes, France, and subsequently, gatherings have occurred every three years.

The EIS procedure essentially involves two variants, one of which is referred to as "potentiostat EIS." In this method, a sinusoidal voltage signal is applied.

$$V(t) = \bar{v} + \hat{v}\sin(wt) \qquad (2.11)$$

A sinusoidal voltage is administered to the sample under examination (SUT), resulting in the generation of an induced electric current.

$$I(t) = \bar{I} + \hat{I} \cdot \sin(wt + \phi) \qquad (2.12)$$

Subsequently, the complex impedance is computed by determining the measured values.

$$z(jw) = \frac{v(j^w)}{I(jw)} = \frac{\hat{v}}{\hat{I}} \cdot e^{-j_\phi} = |z| \cdot e^{J \cdot Ag(z)} \qquad (2.13)$$

$$= Re(Z) + j\,.Im(Z)$$

$\hat{v}$ represents the amplitude of the voltage, while $\hat{I}$ signifies the amplitude of the current. $\bar{v}$ and $\bar{I}$ denote the direct current (DC) values of voltage and current, respectively. The symbol (f) stands for the frequency of the test signal, 'ω' represents the angular frequency (equal to 2πf), and 'φ' denotes the phase difference between V(t) and I(t). Additionally, 'V(jω)' and 'I(jω)' correspond to the Steinmetz transforms of V(t) and I(t), respectively. The parameters associated with the sine-wave can be derived from the collected signals through either a time-domain fitting algorithm, or by employing a fast Fourier transform algorithm[157].

2.2. CHARACTERIZATION TECHNIQUES

2.2.1. X-ray Diffraction (XRD)

X-ray Diffraction (XRD) is a scientific technique wherein X-rays are subjected to diffraction as they interact with the atomic spacing within a crystalline structure. X-rays are chosen as the ideal type of photon for this purpose due to their wavelength being of a comparable magnitude to the spacing between atoms in the crystal lattice. This technique can be applied to analyse a wide range of substances, although it is commonly employed for the specific purpose of mineral sample identification. In XRD, when X-rays are directed at a crystal at certain specific angles, they undergo diffraction.

The critical information lies in the specific angles at which diffraction occurs. It is the combination of these diffraction angles that is utilized to determine the identity of the mineral in question. For instance, in the case of a pure copper sample, distinct diffraction angles typically appear around 43 and 50 degrees. If diffraction occurs at angles other than these, it would indicate a different mineral composition rather than copper. The primary purpose of X-ray Diffraction (XRD) lies in the qualitative determination of the mineral composition within crystalline samples and the determination of their unit cell parameters. In the XRD process, a diffractometer records the diffracted beam emerging from a crystalline specimen that has been exposed to a monochromatic X-ray, typically one generated by the Cu Kα line. The detector is specially engineered to capture the distribution of the diffracted intensity originating from the sample as a function of the scanning angle 2θ.

When we consider the arrangement of atoms and X-ray diffraction planes, as depicted in **Figure 2.5**, the Bragg law dictates that constructive interference occurs under the following conditions:

$$2\,d\,sin(\theta) = n\,\lambda \qquad (2.14)$$

θ represents the incident angle formed between the X-ray radiation and the sample, while 'd' denotes the interplanar distance specific to each crystalline sample. Typically, when X-rays impinge upon a sample, they interact with numerous crystalline structures oriented in various directions. The instrument's geometry is designed to detect only the X-rays that have been reflected at a particular θ angle.

A standard sample contains both crystallites and grain boundaries, with approximately 80% of the signal emanating from the crystallites (with grain sizes on the order of 10^{-6} meters or 10^{4} Ångströms) and the remaining 20% arising from the grain boundaries. Utilizing the Bragg law, one can compute the interplanar distances. For instance, the interplanar distances for the family of planes are as follows:

$$d_{100} = \mathrm{a} \tag{2.15}$$

$$d_{120} = \mathrm{a}\cos(\theta) \equiv a \cdot \frac{a}{\sqrt{a^2 + 4a^2}} = \frac{a}{\sqrt{5}} \tag{2.16}$$

$$sin(\theta)_{100} = \frac{\lambda}{2d_{100}} = \frac{\lambda}{2a} \tag{2.17}$$

$$sin(\theta)_{120} = \frac{\lambda}{2d_{120}} = \frac{\sqrt{5}\cdot\lambda}{2\mathrm{a}} \tag{2.18}$$

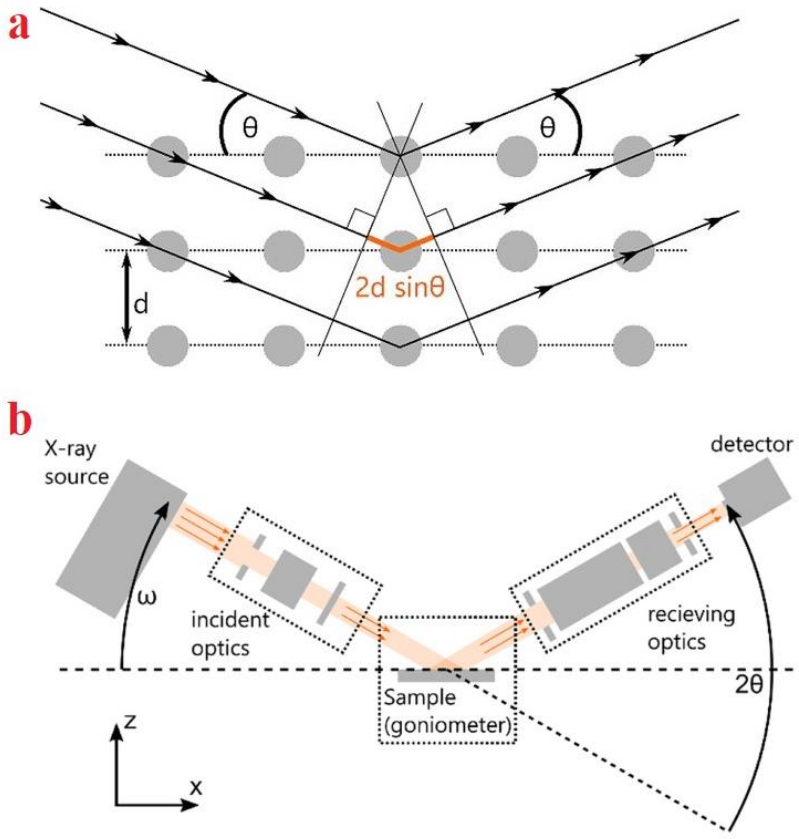

Figure 2.5. XRD analysis (a) Illustration of Bragg's Equation (b) Elements of a Diffractometer[158].

2.2.2. Morphology analysis

Scanning Electron Microscopy (SEM) is a technique for surface analysis, using a high-energy electron beam to generate signals collected into detailed images. Two key interactions occur: elastic scattering, where electrons deflect off atomic nuclei or outer-shell electrons, producing backscattered electrons (BSEs), and inelastic scattering, where energy transfer releases secondary electrons (SEs). BSEs offer compositional and surface data, while SEs provide high-resolution topographic details.

SEM uses an electron source emitting beams between 0.1 and 30 keV, focused by electromagnetic lenses in a vacuum to avoid scattering[159].

The electron beam then scans the surface of the target material using scan coils. As the beam interacts with the sample, it generates various signals, including backscattered electrons, secondary electrons, and characteristic X-rays, which are captured by different detectors. These detectors produce the final images, which are displayed on a computer screen[160].

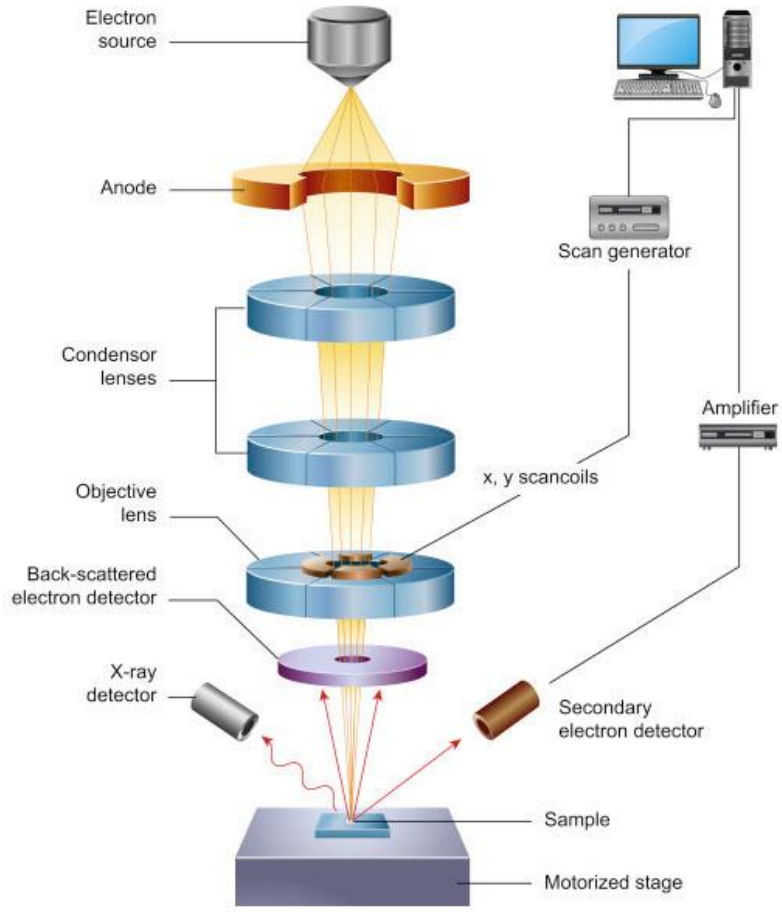

Figure 2.6. A schematic diagram of a scanning electron microscope (SEM)[161].

2.2.3. Optical analysis

UV-Visible spectroscopy (UV-Vis spectroscopy) is an analytical technique used to measure the absorbance or transmittance of UV and visible light by a sample, widely applied in chemistry, biology, and environmental science for identifying and quantifying chemical substances. The principle of UV-Vis spectroscopy is based on the absorption of light by electrons in a molecule, where exposure to UV or visible light promotes electrons from a lower energy state (ground state) to a higher energy state (excited state), corresponding to electronic transitions[162].

The technique involves a light source emitting UV and visible light, which passes through a monochromator to separate the light into its constituent wavelengths. The sample, typically in liquid form, is placed in a cuvette in the light path, and a photodetector measures the intensity of the transmitted light compared to the incident light. The absorbance is calculated using the equation

$$A = \log_{10}(\mathrm{I}_0/\mathrm{I}) \qquad (2.18)$$

where I0 is the incident light intensity and I is the transmitted light intensity, producing a spectrum plotted against wavelength. Applications of UV-Vis spectroscopy include quantitative analysis for determining the concentration of colored compounds in solution using Beer-Lambert's law, qualitative analysis for identifying and characterizing compounds, and monitoring reaction progress in kinetics studies. Its simplicity, speed, and versatility make UV-Visible spectroscopy an essential tool in many scientific disciplines[163].

2.2.4. Functional group analysis by Fourier transform infrared spectroscopy (FTIR)

Fourier transform infrared spectroscopy (FTIR) operates on the principle of light absorption in the infrared portion of the electromagnetic spectrum by most molecules in a sample. The resulting spectrum illustrates molecular absorption and transmission, effectively creating a molecular fingerprint characterized by absorption peaks that correspond to the vibrational frequencies of the bonds between atoms in the material. FTIR offers several advantages, including the ability to identify different materials, quantify the amount of material present by measuring peak sizes, determine the number of components in a mixture, and assess the quality or consistency of a sample.

Consequently, FTIR serves as a rapid and sensitive analytical technique for obtaining key information regarding the characterization of nanoencapsulation systems[164].

The principles of infrared spectroscopic technology are based on the atomic vibrations of molecules that absorb specific frequencies and energy levels of infrared radiation. Fourier-transform infrared (FTIR) spectroscopy enables the detection and classification of molecules, as each type of molecule exhibits a unique infrared spectrum. Figure 6 illustrates the operational workflow of FTIR. The FTIR spectrometer primarily employs an interferometer to assess the energy transmitted to the sample. Infrared radiation emitted from a black body reaches the interferometer, where the spectral encoding of the signals occurs. The resulting interferogram signal is either transmitted through or reflects off the sample surface, absorbing particular energy wavelengths. Finally, the beam travels through a detector and is then sent to a processing computer for the Fourier transformation of the energy signals[165].

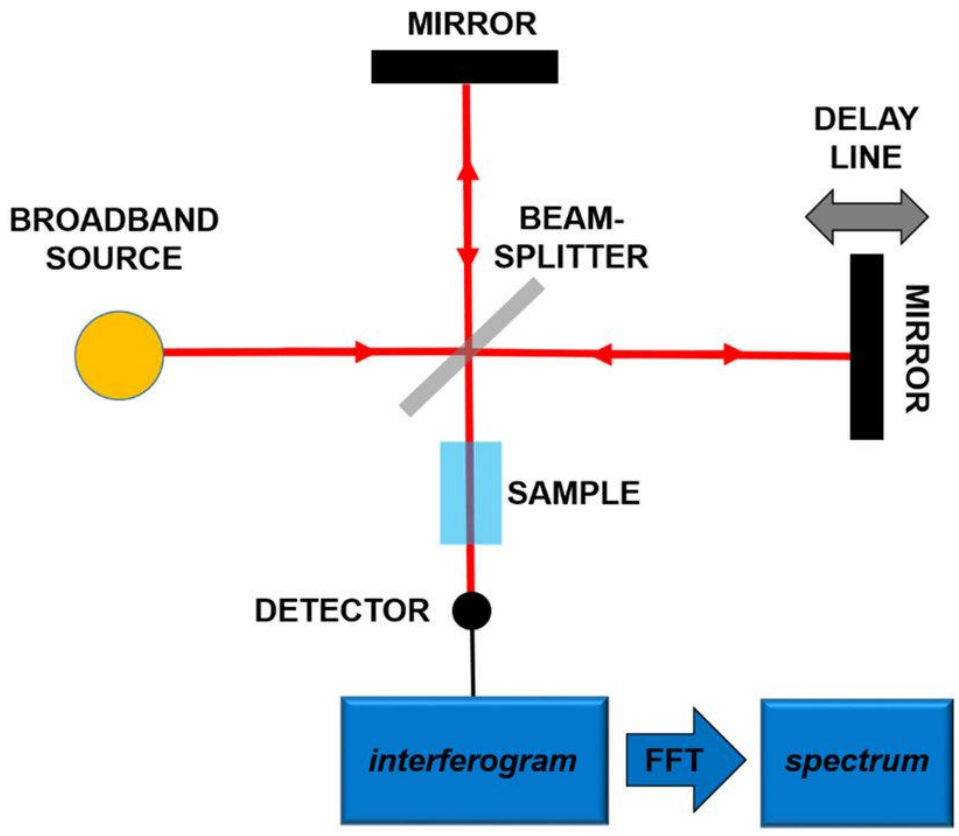

Figure 2.7. Fundamentals of Fourier-Transform Infrared Spectroscopy (FT-IR)[166].

2.2.5. Surface Topography

3D surface topography refers to the detailed representation of a surface's shape, texture, and features in three dimensions, utilizing various measurement techniques

such as stylus profilometry, optical interferometry, laser scanning microscopy, and atomic force microscopy. These methods collect height data over a defined area, which is then processed to reconstruct a 3D representation, often employing surface roughness parameters like Ra (arithmetic average roughness) and Rz (average maximum height of the profile) to quantify surface texture. The analysis focuses on surface features that impact properties like adhesion and wear resistance, with applications across materials science, microelectronics, and biotechnology. Ultimately, the processed data can be visualized in 3D models, enhancing the interpretation of surface characteristics and their influence on material behavior[35].

2.3. Substrate preparation

2.3.1. Ag/ITO preparation

Silver nitrate ($AgNO_3$) with a 99.8% purity level, sourced from Biochem Chemo Pharma in France, was dissolved in 12.5 ml of distilled water to create a 0.001M solution. Concurrently, sodium nitrate ($NaNO_3$) of 99.0% purity from the same supplier was dissolved in 12.5 ml of distilled water to achieve a 0.1M concentration. This higher concentration of $NaNO_3$ was used to improve the current conductivity in the solution, acting as a supporting electrolyte. The solutions of $AgNO_3$ and $NaNO_3$ were then combined in 25 ml of distilled water at room temperature. Indium tin oxide (ITO) conductive glass, measuring 1 cm x 2 cm with a thickness of 1 mm, was used as the substrate for electrodeposition. Prior to deposition, the ITO glass underwent thorough cleaning with acetone and distilled water, followed by drying at 30°C.

Electrochemical deposition was conducted using a standard three-electrode open cell configuration. The ITO-coated glass was positioned vertically as the working electrode (WE), with one side facing the counter electrode and only 1 cm immersed in the solution. The counter electrode (CE) was a platinum wire, 0.05 cm in diameter and 1 cm long. A calomel electrode ($Hg/Hg_2Cl_2/KCl$) served as the reference electrode (RE) and was in contact with the solution. To ensure consistency, all electrodes were rinsed with deionized water before and after each experiment. The electrodes were arranged with a separation of approximately 0.5 cm within the electrochemical cell. This setup allowed for precise control over the deposition process, influencing the energy, size, shape, and kinetics of the deposited materials. CVs experiments were conducted at ambient temperature using a PGZ 301 instrument, specifically the

DYNAMIC-EIS Voltammetry mode, and controlled by the VOLTAMASTER 4 V7.09 software (Serial no. 913V718/INT). The choice of an ITO glass electrode as the substrate for silver (Ag) electrodeposition is prevalent due to its favourable surface roughness characteristics.

The process of electroplating silver onto the ITO substrate involves the reduction of silver ions (Ag ions) leading to the formation of neutral silver atoms at the cathode, as detailed in the following procedure.

$$Ag^{+} + e^{-} \rightarrow Ag \qquad (2.19)$$

An external current supply was linked, enabling the deposition of silver ions onto the substrate through a reduction process. The quantity of silver atoms deposited on the substrate increases with higher silver ion concentrations, yet it's essential to ensure that the silver concentration does not exceed that of the supporting electrolyte. The deposition time and scanning rate play pivotal roles in the creation of multidimensional layers on the substrate surface.

2.3.2. NFMA/FTO preparation

Materials

Ethanol (C_2H_5OH), Methylene blue ($C_{16}H_{18}ClN_3S$), and Sulfuric acid (H_2SO_4) were procured from PubChem. N-(ferrocenylmethyl)aniline (NFMA) ($C_{17}H_{17}FeN$) and distilled water (H_2O) were sourced from the research laboratory "Valorisation and Technology of Sahara Resources (VTRS) in Eloued, Algeria." The working electrode, Fluorine-doped Tin Oxide (FTO), and an aqueous solution of Hydrogen peroxide (H_2O_2) were acquired from a commercial laboratory.

Apparatus and instruments

CV and chronoamperometric measurements were conducted using a PGZ 301 instrument with DYNAMIC-EIS capabilities, managed by VOLTAMASTER 4 V7.09 software (Serial no. 913V718/INT). The experiments were carried out in a three-electrode configuration at room temperature, employing an Ag/AgCl reference electrode. Structural characteristics of the modified electrodes were analyzed using X-ray diffraction (XRD). Surface topography and roughness were assessed with a Tencor P-7 mechanical profilometer. Measurements were taken under standard air conditions

and ambient temperature. The three-dimensional data were acquired using the 2-bar method, and a Gaussian filter with a 0.800-micrometer cut-off was applied to minimize edge effects.

2.4. Preparation of the FTO Electrode

Before modification, the FTO electrode underwent a thorough pre-treatment process to remove any residual impurities and ensure optimal surface cleanliness. This preparation began with immersing the electrode in acetone within an ultrasonic bath for 30 seconds. The ultrasonic treatment effectively dislodges contaminants from the surface by utilizing high-frequency sound waves, which create microscopic cavitation bubbles that aid in the removal of stubborn residues.

Following the acetone bath, the electrode was rinsed thoroughly with distilled water to remove any remaining solvent or loosened debris. It was then dried using a stream of nitrogen gas, which prevents the formation of water spots and minimizes the introduction of new contaminants. To further improve the surface cleanliness, the electrode was subjected to a heat treatment at 80ºC for 20 minutes. This heating step serves to evaporate any remaining moisture and ensures that the electrode surface is free of organic impurities. After the heat treatment, the electrode was rinsed again with distilled water to ensure complete removal of any residues generated during the cleaning process.

2.4.1. Electrochemical deposition of NFMA/FTO

The electrochemical behavior of a solution containing 0.01 g/mL NFMA ($C_{17}H_{16}NFe$), dissolved in a mixture of 9 mL ethanol and 3 mL of 0.1M H_2SO_4, was systematically explored using CV. The resulting CV curves, as shown in **Figure 2.5a**, reveal characteristic redox peaks within the potential range of 0 to 800 mV when scanned with the FTO glass electrode. These peaks correspond to the oxidation and reduction processes of NFMA, providing valuable information about the electrochemical properties of the system.

Additionally, the redox peaks remained stable over time, as evidenced by **Figure 2.5b**, which highlights the durability and consistency of the redox behavior under repeated scans. This stability suggests that NFMA maintains its electrochemical activity throughout the experimental period, making it a promising candidate for applications requiring long-term reliability, such as sensors or catalysis.

To modify the electrode with NFMA, a chronoamperometric technique was employed. A potential of 527 mV was applied for 7 minutes, facilitating the oxidation of NFMA on the electrode surface. Following this oxidation process, a coating technique was implemented, with the potential set to 263 mV, as indicated in **Figure 2.6**. This step allowed for the controlled electrodeposition of NFMA onto the FTO substrate.

After the deposition process, the modified electrode was thoroughly washed with distilled water to remove any unbound material and then dried at 70ºC for 2 hours to ensure a stable and uniform coating. This procedure produced a well-adhered NFMA film on the FTO surface, ready for further electrochemical testing or application. The meticulous preparation and modification steps contribute to the robustness and functionality of the NFMA-coated electrode, making it suitable for various electrochemical applications.

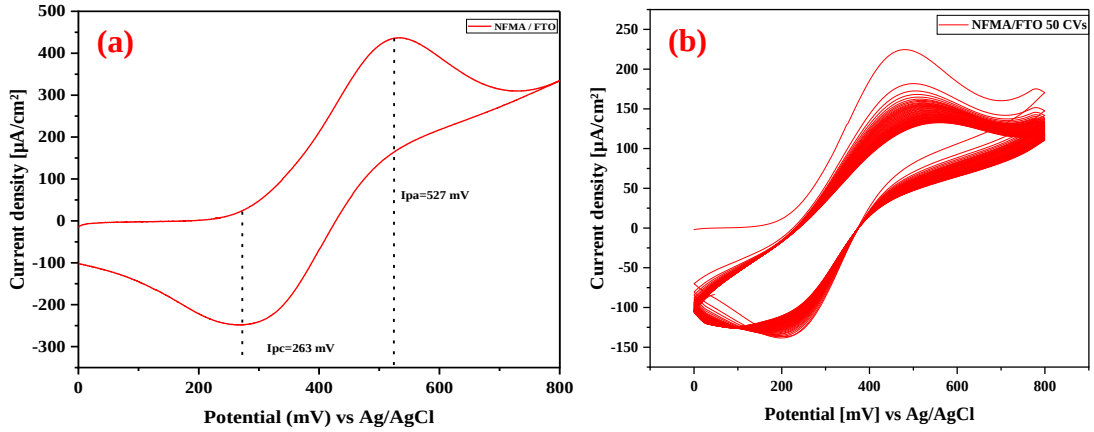

Figure 2.8. Cyclic voltammetry results, including (a) the cyclic voltammogram of NFMA-modified FTO with a scan rate of 50 mVs^{-1} and (b) 100 cycles of cyclic voltammetry recorded at the same scan rate of 50 mVs^{-1}.

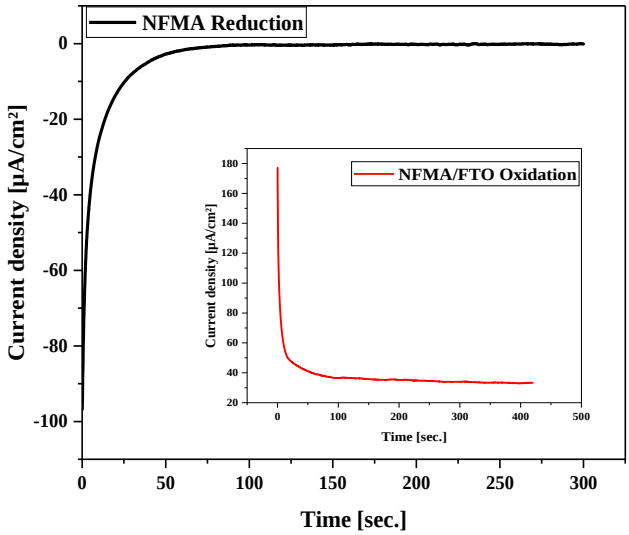

Figure 2.9. Chronoamperometry curve, illustrating oxidation and reduction processes involved in the growth of NFMA on the FTO electrode.

2.4.2. Chemical deposition of NFMA/ FTO

Prior to the immersion process, all glassware and the FTO electrode were meticulously cleaned to ensure the elimination of impurities that could affect the experiment's outcome. The cleaning procedure involved washing the materials with acetone (C_3H_6O) to dissolve any organic contaminants, followed by rinsing with distilled water to remove residual acetone. Afterward, the glassware and electrode were dried in a 70°C oven to ensure a contaminant-free surface before use.

A solution was then prepared by dissolving 0.01 g/mL of NFMA in 6 mL of ethanol in a beaker. The mixture was maintained at a constant temperature of 25°C to ensure stability and uniform dissolution of the NFMA. A 1 cm^2 section of the FTO electrode was carefully immersed in the solution for 5 minutes, allowing sufficient time for NFMA molecules to interact with the electrode surface.

After completing the immersion process, the electrode was gently extracted from the solution and thoroughly rinsed with distilled water to remove any unbound NFMA or other potential contaminants. Finally, the electrode was subjected to a drying process in a 70°C oven for 2 hours. This step ensured the complete evaporation of any residual solvent and the stabilization of the NFMA coating, preparing the electrode for subsequent applications or electrochemical testing.

2.4.3. Preparation of Cu_2O/ITO via Electrochemical Method

The electrochemical properties of a solution containing 0.005 g/mL $CuSO_4$ and 0.285 g/mL H_2SO_4 dissolved in 20 mL of distilled water were systematically investigated using cyclic voltammetry (CV) over a potential range of -600 to 200 mV. The CV results, illustrated in **Figure 2.7**, demonstrate the characteristic redox peak behavior of the ITO glass electrode during the scanning process from -600 to 200 mV. These redox peaks are indicative of the electrochemical reactions involving copper species, which play a crucial role in the formation of Cu_2O on the ITO substrate.

To fabricate the Cu_2O /ITO electrode, the electrodeposition technique was employed, allowing for the controlled deposition of copper oxide onto the ITO surface. Following the electrodeposition, the electrode was thoroughly washed with distilled water to remove any unbound or excess material, ensuring a clean and uniform coating. Subsequently, the electrode was dried at a temperature of 70°C for 2 hours, a crucial step that facilitates the stabilization of the Cu_2O layer and enhances its adhesion to the substrate.

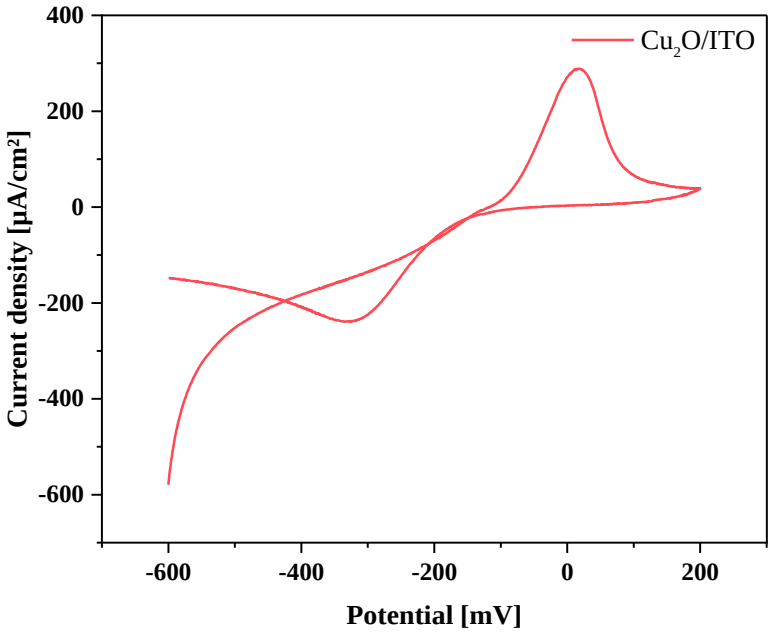

Figure 2.10. The characteristic redox peaks of Cu_2O on the ITO glass electrode after cyclic voltammetry scanning from -600 to 200 mV.

2.4.4. Preparation of NFMA/Cu_2O/ITO via Immersion Method

In order to prepare NFMA/Cu_2O/ITO using the immersion method, it is necessary to clean all glassware and the Cu_2O/ITO electrode meticulously with acetone (C_3H_6O), rinse them with distilled water, and then dry them in an oven at a

temperature of 70°C. A beaker was used to make a solution at 25°C by combining 0.01 g/mL of NFMA with 6 mL of ethanol. The Cu_2O /ITO electrode, with a surface area of 1 cm^2, was submerged in the solution for a duration of 5 minutes. Following immersion, the electrode was rinsed with distilled water to eliminate any contaminants and then dried at a temperature of 70°C for a duration of 2 hours in anticipation of subsequent utilization. The effectiveness of the NFMA/Cu_2O/ITO thin film in photocatalysis was assessed by observing the decomposition of Rose Bengal (RB) in the presence of sunshine. A 1 part per million (PPM) solution of RB was created by dissolving RB in 500 mL of double-distilled water. The solution was agitated using a magnetic stirrer for 15 minutes and then left in a dark environment for 30 minutes.

For the photocatalytic degradation experiment, an NFMA/Cu_2O/ITO sample with a surface area of 1 cm^2 was placed in a solution of RB with a volume of 40 mL. The sample was positioned at an angle of 45° +/- degrees to optimize exposure to sunshine. Specimens from the amalgamation were gathered every 60 minutes for a span of 180 minutes. The variation in absorbance was quantified using a spectrophotometer (UV-VIS JASCO V-770) across the wavelength range of 400 to 900 nm.

2.5. Applications preparation

2.5.1. Photocatalysis of MB

The NFMA/FTO thin-film's photocatalytic performance was evaluated by assessing its capacity to degrade MB under sunshine irradiation, taking into account the specific weather circumstances on April 18th, 2023, at El Oued, Algeria. In order to create the MB solution, which mimics wastewater, 1 part per million (PPM) of MB was dissolved in 500 mL of double-distilled water and then agitated using a magnetic stirrer for a duration of 15 minutes. Subsequently, the resultant solution was placed in a light-restricted environment for a duration of 30 minutes to guarantee stabilization.

In the experiment on photocatalytic degradation, an NFMA/FTO sample with an area of 1 cm^2 was submerged in a solution of 40 mL of MB and placed at an angle of roughly 50 degrees to optimize sunshine exposure. Different samples were extracted from the MB solution at regular 30-minute intervals throughout the 180-minute reaction period to examine their absorbance. The change in absorbance was measured using a spectrophotometer (UV-VIS JASCO V-770) that operated between

wavelengths of 400 to 900 nm. Afterwards, the rate of photocatalytic efficiency, which represents the percentage of degradation, was determined using the following formula:

$$\% D = (C_0 - C_t / C_0) * 100 \quad (2.20)$$

where C_0 represents the initial concentration at time 0, and Ct represents the concentration at time t. The calculation of the rate constant (K_{app}) follows the equation:

$$r = -dC.dt = K_{app}.C \quad (2.21)$$

"r" signifies the constant rate, "C" denotes the concentration of MB, "t" represents time, and "K_{app}" (expressed in units of min^-1) stands for the pseudo-first-order rate constant.

2.5.2. Detection of H_2O_2

The NFMA/FTO sensor platforms that were fabricated were employed to detect varying concentrations of hydrogen peroxide, specifically ranging from 20 µL to 100 µL, using electrochemical techniques. The experiments were conducted in a 0.1 M Na_2SO_4 solution at ambient temperature, utilizing a three-electrode cell configuration to facilitate accurate measurements.

In this setup, the working electrode comprised a 1 cm^2 surface area of NFMA/FTO, which is critical for achieving optimal sensitivity and response during detection. The counter electrode was constructed from a platinum wire, providing a stable and inert surface for the necessary electrochemical reactions. To maintain potential stability and enhance measurement precision, a custom-built Ag/AgCl reference electrode was utilized, which is known for its reliability in electrochemical applications.

This experimental design allows for the effective monitoring of hydrogen peroxide concentrations through the electrochemical response of the NFMA/FTO sensor, leveraging the unique properties of the NFMA material to achieve accurate and reproducible results. The findings from these measurements are significant for applications in environmental monitoring, biomedical diagnostics, and other fields where precise detection of hydrogen peroxide is essential.

Chapter 3

Results and Discussion

Chapter 3: Results and Discussion

3.1. Electrochemical Deposition of Ag Nanoparticles on ITO-Coated Glass: Effect of Different Cyclic Voltammetry Scan Rates on Ag Deposition

Cyclic voltammetry (CV) was employed to investigate the deposition potential of silver (Ag) by varying the voltage range from -100 mV to -700 mV across different scan rates, resulting in a voltammogram. **Figure 3.1** illustrates the electrochemical processes taking place on the surface of the ITO glass electrode, displaying distinct oxidation and reduction peaks. The reduction peak, located between -100 mV and -200 mV, corresponds to the deposition of silver onto the ITO glass substrate. This reduction signifies the transition of Ag^+ ions into metallic silver on the electrode's surface. As the voltammogram progresses, these peaks exhibit increasingly negative values until reaching their maximum potential. Additionally, the oxidation peak, appearing between 300 mV and 400 mV, represents the reverse oxidation process, where silver is oxidized back into its ionic form. These peaks offer insight into the deposition and stripping processes of silver on the ITO glass surface, revealing key electrochemical properties critical to the development of electrode-based systems.

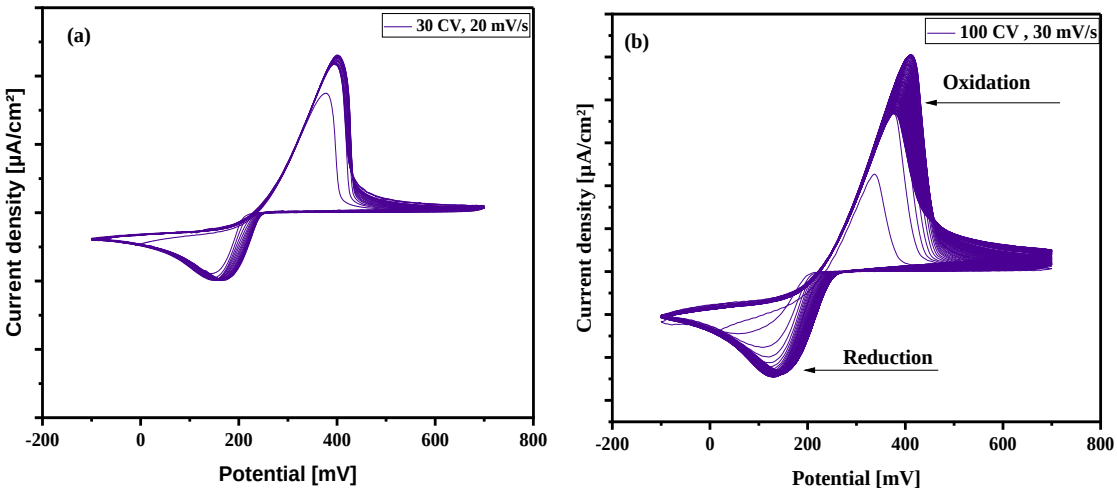

Figure 3.1. Cyclic voltammograms of Ag/ITO system under two different experimental conditions: (a) 20 cyclic voltammetry (CV) scans performed at a current density of 10 µA/cm². (b) 100 CV scans conducted at a current density of 30 µA/cm².

To elucidate the electrodeposition mechanism responsible for coating silver (Ag) onto ITO glass, a controlled experiment was conducted wherein a solution containing

13 mL of 0.1 M $AgNO_3$ was incrementally introduced into the electrochemical system. Specifically, 1 mL of $AgNO_3$ was added each time a voltammetry curve was recorded at a scan rate of 30 mV/s.

The recorded voltammetry curves revealed a notable change in current density, shifting in the negative direction, which indicates a reduction reaction occurring at the electrode surface. This reduction leads to the formation of Ag ions (Ag^+) as metallic silver begins to deposit onto the ITO substrate.

As the volume of the $AgNO_3$ solution was progressively increased, the conductivity of the ITO glass initially exhibited a gradual rise, reflecting the enhanced ionic concentration in the solution. Notably, this conductivity continued to increase until it reached a volume of 8 mL, at which point a relative decline in conductivity was observed. This decline suggests that a saturation point may have been reached, potentially indicating a shift in the deposition dynamics or the onset of competitive reactions on the electrode surface. Interestingly, after reaching a volume of 8 mL, the conductivity began to increase again from 9 mL onward, implying a subsequent enhancement in ionic activity and further deposition of Ag ions.

This series of observations underscores the dynamic nature of the electrodeposition process, providing compelling evidence that the surface of the working electrode underwent significant alteration as it became coated with Ag^+ ions (as illustrated in **Figure 3.2**).

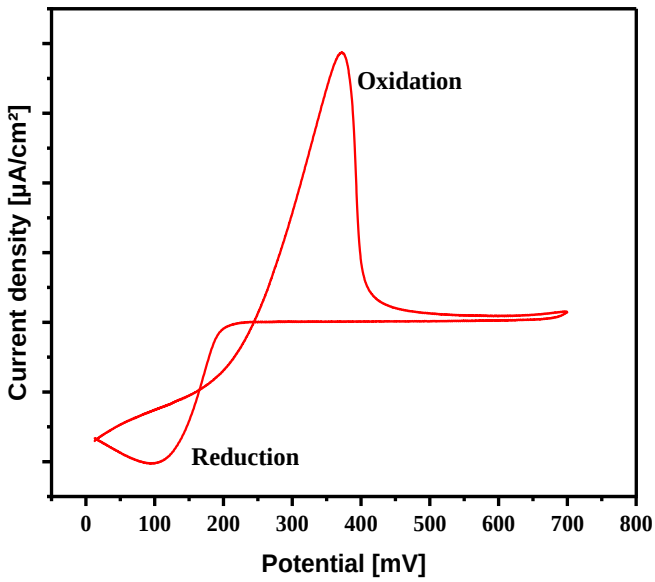

Figure 3.2. Electrodeposition mechanism in the ITO/Ag system.

As depicted in **Figure 3.3**, the current peak observed in a cyclic voltammogram was generated using a solution composed of 25 mL of C_{NaNO3} at a concentration of 0.1 M, while C_{AgNO3} remained at a concentration of 0 M. This result clearly indicates the successful deposition of silver (Ag), with Ag effectively occupying all available sites on the ITO electrode. Calibration curves were generated by plotting the anodic peak height (current) against varying concentrations of silver nitrate. Key validation parameters, including linearity, limit of quantification (LOQ), precision, and limit of detection (LOD), were assessed. CVs of $AgNO_3$ solutions were recorded across a concentration range of 0.001 to 0.005 mM within a 0.1 M $NaNO_3$ solution at room temperature.

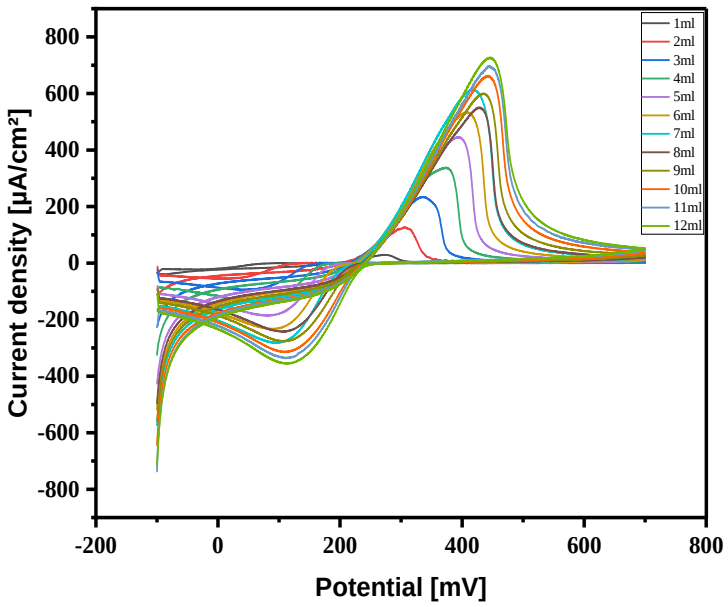

Figure 3.3. Depicts a voltammogram obtained from an ITO-coated electrode in a solution containing 0.1 M of $NaNO_3$ and 0 M of $AgNO_3$.

The calibration curves for silver nitrate were obtained using the data collected during these cyclic voltammetric tests. **Figure 3.4** displays the calibration curve that shows the correlation between the concentration of silver nitrate and the electric current for ITO electrodes. Cyclic voltammetric measurements were conducted on silver nitrate solutions with linear values ranging from 0.001 mM to 0.005 mM. **Figure 3.4** displays the anodic current linked to silver nitrate, plotted against the concentration of $AgNO_3$. We then performed a linear regression analysis on the collected data. The calibration curve obtained using ITO electrodes resulted in a correlation coefficient

(R^2) of 0.976. The linear regression equation allows for the estimate of the residual concentration of $AgNO_3$ after the electrodeposition procedure. In order to verify the precision of this calibration curve, we exposed a small layer of silver on an indium tin oxide (ITO) glass substrate to a certain duration of analysis. Afterwards, we identified the maximum value of the anodic current in cyclic voltammetry in order to examine its influence on the calibration curve.

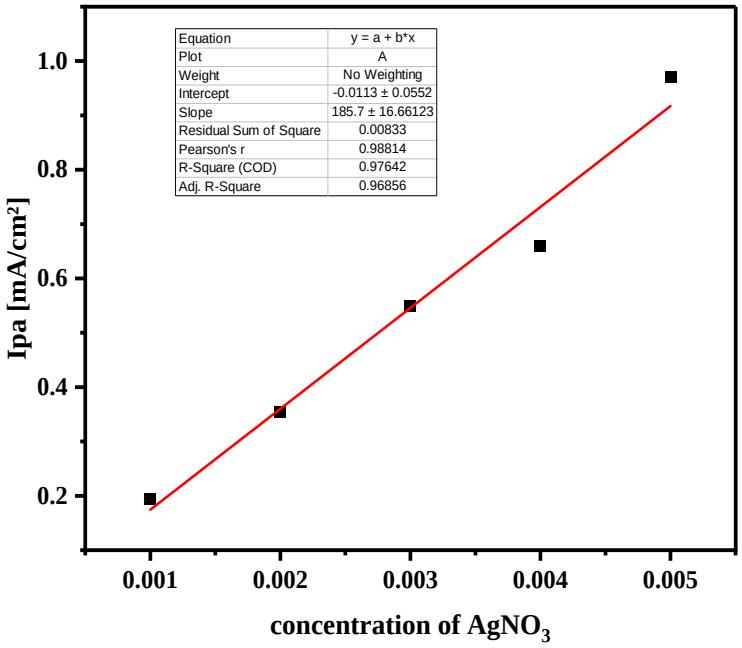

Figure 3.4. Illustrates the calibration curves representing the relationship between current density and various concentrations of $AgNO_3$.

In an aqueous solution, cyclic voltammograms were conducted to analyze the behavior of $AgNO_3$ and $NaNO_3$. These experiments involved varying the scan rate from 10 to 120 mV/s, resulting in distinct cathodic current peaks (Ipc) at different scan rates (v). **Figure 3.5** displays a graph illustrating the relationship between (Ipc) and (v1/2) across the potential range of -1 to +7. As illustrated in **Figure 3.5**, the cathodic peak (Ipc) exhibited a linear increase corresponding to the scan rate increment. In accordance with the Scharifker–Hills hypothesis[167], there are two scenarios for metal deposition based on the initial surface density of nucleation. The first scenario, termed the instantaneous nucleation process, occurs when an alteration in nucleation density can be achieved through increased polarization. This heightened polarization results in an augmented nucleation rate until depletion occurs due to an insufficient number of nucleation sites.

$$I(t)ins = \frac{zFD^{1/2}c}{\pi t^{1/2}}[1 - e^{-N_0\pi kDt}] \quad (3.1)$$

$$\text{Where } k = \sqrt{\frac{(8\pi cM)}{\rho}} \quad (3.2)$$

Furthermore, progressive nucleation takes place when there is a high initial nucleus density at the outset of growth, and the nucleation rate significantly outpaces the rate of growth. This results in a slow growth process due to the overlapping diffusion profiles of Ag ions, as indicated by the following equation[167]:

$$I(t)ins = \frac{zFD^{1/2}c}{\pi t^{1/2}}[1 - e^{-N_0\pi kDt}] \quad (3.3)$$

$$where: \qquad k = \frac{4}{3}\sqrt{\frac{(8\pi cM)}{\rho}} \quad (3.4)$$

And A is the nucleation rate constant.

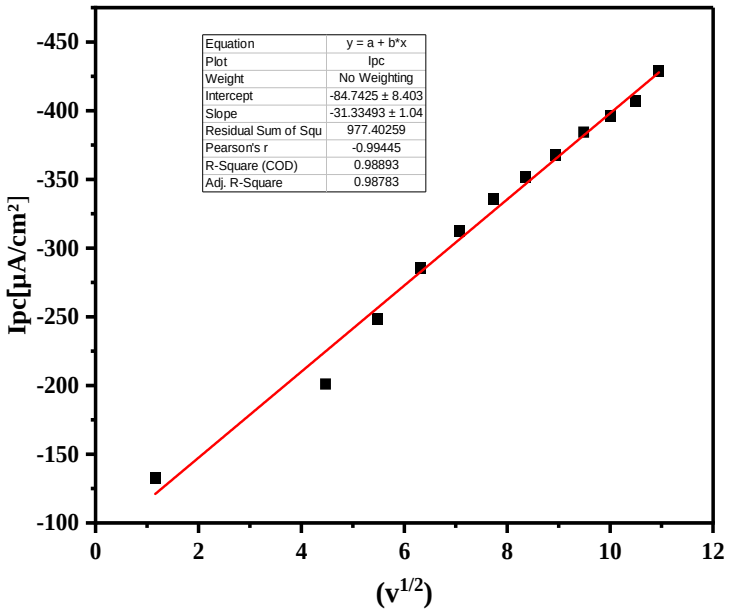

Figure 3.5. Linear correlation between the cathodic peak (Ipc) and the square root of the scan rate ($v^{1/2}$) for the ITO/Ag electrode.

2.1.1. Structural properties

The structural characterization of the synthesized nanoparticles was performed using X-ray diffraction (XRD) analysis, as depicted in **Figure 3.6**, which illustrates the XRD patterns of silver nanoparticles deposited onto ITO substrates under varying

deposition conditions. In the commercial ITO sample, distinct diffraction peaks associated with ITO are clearly identified, corroborating the data presented in **Figure 3.6.** Particularly, the diffraction peak at $2\theta = 30.37°$ corresponds to the body-centered cubic phase of indium oxide (according to JCPDS file No. 06-0416).

A key observation from **Figure 3.6(a,b)** is the appearance of a prominent diffraction peak attributed to silver. Based on JCPDS card No. 04-0783, which describes Face-Centered Cubic (FCC) structures, the most intense peak is typically aligned with the (1 1 1) plane, a feature that is consistently observed in our samples. The sharpness and intensity of this peak are indicative of a high degree of crystallinity in the silver nanoparticles, further substantiated by the narrow width of the peaks, which suggests a relatively small crystallite size. The broadening of these peaks is characteristic of nanoscale dimensions, as it is often associated with the reduction in crystallite size according to the Scherrer equation.

The diffraction peak at $2\theta = 38.08°$ provides further evidence of the successful crystallization of Ag^{+} ions into a well-defined silver phase. Furthermore, the significantly higher intensity of the silver peaks in comparison to those of ITO indicates that silver growth preferentially occurred along the crystal planes, specifically the (1 1 1) plane. This dominance suggests that the silver nanoparticles exhibited oriented growth with a preferred crystallographic direction, which may have implications for the physical properties and potential applications of these materials. The enhanced crystallinity and intensity of the silver reflections underscore the effectiveness of the deposition process and provide insight into the underlying growth mechanisms governing nanoparticle formation on ITO substrates.

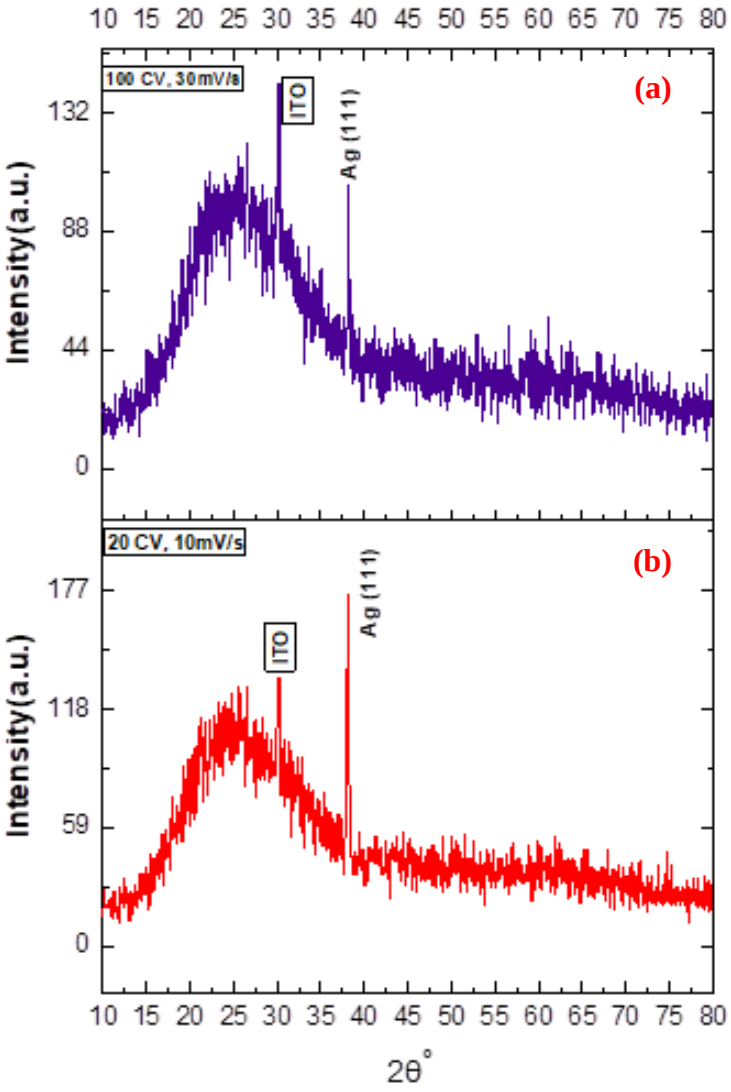

Figure 3.6. X-ray diffraction (XRD) patterns for silver deposition onto ITO substrates at different scan rate (a) 30 mV/s and (b) 10mV/s.

Table 3.1 X-ray diffraction parameters.

Phase	2theta °	d-spacing	FWHM (°)	Crystalline size (nm)
Ag	38.08	2.36316	0.15941	52.69
ITO	30.19658	2.95973	0.42509	19.349

2.1.2. Morphological properties

The surface morphology of Ag^{+} ions deposited on ITO glass substrates, specifically their size, shape, and distribution, was analyzed using scanning electron microscopy (SEM). **Figure 3.7 (a, b)** presents the SEM images of silver nanoparticles

formed under different conditions: during 20 cyclic voltammetry (CV) scans at a scan rate of 10 mV/s and 100 CV scans at 30 mV/s, within the potential range of -1 to +7 V.

The SEM analysis reveals the formation of relatively larger silver nanoparticles, which can be explained by the inherent tendency of Ag nanoparticles to aggregate. This aggregation behavior is primarily driven by the high surface energy associated with nanoscale silver particles, which leads to an increase in surface tension. As ultrafine nanoparticles possess a larger surface area relative to their volume, they exhibit heightened surface energy, promoting particle-particle interactions and agglomeration. Consequently, the formation of larger nanoparticles is observed, particularly under conditions where the number of CV scans is increased, as seen in **Figure 3.7b**.

The observed surface characteristics suggest that the deposition method and scanning parameters play a crucial role in controlling nanoparticle size and distribution on the ITO substrate. The tendency of silver nanoparticles to aggregate can impact their functional properties, including electrical conductivity and catalytic activity, and thus must be carefully managed in applications where precise control over nanoparticle size is critical.

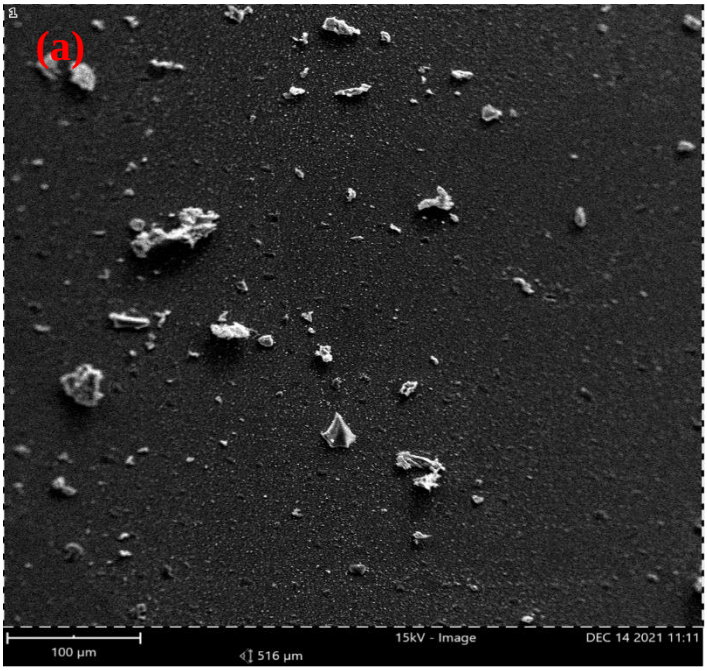

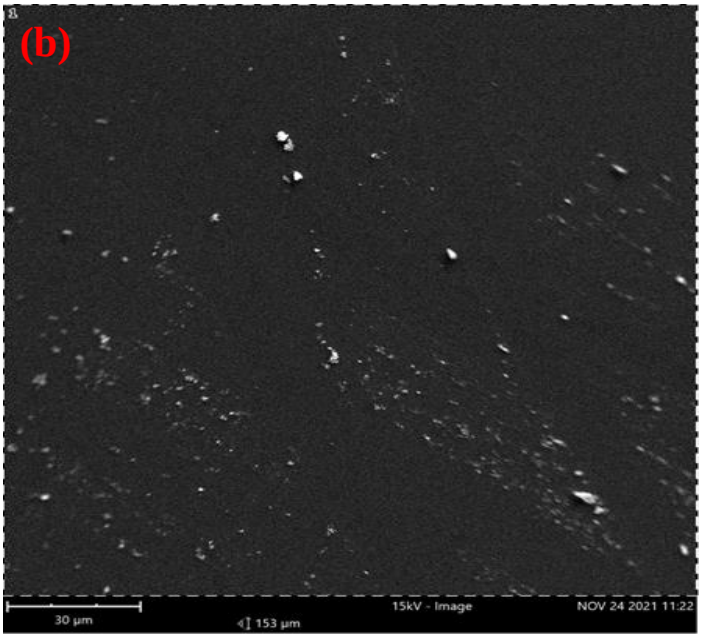

Figure 3.7. Scanning electron microscopy (SEM) images of the ITO/Ag electrodeposited within the voltage range of -1 to +7 V.**(a)** 20 cyclic voltammetry (CV) scans at a scan rate of 10 mV/s **(b)** 100 CV scans at 30 mV/s

2.1.3. Optical properties

The optical characterization of Ag^+ ions within thin films is influenced by both their internal structure and the distances between individual particles, factors that are contingent upon the experimental conditions employed. The assessment of visible transmittance can be carried out using methods such as UV and FTIR spectroscopy. In **Figure 3.8**, the optical transmittance of the ITO/Ag-coated substrates is presented using UV spectroscopy. Based on the transmittance data depicted in **Figure 3.8**, it is evident that the substrate's structure plays a crucial role in dictating its optical properties. The UV-visible transmittance spectra of the ITO glass **(Figure 3.8a)**, used as a reference, exhibited a transmittance of 100%. Notably, characteristic peaks attributed to silver were observed at 324 and 323 nm. The sample subjected to 100 cyclic voltammetry scans at a scan rate of 30 mV/s exhibited greater thickness and consequently displayed a slightly lower optical transmittance, as this condition led to the formation of a thicker layer of silver **(Figure 3.8b)**. Conversely, the sample subjected to 20 cyclic voltammetry scans at a scan rate of 10 mV/s exhibited an increase in optical transmittance as shown in **Figure 3.8c**. Importantly, all the samples exhibited high optical transmittance and maintained clear transparency within the visible light wavelength range of 300-900 nm.

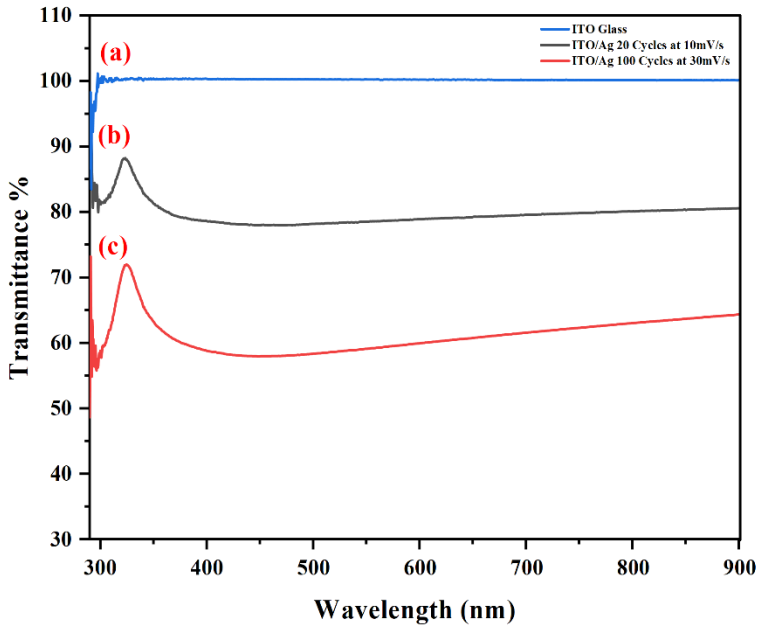

Figure 3.8. UV-visible spectra of Ag/ITO substrates: (a) the ITO glass, (b) Ag/ITO deposited at a scan rate of 10 mV/s, and (c) Ag/ITO deposited at a scan rate of 30 mV/s.

FTIR spectroscopy was employed to analyze and quantify the functional groups present in the material, providing valuable insights into the chemical composition and bonding environment. The identification of specific functional groups was facilitated by comparing the recorded absorption peaks with reference spectra from the literature. **Figure 3.9** illustrates the FTIR spectra, highlighting the characteristic transmittance bands for the two samples under investigation. A prominent absorption peak at 2104 cm^{-1} is observed, corresponding to the stretching vibrations of C≡C bonds, consistent with previously reported values. This peak suggests the presence of unsaturated carbon-carbon bonds, indicative of certain organic or polymeric species[168]. Additionally, a band at 892 cm^{-1} is attributed to the bending vibrations of C-H bonds, further confirming the presence of hydrocarbon groups within the material's structure.

The emergence of a peak at 1354 cm^{-1} is particularly noteworthy, as it can be attributed to the O-H stretching mode. This observation is likely due to the interaction of water molecules with the silver nanoparticle surface, suggesting a degree of surface hydration or adsorbed moisture. This water interaction may play a significant role in influencing the surface chemistry and reactivity of the silver.

Furthermore, a distinct peak at 767 cm^{-1} is associated with the C-H bending vibrations of a (meta) configuration, providing additional confirmation of the presence of specific hydrocarbon frameworks[169].

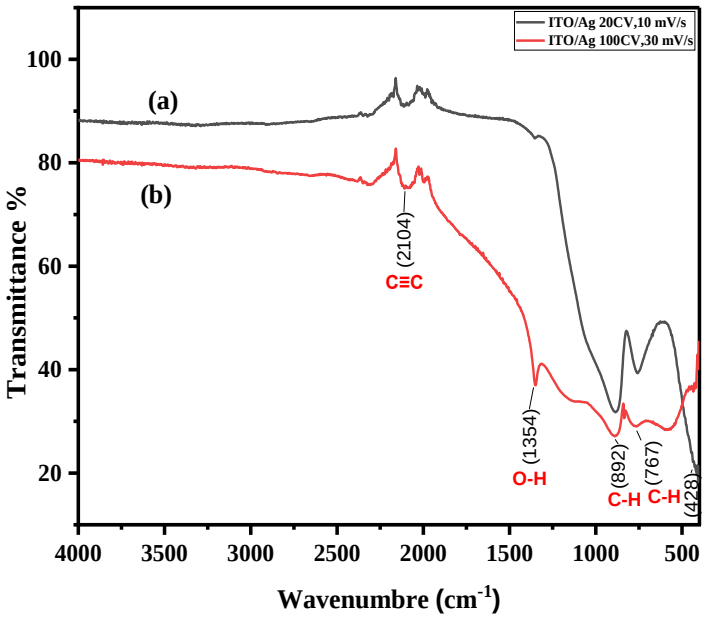

Figure 3.9. FTIR spectra: (a) after 20 cyclic voltammetry scans at a scan rate of 10 mV/s, and (b) after 100 cyclic voltammetry scans at a scan rate of 30 mV/s.

2.1.4. Conclusion

The successful electrochemical characterization of silver nanoparticles on ITO-modified electrodes was achieved. Cyclic voltammetry was employed within a potential range spanning from -1 to +7 V, with variations in the number of cycles and scan rates, to assess the electrodeposition process of $AgNO_3$ on the modified ITO electrode surface. The SEM analysis unveiled the surface morphology of Ag on ITO electrodes, showcasing the deposition of nanoclusters. X-ray diffraction (XRD) analysis demonstrated that the ITO/Ag films on both samples exhibited crystalline properties with a preference for orientations along the hkl (111) directions. Additionally, FTIR spectroscopy provided confirmation of the successful formation of silver on the ITO surface. These findings indicate the creation of a homogeneous structure with morphological surface features characterized by high efficiency and favorable optical properties. Such attributes make these materials potentially valuable for applications in solar cells.

2.2.NFMA/FTO Electrochemical Thin Film

2.2.1. X-ray diffraction

The X-ray diffraction patterns obtained through electrodeposition of NFMA/FTO exhibit distinct and well-defined diffraction peaks in contrast to those obtained through the immersion technique. In **Figure 3.10a**, it is evident that various peaks are observed at 2θ = 17.12° and 22.90°, indicative of the polycrystalline nature of the NFMA/FTO thin film with higher crystallinity. This suggests that the electrodeposition method results in a more favorable condition for efficient charge transport when compared to film deposition by immersion. Conversely, when using the immersion technique (as shown in **Figure 3.10b**), only one peak is observed at 2θ = 22.80°, corresponding to N-(ferrocenylmethyl)aniline.

According to the JCPDS database (reference: 029-1711), under standard conditions, ferrocene's solid phase is characterized as a molecular crystal with a monoclinic unit cell (space group P21/a) featuring the following parameters: a = 10.53 Å, b = 7.61 Å, and c = 5.93 Å. The primary peaks associated with ferrocene are located at smaller angles of 2θ ∼ 10−30° in the X-ray diffractograms (**Figure 3.10a and b**). Moreover, the transformation of organic molecular crystals induced by elevated temperatures and pressures within the moderate temperature range is commonly associated with processes such as the transition to an amorphous state and structural phase changes[170]. The X-ray diffraction (XRD) pattern of the electrode that underwent electrodeposition is depicted in **Figure 3.10a**, displaying a solitary peak at 2θ = 22.80°, corresponding to the (210) and (001) reflections of NFMA. This observation suggests a high degree of crystalline quality in the modified FTO electrode. To ascertain the grain size of the crystalline structure in each electrode, we applied the Scherrer **equation 5**, yielding an average value of approximately 68 nm[171].

$$L = (K \cdot \lambda) / (\beta \cdot \cos\theta) \quad (3.5)$$

Where L is crystallite size

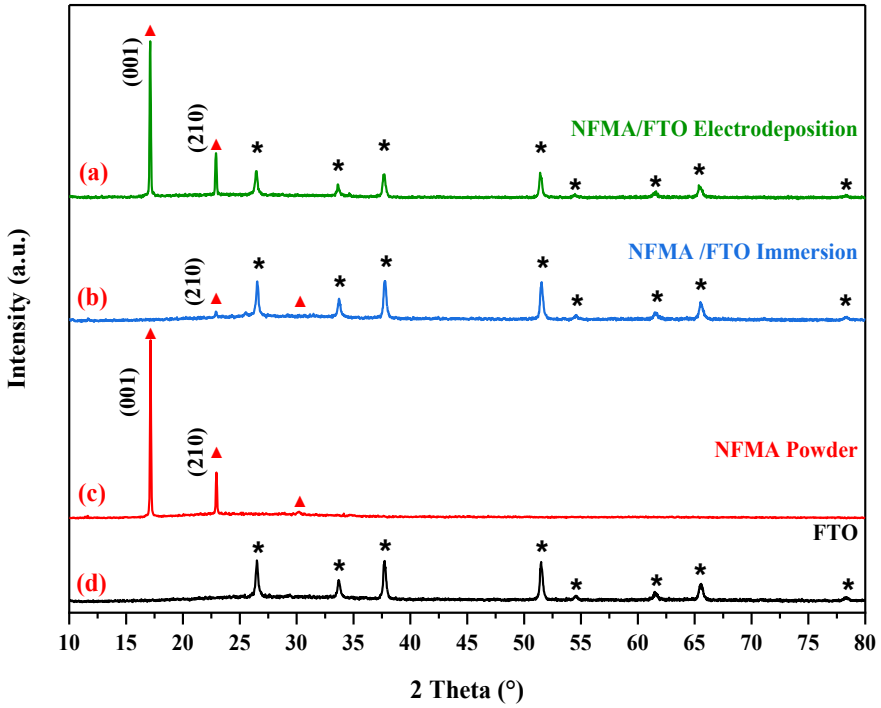

Figure 3.10. Illustrates the X-ray Diffraction patterns for(a) NFMA/FTO obtained through the electrodeposition method, (b) NFMA/FTO through the immersion method, (c) the XRD pattern of N-(ferrocenylmethyl)aniline, and (d) the XRD pattern of FTO glass.

2.2.2. Scanning electron microscopy (SEM)

Scanning electron microscopy (SEM) analysis was conducted on NFMA/FTO glass electrodes to investigate the film structure's characteristics. The SEM images depicted in **Figure 3.11a** exhibited the surface of the uncoated FTO, while **Figure 3.11b** demonstrated that the particle shapes on the surface were similar for both deposition methods. Consequently, it was observed that the electrodeposition method yielded a more uniform thin film compared to the immersion deposition method, which displayed less uniformity. The formation of the NFMA film on the FTO substrate can be described as occurring in two phases: Initially, NFMA material was deposited onto a modified FTO electrode at room temperature, resulting in the formation of a uniform film. Subsequently, as the temperature increased, nuclei gradually developed, leading to the formation of particles approximately 68 nm in size, as confirmed by XRD analysis.

The morphology of the NFMA film plays a crucial role in influencing the charge transport within the NFMA/FTO structure. As depicted in **Figure 3.11b**, the growth of nuclei on the FTO surface via the immersion technique exhibited less uniformity compared to the electrodeposition method. Consequently, it can be concluded that

electrodeposition of NFMA on FTO is a more suitable process when utilizing the electrochemical method for deposition. However, it is noteworthy that this specific morphology has been effectively utilized to estimate the electrical conductivity of compounds derived from NFMA on FTO.

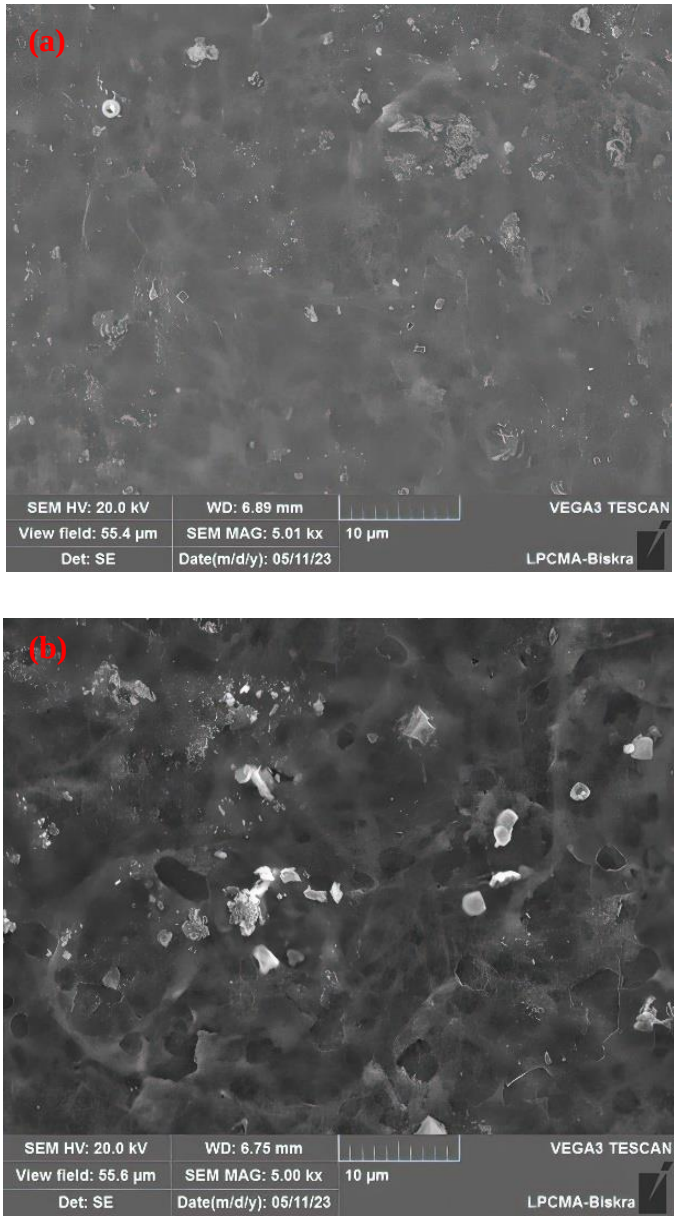

Figure 3.11. Scanning electron microscopy (SEM) images of the NFMA/FTO electrode that was constructed using two different methods: (a) electrodeposition and (b) the immersion technique.

2.2.3. Investigation of Three-Dimensional Surface Topography

The 3D surface topography, as depicted in **Figure 3.12**, offers a detailed visualization of the surface roughness characteristics observed on the NFMA/FTO glass substrate. A thorough analysis of the topographical features indicates that the immersion method significantly increases surface roughness and introduces a higher degree of surface heterogeneity. Quantitatively, the root-mean-square roughness (Rq)

values, which provide a statistical measure of surface roughness, were calculated to be 68 nm for the electrodeposition technique and 110 nm for the immersion technique. This stark contrast underscores the substantial effect of the deposition method on surface morphology.

In addition to roughness, the analysis also highlights variations in peak height across the two methods. The electrodeposition method produced a maximum peak height (Rp) of 1.1 μm, while the immersion method yielded a lower peak height of 0.5 μm. These findings suggest that the electrodeposition process fosters the development of more prominent surface features, whereas the immersion technique results in a relatively smoother, but more uneven, surface.

The distinct differences in surface topography between the two methods emphasize the critical role that the deposition technique plays in shaping the surface characteristics of NFMA/FTO glass. These surface properties are crucial, as they can influence the material's performance in various applications, including its electrical conductivity, catalytic activity, and interaction with external environments. The increased surface roughness and heterogeneity achieved through immersion could have implications for enhancing surface area and reactivity, whereas the more controlled roughness produced by electrodeposition might be favorable for applications requiring precise surface features.

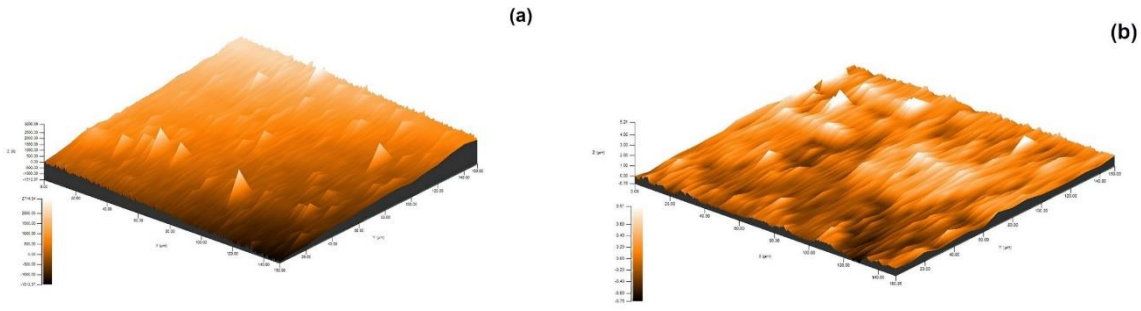

Figure 3.12. The three-dimensional surface characteristics of the NFMA/FTO electrode, which were assessed through two separate manufacturing methods: (a) electrodeposition and (b) deposition via the Immersion approach.

2.2.4. Water droplet contact angles analysis

The water contact angle measurement provides critical insights into the wettability of NFMA, particularly the nature of its interaction with water molecules at the material interface. The contact angle results, illustrated in **Figure 3.13**, offer a clear comparison of the hydrophobic properties of NFMA under different preparation

methods. As shown in **Figure 3.13a**, the NFMA/FTO electrodeposited surface exhibits a contact angle of 73.86°, indicating a moderately hydrophobic surface. This hydrophobicity can be largely attributed to the presence of nonpolar H–C bonds within the NFMA structure, which reduces the material's affinity for water molecules. This hydrophobic nature is noteworthy because it can enhance the sensitivity for detecting H_2O_2 and promote effective photoelectrochemical degradation processes, making it advantageous for applications in environmental sensing and catalysis.

In contrast, NFMA/FTO prepared via the immersion technique showed a slightly higher water contact angle of 78°, as seen in **Figure 3.13b**. This marginal increase in hydrophobicity can be attributed to the greater presence of NFMA ions on the FTO surface, which may contribute to a more structured or less interactive surface with water molecules. The increase in contact angle suggests that the immersion method results in a more hydrophobic surface, though the difference between the two methods is subtle.

Overall, the variation in water contact angles between the electrodeposition and immersion methods underscores the influence of fabrication techniques on the surface chemistry of NFMA/FTO. The slight difference in hydrophobicity between the two approaches could have important implications for their use in applications where surface wettability plays a key role, such as in sensors, photocatalysis, or electrochemical reactions. The hydrophobic nature of these surfaces may also contribute to enhanced stability and selectivity in aqueous environments, further highlighting the relevance of these findings for practical applications.

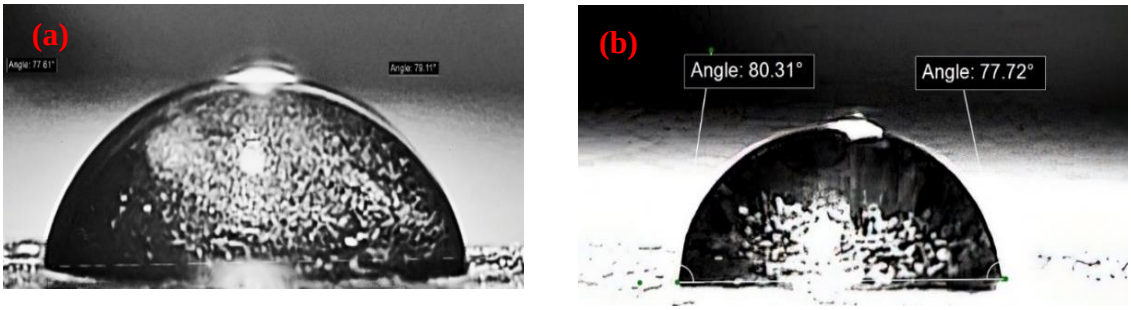

Figure 3.13. The water contact angle measurements for (a) the NFMA/FTO electrodeposition and (b) the NFMA/FTO fabricated via the immersion technique.

2.2.5. The optical energy gap

To further investigate the optical properties and durability of NFMA, UV-visible absorption spectroscopy was performed, providing valuable insights into its electronic

structure. **Figure 3.14** presents the UV-visible absorption spectra of NFMA dissolved in ethanol. A distinct absorbance peak is observed at 437 nm, as shown in **Figure 3.14a**, which is indicative of the material's ability to absorb light in the visible region of the spectrum.

Further analysis of the UV-visible data allowed for the calculation of the direct band gap (Eg) of the NFMA solution, which was determined to be 2.4 eV, as illustrated in **Figure 3.14b**. This band gap value places NFMA within the semiconductor range, a characteristic that positions it as a promising candidate for applications in photovoltaic technologies. The band gap energy is particularly suitable for efficient light absorption and charge separation, which are essential properties for materials used in solar energy conversion and other photoactive systems.[172].

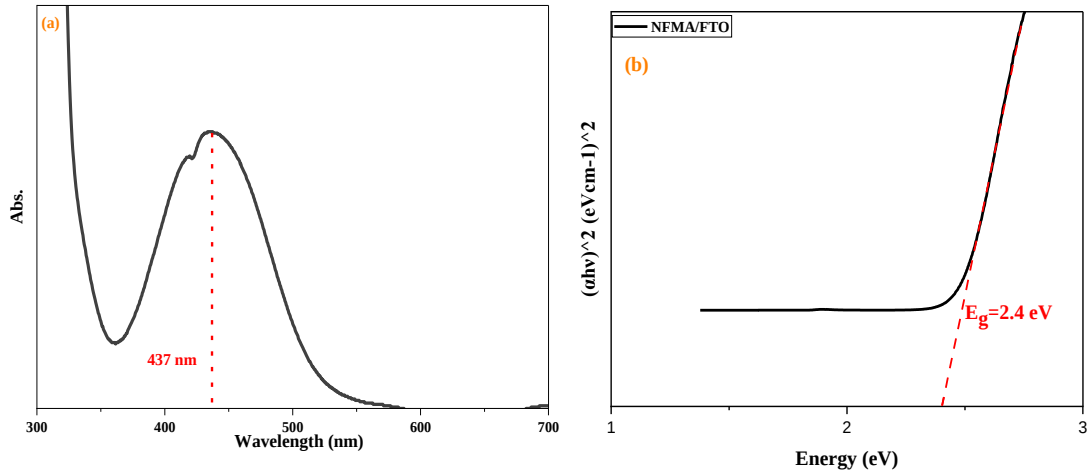

Figure 3.14. (a) The UV-visible absorption spectrum of the NFMA solution, and **(b)** the αhv *vs* Energy

2.2.6. Electrochemical Analysis

The NFMA composite underwent X-ray diffraction (XRD) analysis. The electrochemical studies were performed at room temperature using a solution composed of 12 mL of 0.01 M ($C_{17}H_{16}NFe$) in 9 mL of ethanol and 3 mL of 0.1 M H2SO4. Cyclic voltammetry (CV) measurements were conducted within a potential range of 0 to 800 mV, with a scan rate of 50 mV/s. The electron transfer behavior of the NFMA/FTO electrode redox pair was investigated using cyclic voltammetry measurements. The studies were conducted in a solution of 0.1 M H_2SO_4 containing 0.01 M NFMA, and the scan speeds ranged from 10 to 100 mV s^{-1}.

Figure 3.15a demonstrates that the redox peak currents (Ipc and Ipa) grow when the scan rate of the NFMA/FTO electrode increases. When the scan rate was set to 100

mV s^{-1}, the cathodic peak (Ipc) saw an approximate shift of 144 mV. This shift suggests that the redox process of the NFMA/FTO thin-film was not perfectly reversible, as explained by **equations 6 and 7**.

$$E = E° + (RT/nF)ln((ox)/(red)) \quad (3.6)$$

$$n = 2.303RT/((\Delta E_p)/log(k_a/k_c)) \quad (3.7)$$

E° represents the standard potential, R stands for the gas constant, T denotes the temperature, n signifies the number of electrons involved in the transfer process, and F represents the Faraday constant. Additionally, within the equation, (ox) and (red) correspond to the concentrations of the oxidized and reduced species, respectively. The terms "ka" and "kc" refer to the rate constants governing the forward and backward reactions, respectively.

The quasi-reversible process occurs at the electrode surface, as illustrated in **Figure 3.15b**, depicting the relationship between the square root of the scan rate ($\upsilon^{1/2}$) and the redox peak current values. A linear regression analysis revealed a high degree of linearity, with regression coefficients (R^2) of 0.99 for Ipa and 0.98 for Ipc. This linear relationship suggests that the peak current is directly proportional to the square root of the scan rate values, indicating that the redox process is governed by diffusion control and confirming the stability of a monolayer.

Simultaneously, cyclic voltammetry (CV) curves of NFMA/FTO in a 0.1 M H2SO4 solution were recorded. These curves demonstrated the significant role played by NFMA in enhancing the peak current. However, the CV curves obtained at different scan rates remained consistent, indicating that the FTO electrode exhibits excellent rate capability and reversibility.

When the scan rates were reduced, the NFMA ions spread out into the FTO glass, leading to increased specific capacitances. On the other hand, the reduction in specific capacitance of the FTO electrode at higher scan rates might be attributed to the restricted availability of NFMA ions to many active surface locations, as shown in **Figure 3.15**. The specific capacitance (Cs) of the NFMA/FTO electrode was determined by applying the following equation:

$$Cs = (\int_{Vi}^{V_f}(V)\,dV)/(2\ s\ m\Delta V) \quad (3.8)$$

"s" represents the discharge time, "m" denotes the mass of the active material, "mVs^{-1}" signifies the scan rate, and "V" represents the discharge potential window[173]. **Figure 3.15a** presents the cyclic voltammograms (CVs) obtained as the concentration of NFMA was systematically increased. In the forward scan, the NFMA current peaks shifted towards more positive potentials, resulting in a positive peak current (Ipa). Conversely, during the reverse scan, the CVs exhibited negative potentials and moved towards more negative values, indicating a negative peak current (Ipc). The occurrence of Ipc potentials can be attributed to the back transfer of Fc^{+} from the NFMA solution to the FTO electrode. The shape of the CVs suggests that the transfer of NFMA is quasi-reversible. The electrochemical behavior of the FTO electrode in response to various NFMA concentrations ranging from 0.001 g/mL to 0.005 g/mL is depicted in **Figure 3.15b**. Notably, the peak current (Ipa) exhibited a proportional increase with the concentration of NFMA, demonstrating a linear correlation between Ipa and NFMA concentration.

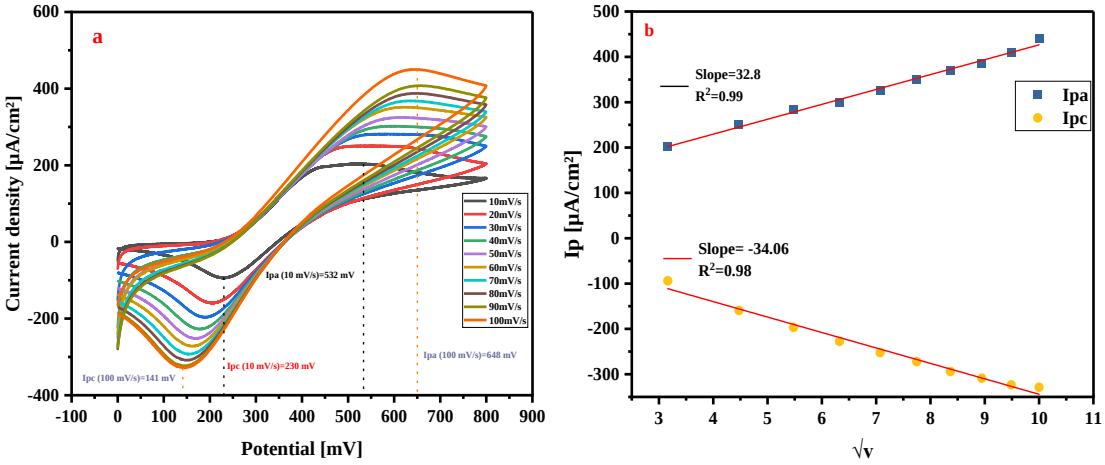

Figure 3.15. Displays the kinetics of the process taking place at the NFMA/FTO electrode. The data was obtained by cyclic voltammetry, employing scan rates varying from 10 to 100 mV s^{-1}, in a solution of 0.01 M NFMA and 0.1 M H_2SO_4. The study focused on examining the correlation between the anodic and cathodic current peaks and the square root of the scan rate.

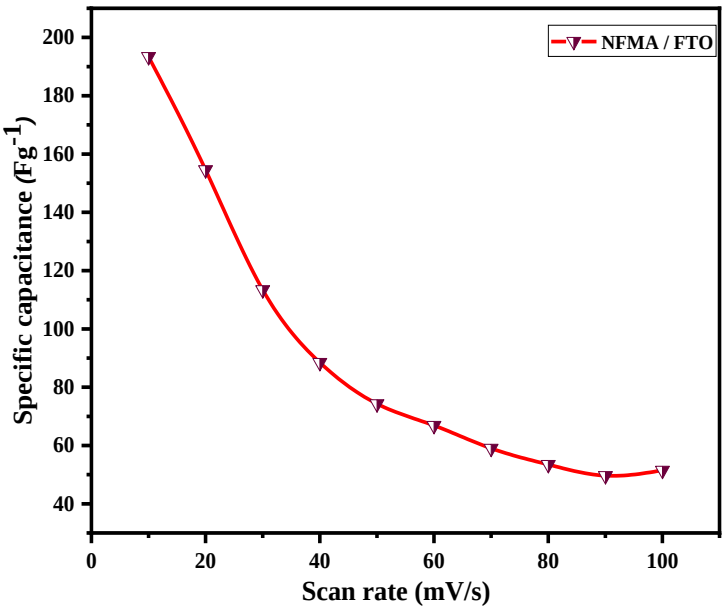

Figure 3.16. The specific capacitance values obtained at various scanning rates.

Impedance Spectroscopy analysis (IS)

Electrochemical Impedance Spectroscopy (EIS) is a widely used technique for studying the behavior of electric current when subjected to alternating current (AC) voltage at various frequencies. Electrochemical impedance spectroscopy (EIS) has been widely used to study the kinetics of electrochemical reactions and the principles of photoelectrochemical processes. It allows for the analysis of the ionic and electronic processes occurring at various interfaces in electrochemical devices[174].

The Nyquist plot for the NFMA/FTO-modified electrode is shown in **Figure 3.17**. The Nyquist figure shows that the FTO electrode had the greatest Rct value. Conversely, the value exhibited a slow decline when altered with the ECD technique and subsequently experienced a further fall with the Immersion method. More precisely, the NFMA/FTO, which was altered using chronoamperometry and Immersion, showed Rct values of 50 mS/cm² and 51 mS/cm², respectively. The methodology of the Electrochemical Impedance Spectroscopy (EIS) measurement involves the reduction of the NFMA coating in terms of electron transport on the FTO surface. Therefore, the value of Rct is highly dependent on the interaction between the NFMA film and the FTO electrode. The NFMA/FTO electrode clearly demonstrates a lower overpotential and, thus, exhibits greater potential than the FTO electrode.

Figure 3.18a depicts an FTO electrode submerged in a solution containing Na_2SO_4. The representation involves the series connection of the solution's resistance

(Rs) with the parallel combination of the surface layer's capacitance (Cd) and the charge transfer resistance (Rt).

Conversely, **Figure 3.18b** illustrates the NFMA/FTO electrode immersed in a liquid with an NFMA layer deposited using the electrochemical approach. The semicircle is defined by the resistance of the solution (Rs) that is coupled in series with a capacitor and resistance (Rt). Consequently, the semicircle represents the balance of the solution with the ferrocene derivative layer, resulting in the semicircle's appearance.

Figure 3.18c shows the NFMA/FTO electrode submerged in a liquid that contains an NFMA deposited utilizing the Immersion process. The equilibrium between the solution and the NFMA is indicated by the series connection of a capacitor, a resistor, and the resistance of the solution (Rs). In addition, the second semicircle symbolizes a capacitor and resistor, which signifies the balance between the NFMA and FTO electrode. **Figure 3.18** demonstrates that the NFMA shows minimal activity when applied using the Immersion approach, resulting in the formation of two semicircles. In the Immersion method's equivalent circuit, Rct_2 represents the resistance of the porous layer. This resistance is mainly determined by the faulty deposition structure of the NFMA film on the FTO electrode, as depicted in **Figure 3.18c**.

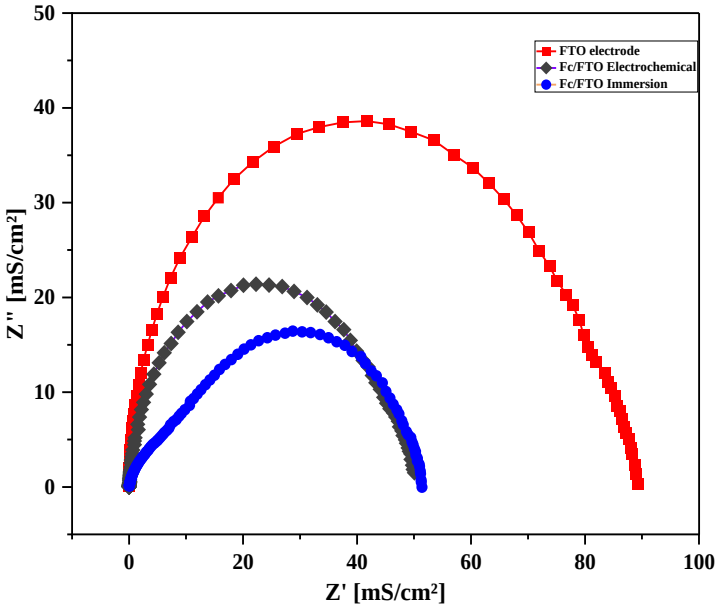

Figure 3.17. The electrochemical impedance characteristics of FTO in three conditions: FTO without any deposited film, FTO with film deposited via the electrochemical technique, and FTO with film deposited via the immersion method.

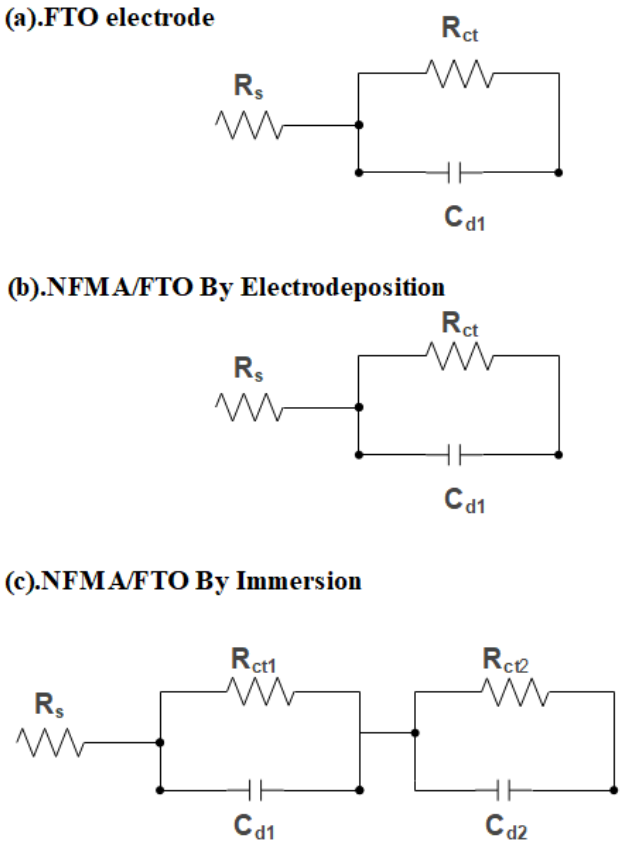

Figure 3.18: The equivalent circuit diagrams for non-faradaic processes in the following: (a) FTO electrode, (b) NFMA/FTO electrode prepared through electrodeposition, and (c) NFMA/FTO electrode prepared through the immersion technique.

Electrochemical Detection of H_2O_2

NFMA was successfully deposited onto FTO glass to create a NFMA/FTO thin-film, incorporating multiple redox centers from ferrocene derivatives into the FTO surface. This configuration was explored for its potential in electrochemically sensing H_2O_2. Consequently, the NFMA/FTO electrode was investigated for its electrochemical response to H_2O_2. **Figure 3.19a** displays the voltammograms of the fabricated NFMA/FTO electrode in a 0.1 M Na_2SO_4 solution containing only Na_2SO_4, and H_2O_2 ranging from 20 to 100 µL.

The observed phenomenon clearly demonstrates a significant increase in both oxidation and reduction current peaks immediately upon the introduction of H_2O_2[175]. The voltammogram features clearly demonstrate a highly responsive and immediate reaction of the NFMA/FTO electrode when H_2O_2 is introduced. In the voltage range of 0–800 mV, an anodic peak (Ipa) is observed during the forward scan, with a potential of 408 mV for 20 µL, which corresponds to the oxidation of the

ferrocene complex (Fc to Fc^+). Conversely, in the backward scan, a cathodic peak is observed at 244 mV for 20 µL, corresponding to the reduction of the ferrocene cation (Fc^+ to Fc). This voltammogram is a result of the presence of electroactive NFMA nuclei on the FTO surface.

In the presence of H_2O_2, the potential of the Ipa and Ipc peaks is shifted, and there is an increase in the current density[176]. This alteration in cyclic voltammograms (CVs) indicates a simplification of the Ipa and Ipc processes. The observed change in current can be attributed to the oxidation of H_2O_2 to O_2 and the regeneration of H_2O_2 to H_2O in the presence of Fc/Fc^+ (as depicted in **Figure 3.19b**.

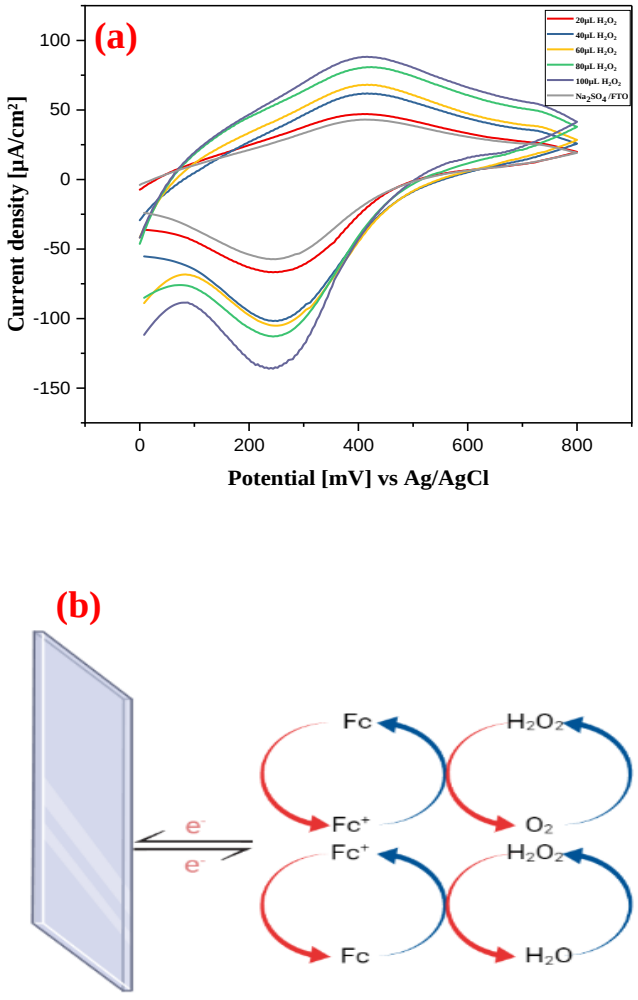

Figure 3.19. (a) Cyclic voltammograms (CVs) recorded from the produced NFMA /FTO thin-film electrode in a solution containing only Na_2SO_4 and varying volumes of H_2O_2 (ranging from 20 to 100 µL). The scan rate employed was 400 mV/s, and 0.1M Na_2SO_4 served as the supporting electrolyte. (b) A suggested electrochemical reaction mechanism outlining the interactions between NFMA/FTO and H_2O_2.

Photocatalytic degradation of Methylene Blue

Under sunlight exposure, the photocatalytic performance of the NFMA/FTO thin film was evaluated by assessing the degradation of MB at a concentration of 1 PPM in a 500 mL aqueous solution. The remarkable photocatalytic efficiency of the NFMA/FTO thin film (as depicted in **Figure 3.20**) is attributed to its band-gap value of 2.4 eV, which can facilitate the recombination of electron-hole pairs. **Figure 3.20a** demonstrates the progression of MB degradation over the irradiation period of NFMA/FTO, while **Figure 3.20b** illustrates the degradation of MB under sunlight using the NFMA/FTO electrode, reaching a degradation rate of 78% after 180 minutes. In **Figure 3.20c**, the advancement of MB degradation is presented in terms of the ratio oxidation process, $-Ln(C/C_0)$, over the course of the investigation. It is important to note that various environmental factors, including wind speed, humidity, solar radiation levels, and temperature, can influence the photocatalytic process. **Table 3.2** below provides a detailed overview of the variations in these factors over 30-minute intervals from 11 a.m. to 3 p.m.

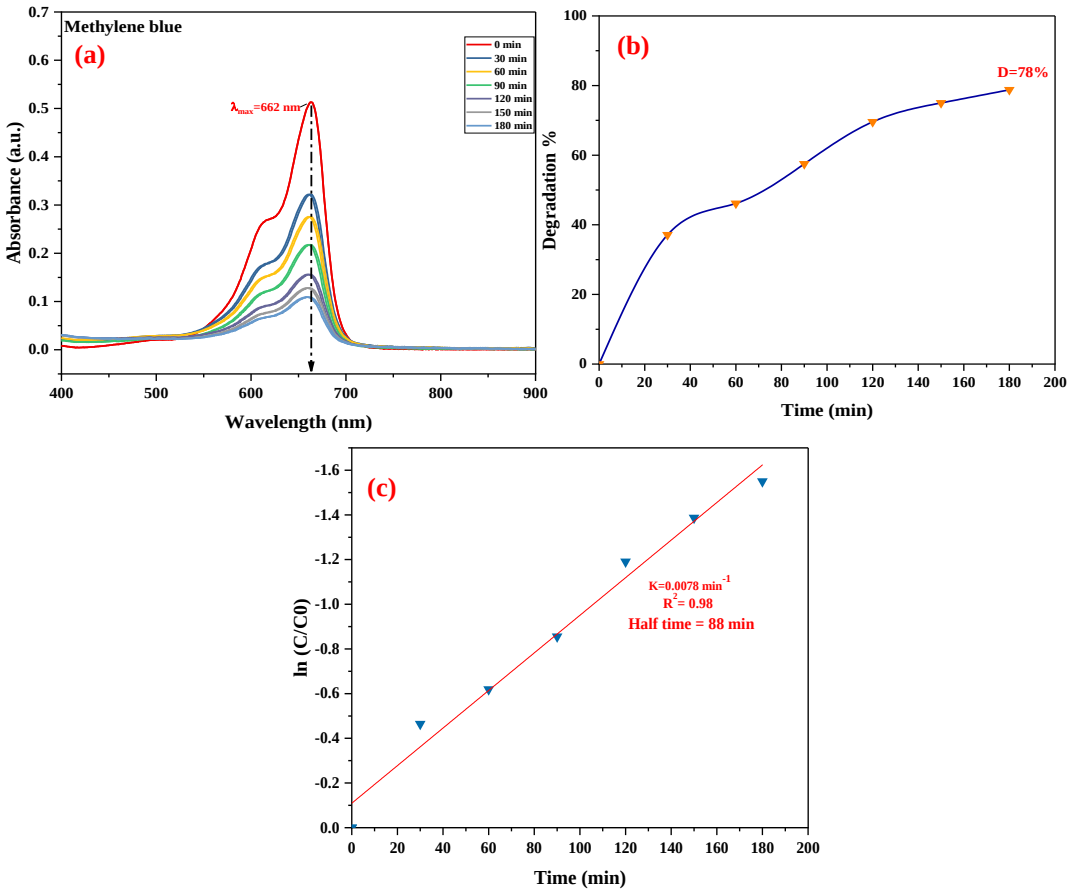

Figure 3.20. UV-Visible absorption spectra of (a) MB exposed to sunlight, (b) dye degradation, and (c) kinetic plot following pseudo-first-order reaction.

Table 3.2 Variations in parameters and radiation every 30 minutes during the photocatalytic degradation of MB on February 1st, 2023, in Eloued, Algeria.

Time (min)	**0**	**15**	**30**	**45**	**60**	**90**	**120**
Wind speed (km/h)	5	5	5	5	5	5	5
Temperature (C^0)	14	14	14	14	15	15	16
Humidity (%)	33	33	33	33	33	33	33
Radiation	low	moderate					

In order to examine the elements contributing to the improvement of the photocatalytic response for MB, we have presented a proposed energy band diagram and a mechanism for charge transport in NFMA/FTO in **Scheme 2**. The photocatalytic reaction initiates with the absorption of photons by the catalyst, which carries energy levels exceeding the bandgap energy[177]. Consequently, this leads to the rapid elevation of excited electrons from the valence band (VB) to the conduction band (CB)[178].

This, in turn, triggers an oxygen reduction reaction. Simultaneously, the vacancies left behind in the valence band (VB) can serve as oxidizing agents, facilitating oxidation reactions. The photocatalytic attributes of NFMA films in the presence of MB solution can be described using the following equations[179]:

$$NFMA \xrightarrow{h\nu\ (\text{(solar irradiation)})} NFMA\left(e^{-}/_{h^{+}}\right) \rightarrow NFMA\,({e_{cb}}^{-}) + NFMA({h_{vb}}^{+}) \quad (3.9)$$

Following that, the generation of ${O_2}^{\bullet -}$ and $2OH^{\bullet}$ is stated as follows:

$$NFMA({e_{cb}}^{-}) + {O^{\bullet}}_2 \rightarrow {O_2}^{\bullet -} \quad (3.10)$$

$${O^{\bullet}}_2 + H_2O \rightarrow 2OH^{\bullet} \quad (3.11)$$

The hydroxyl radicals, once liberated, exclusively convey unbound electrons, whereas the superoxide anion radicals carry an extra negative charge. Given the contrasting chemical characteristics of these two types of radicals, it is reasonable to suggest that the degradation process, instigated by these radicals, would be driven primarily by the formation of hydroxylated radicals, while keeping the concentration

of ions in the solution at a minimum level[35]. Then the NFMA photocatalysis process continues as follows:

$$NFMA(h_{vb}{}^{+}) + H_2O \rightarrow OH^{\bullet} + H^{+} \quad (3.12)$$

$$H^{+} + H_2O^{\bullet} + O^{\bullet}{}_2 \rightarrow OH^{\bullet} + OH^{-} + H_2O_2 \quad (3.13)$$

$$NFMA(e_{cb}{}^{-}) + H_2O_2 \rightarrow OH^{\bullet} + OH^{-} \quad (3.14)$$

$$NFMA(h_{vb}{}^{+}) + OH^{-} \rightarrow OH^{\bullet} \quad (3.15)$$

Furthermore, owing to the inherent negative charge carried by anions, their interactions are anticipated to result in significant mineralization, with limited production of hydroxylated radicals and a possible presence of inorganic ions, contingent upon their presence within the organic structure[180]. Following the photocatalytic process, when superoxide anions ($O^{\bullet}{}_2$) and hydroxyl radicals ($OH^{\bullet}$) are produced, they engage in reactions with organic molecules (such as Methylene Blue) as outlined below:

$$OH^{\bullet} + MB \rightarrow H_2O + CO_2 \quad (3.16)$$

The photo-generated electrons transform dissolved oxygen into superoxide radicals $O^{\bullet}{}_2$which subsequently initiate the degradation of MB. Concurrently, the empty sites in the valence band (VB) promote the oxidation of water by generating hydroxyl radicals($OH^{\bullet}$). This process extends the lifetime of charge carriers and impedes their recombination[181]. The kinetics of MB photodegradation is commonly described using the first-order concept, as outlined in **Equation 17**. The integration of this equation yields the following result:

$$ln(C_0/C_t) = K_{app}.t \quad (3.17)$$

The time-dependent changes in -Ln(C_t/C_0) exhibit linearity regardless of the initial concentration, thereby confirming the applicability of first-order kinetics. In accordance with the Langmuir-Hinshelwood hypothesis, the photocatalysis yields an unsteady Kapp value of 0.0078 min^{-1}. The coefficient of determination (R^2) approaches approximately 0.98, signifying a stable value according to the Langmuir-Hinshelwood hypothesis. It is possible to calculate the half-time ($t_{1/2}$) using the K_{app} parameters:

$$t_{1/2} = (ln2/k_{app}) \quad (3.18)$$

This suggests that the initial degradation rate increases with the initial concentration (C_0), as evidenced by the $t_{1/2}$ and K_{app} values. Improving the interaction between MB and the NFMA film with photogenerated molecules enhances the overall photocatalytic efficiency.

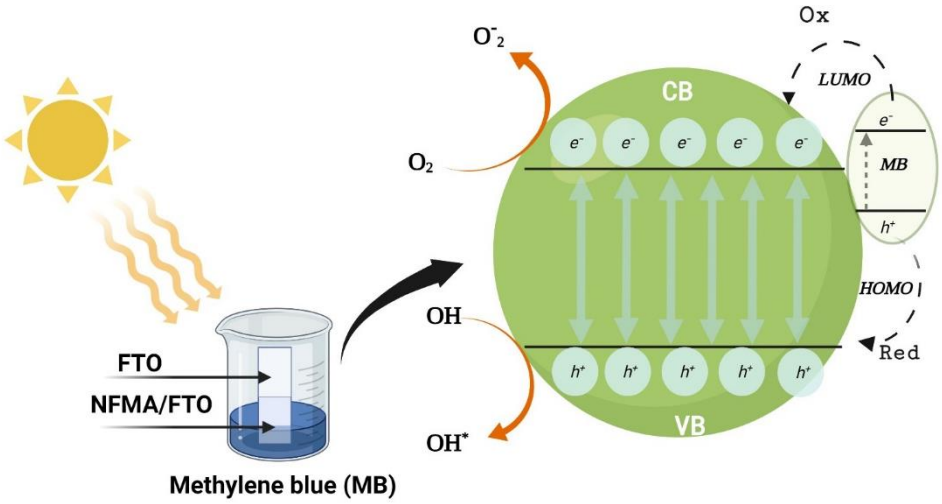

Scheme 2 Photocatalytic Mechanism of NFMA/FTO Electrode for the Degradation of Methylene Blue

2.2.7. Conclusion

This study involved doing a thorough analysis of the electrochemical and physicochemical properties to effectively create a new NFMA/FTO electrochemical thin film. The thin film was used as a highly effective electrochemical sensor for H_2O_2 and exhibited remarkable efficiency in breaking down low levels of MB in water when exposed to sunshine. The findings derived from cyclic voltammetry, chronoamperometry, and electrochemical impedance spectroscopy (EIS) verified that the NFMA/FTO film exhibited enhanced electrochemical stability and homogeneity in comparison to the immersion approach. The increased stability and homogeneity of NFMA/FTO electrodes make them very appropriate for many applications.

The X-ray diffraction (XRD) examination demonstrated a change in the structure of NFMA on the FTO electrode, shifting from a polycrystalline to a monocrystalline state, depending on the method of deposition. The surface roughness measurements (R_q) for the films were found to be 68 nm for electrodeposition and 110

nm for the immersion approach. These results indicate that the immersion technique leads to higher surface roughness and greater heterogeneity. Furthermore, the measurements of water droplet angles clearly indicated that the NFMA/FTO surface is hydrophobic, which suggests that it has great potential for use in hydrophobic applications.

Moreover, the NFMA/FTO thin film had a narrow bandgap of around 2.4 eV, indicating its appropriateness for optoelectronic devices. The NFMA/FTO electrode exhibited a significant degradation rate of 78% in the MB degradation experiment, which followed first-order kinetics. In addition, the NFMA/FTO electrode efficiently detected H_2O_2 and enabled its conversion to O_2 by oxidation, as well as reduction to H_2O.

The combined results highlight the significant potential of the NFMA/FTO thin film for a wide range of applications, including environmental remediation and optoelectronics. This is due to its exceptional electrochemical capabilities, surface features, and optical functioning.

2.3.NFMA/Cu_2O Deposited on ITO Thin Film By Electrodeposition and Immersion Techniques

2.3.1. UV-Visible Spectroscopy

The UV-visible absorption spectrum analysis conducted on NFMA/Cu_2O/ITO offers valuable insights into its optical properties and potential applications, particularly in the realm of photovoltaics. By examining the direct band gap (Eg) values, which indicate the energy required to excite electrons from the valence band to the conduction band (**Figure 3.21)**.

The measured Eg value of 2.08 eV for NFMA/Cu_2O/ITO suggests that it possesses the necessary electronic structure to function effectively as a semiconductor. Semiconductors are pivotal in photovoltaic devices as they can absorb light energy and generate electricity through the photovoltaic effect. Moreover, the Eg value falling within this range indicates that NFMA/Cu_2O/ITO holds promise as a highly efficient material for such applications. the UV-visible absorption spectrum analysis provides compelling evidence of NFMA/Cu_2O/ITO 's semiconductor nature and its suitability for use in photovoltaic technologies.

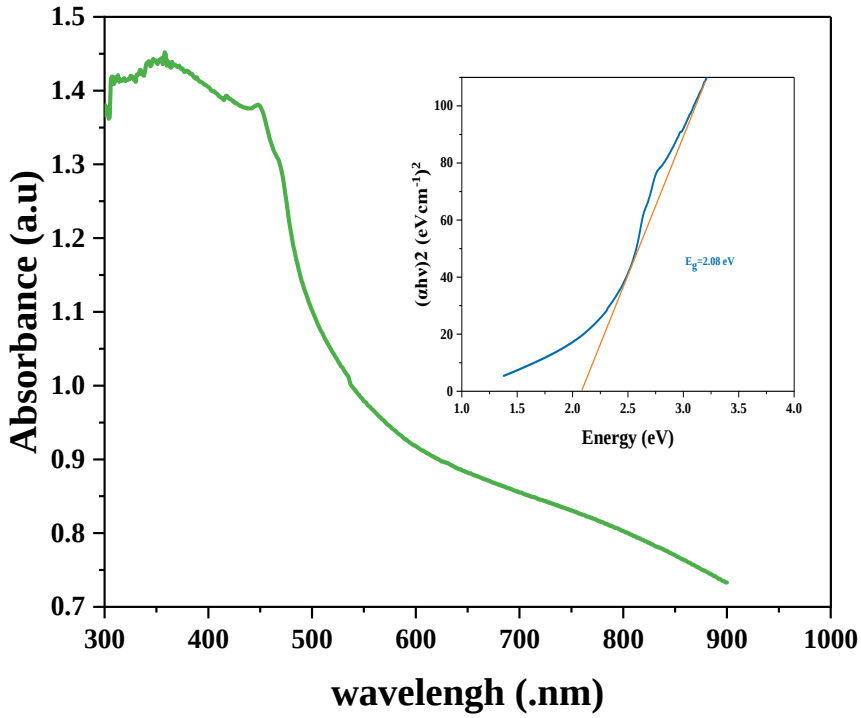

Figure 3.21. Depicts the UV-Vis spectra and energy band gaps of NFMA/Cu_2O/ITO.

2.3.2. XRD analysis of NFMA/Cu_2O/ITO

The X-ray diffraction (XRD) analyses conducted on NFMA/Cu_2O/ITO samples, prepared through a combination of electrodeposition for Cu_2O and an immersion technique for NFMA, offer valuable insights into the structural characteristics of the materials involved. The distinct peaks observed in the XRD pattern, particularly at 2θ = 17.12° and 22.90° as shown in **Figure 3.22**, signify the polycrystalline nature and enhanced crystallinity of NFMA within the electrode. Comparison with the JCPDS reference code 029-1711 further elucidates the molecular crystal structure of ferrocene, providing standard monoclinic unit cell parameters. Notably, the presence of ferrocene peaks at relatively low angles (2Θ ~ 10−30°) in the XRD pattern suggests potential organic molecular crystal transformations, possibly induced by moderate temperature-driven crystalline amorphization and structural phase transitions.

Moreover, the XRD profile of the electrode fabricated via electrodeposition displays prominent peaks at 2θ = 29°, 36°, and 61°, corresponding to (110) and (111) reflections of Cu_2O (JCPDS: 05-0667). This observation underscores the high crystalline quality achieved on the modified ITO electrode surface. The presence of well-defined peaks indicates a robust crystalline structure, essential for various applications in electrochemical devices and sensors. Additionally, the determination

of the grain size using the Scherrer equation yields an average size of approximately 55 nm, providing valuable information about the microstructural features of the electrode material. the XRD analyses offer comprehensive insights into the structural characteristics and crystalline integrity of the NFMA/Cu_2O/ITO samples. Understanding these aspects is crucial for optimizing the fabrication process and tailoring the material properties to meet specific application requirements, particularly in the fields of electrochemistry and nanotechnology.

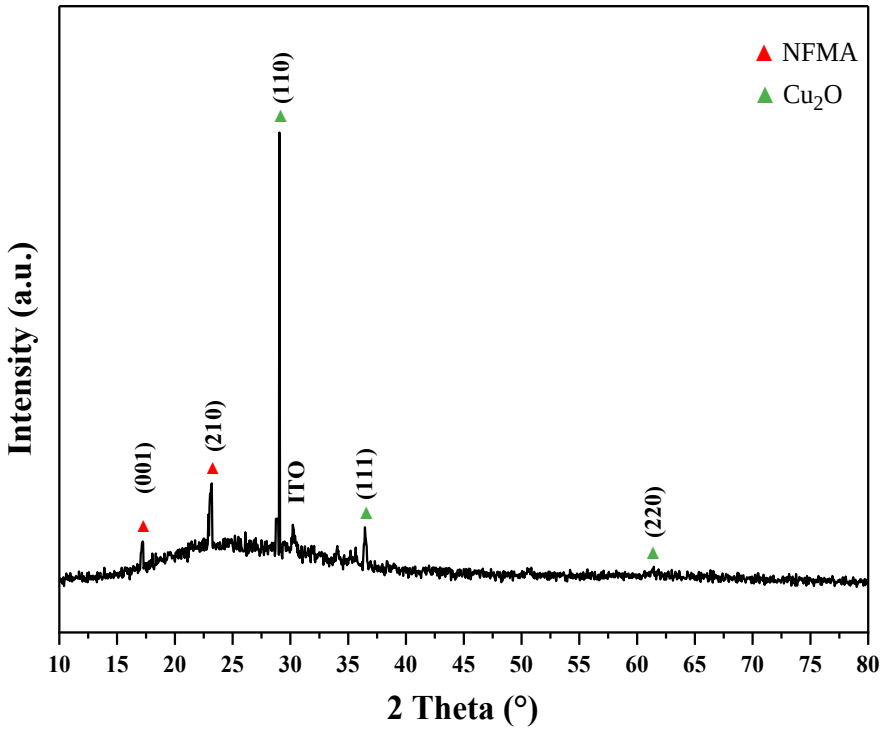

Figure 3.22. X-ray diffraction (XRD) profiles obtained from the NFMA/Cu_2O/ITO electrode.

2.3.3. Morphological analysis

SEM analysis serves as a vital tool for exploring the intricate morphology of NFMA/Cu_2O/ITO electrodes, shedding light on the structural characteristics essential for their functional properties. The SEM images depicted in **Figure 3.23.** offer valuable insights into the distinct particle shapes observed within the electrode configuration.

Notably, the cubic morphology of Cu_2O particles signifies the formation of a uniform thin film, crucial for ensuring consistent electrical conductivity and stability. In contrast, the deposition process of NFMA particles onto the ITO electrode unfolds in two distinct phases, as elucidated by the SEM observations. Initially, NFMA

material uniformly coats the modified ITO electrode at ambient temperature, creating a homogeneous film. Subsequent temperature elevation prompts the gradual growth of nuclei, leading to the formation of particles with an average size of approximately 43 nm, as corroborated by XRD analysis. This nuanced understanding of the NFMA film morphology is paramount, as it profoundly influences charge transport mechanisms within the NFMA/Cu_2O/ITO structure.

By elucidating the intricate interplay between morphology and functionality, SEM analysis facilitates the optimization of electrode design and performance in various electrochemical applications, thereby advancing the development of efficient energy storage and conversion devices.

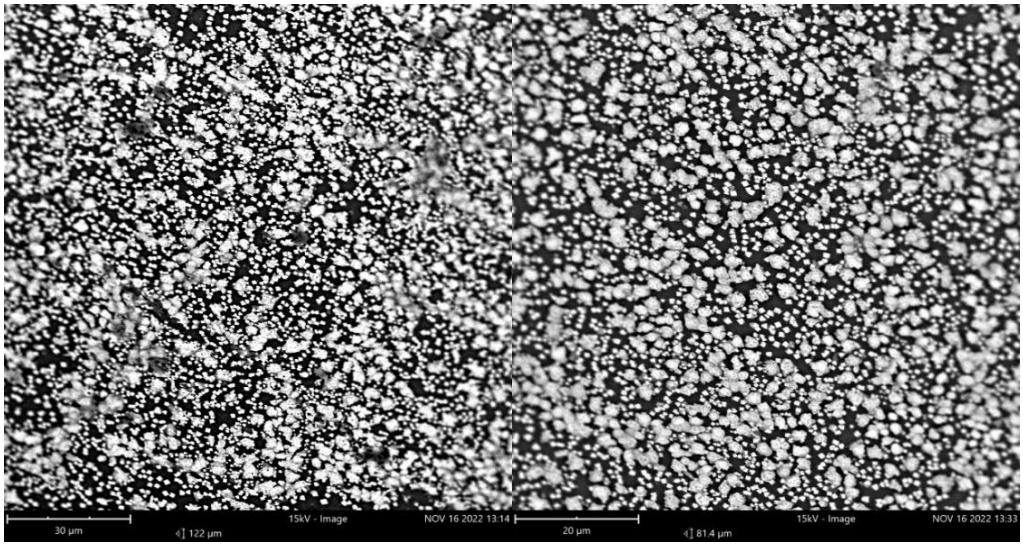

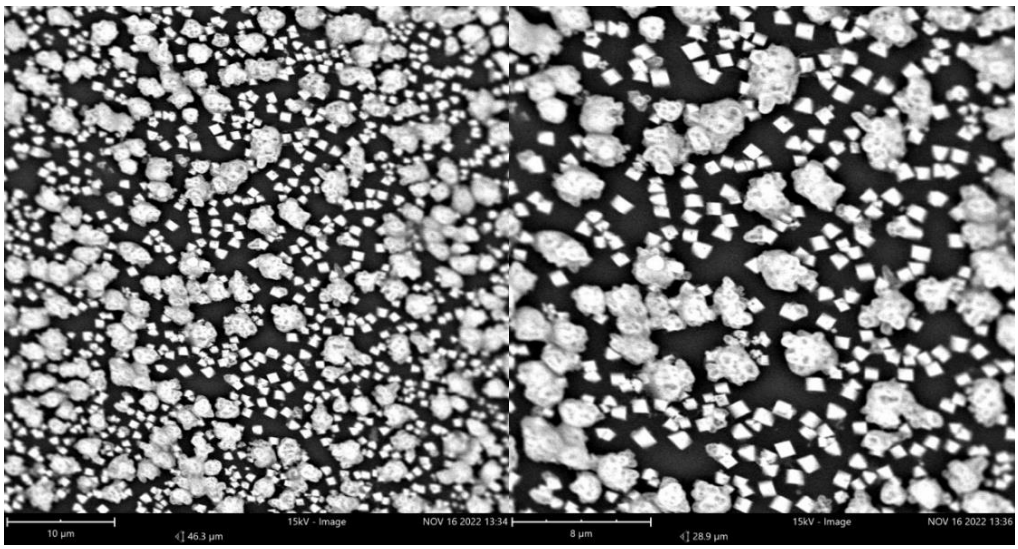

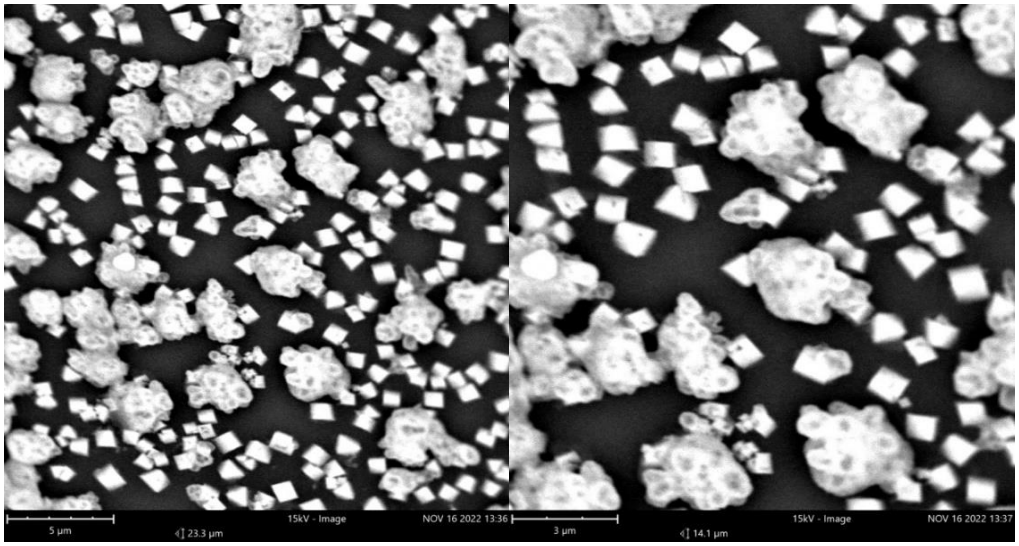

Figure 3.23. SEM image of NFMA/Cu_2O/ITO electrode.

2.3.4. Photocatalytic activity and its mechanism

The enhanced photocatalytic performance observed in the NFMA/Cu_2O/ITO thin film, particularly in its ability to degrade RB under sunlight exposure, is primarily attributed to its optimal band-gap energy of 2.08 eV, facilitating efficient electron-hole pair recombination. This mechanism, fundamental to photocatalysis, involves the absorption of photons by the catalyst, which promotes the excitation of electrons from the valence band to the conduction band while creating holes in the valence band. These excited electrons and holes subsequently participate in reduction and oxidation reactions, respectively, driving the degradation of RB molecules.

The specific equations describing the degradation process, along with the proposed energy band diagram and charge transport mechanism presented in **Schema 2**, provide valuable insights into the underlying processes governing the photocatalytic activity of NFMA/Cu_2O/ITO. It's noteworthy that environmental parameters such as wind speed, humidity, solar radiation intensity, and temperature can significantly influence the photocatalytic efficiency. The substantial degradation rate of RB achieved by NFMA/Cu_2O/ITO, reaching 80% at 542 nm as depicted in **Figure 3.24 (a,b)**, underscores its efficacy as a photocatalyst for organic dye degradation. This exceptional performance highlights the promising potential of NFMA/Cu_2O/ITO in various environmental remediation applications, emphasizing its role as a highly effective and sustainable photocatalytic material.

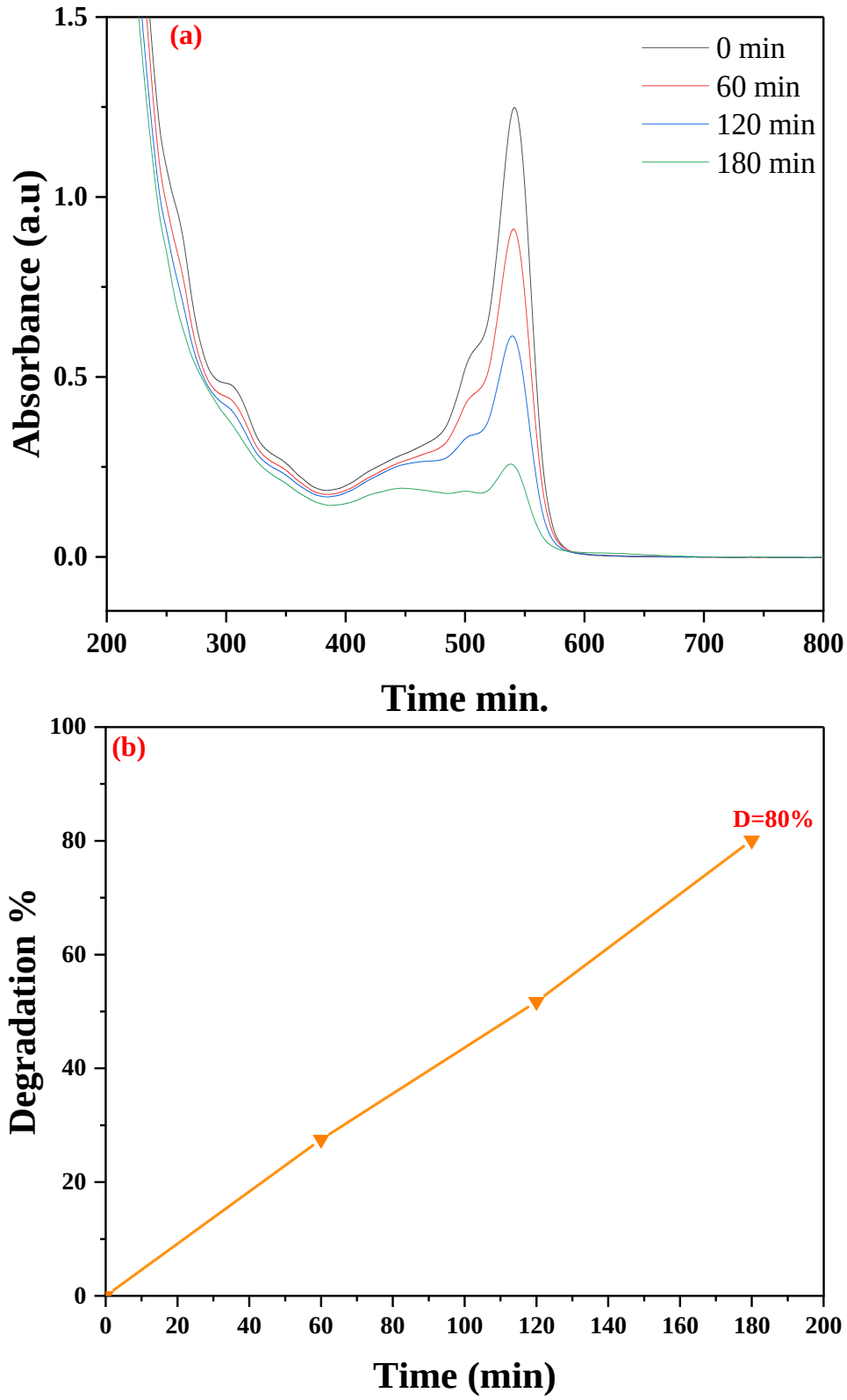

Figure 3.24. The UV-Visible spectra depict (a) the absorption characteristics of dyes after exposure to RB for up to 180 minutes, and (b) Plot of the degradation of RB over time.

The release of hydroxyl radicals involves the transportation of sole free electrons, whereas superoxide anion radicals carry an additional negative charge. Due

to their distinct chemical properties, it is plausible to propose that the degradation process initiated by radicals progresses through the generation of hydroxylated radicals while maintaining a low ion population in the solution. The NFMA/Cu_2O/ITO photocatalytic process operates through several sequential reactions, as outlined below:

$$NFMA/Cu_2O(e_{cb}^{-}) + O^{\bullet}{}_2 \rightarrow O_2^{\bullet -} \quad (3.19)$$

$$O^{\bullet}{}_2 + H_2O \rightarrow 2OH^{\bullet} \quad (3.20)$$

$$NFMA/Cu_2O(h_{vb}^{+}) + H_2O \rightarrow OH^{\bullet} + H^{+} \quad (3.21)$$

$$H^{+} + H_2O^{\bullet} + O^{\bullet}{}_2 \rightarrow OH^{\bullet} + OH^{-} + H_2O_2 \quad (3.22)$$

$$FMA/Cu_2O(e_{cb}^{-}) + H_2O_2 \rightarrow OH^{\bullet} + OH^{-} \quad (3.23)$$

$$FMA/Cu_2O(h_{vb}^{+}) + OH^{-} \rightarrow OH^{\bullet} \quad (3.24)$$

Moreover, due to the inherent charge of anions, their interactions are expected to lead to substantial mineralization, with limited hydroxylated radical production and the possibility of inorganic ion presence within the organic structure. Post-photocatalytic process, the generated superoxide anion ($O^{\bullet}{}_2$) and hydroxyl radicals ($OH^{\bullet}$) interact with molecules (RB) as follows:

$$OH^{\bullet} + RB \rightarrow H_2O + CO_2 \quad (3.25)$$

Electrons generated through photolysis of dissolved oxygen produce hydroxyl radicals ($OH^{\bullet}$) initiating RB molecule degradation. Simultaneously, vacancies in the valence band (VB) promote water oxidation, generating hydroxyl radicals (OH•), thus prolonging carrier lifetimes and impeding recombination. The kinetics of RB photodegradation are comprehensively elucidated using the first-order concept (Eq. 17). Plots of ln(C_0/Ct) versus time display linear trends irrespective of initial concentration, validating first-order kinetics (**Scheme 3**). According to the Langmuir-Hinshelwood hypothesis, the photocatalysis demonstrates an unstable Kapp value of -0.00875 min^{-1}. The regression coefficient, R^2, approaches ~0.94, suggesting a stable value consistent with the Langmuir-Hinshelwood hypothesis.

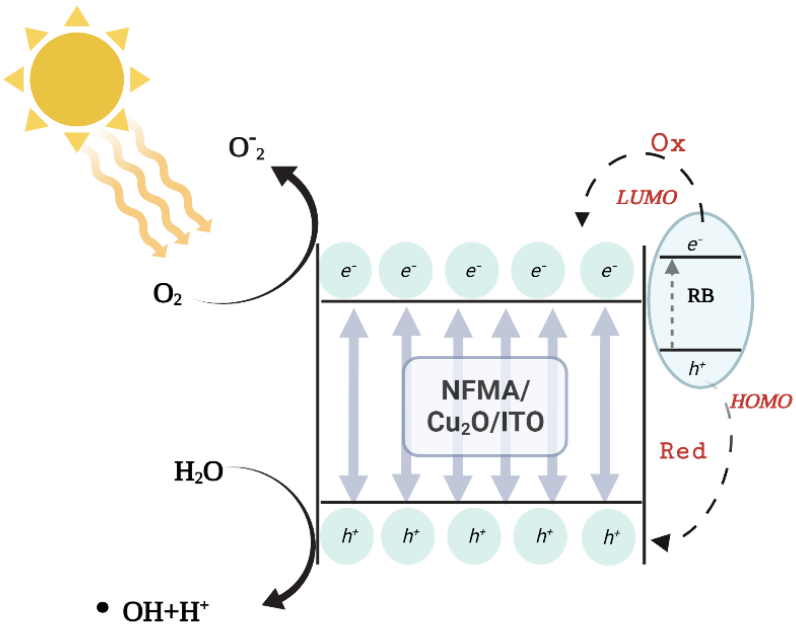

Scheme 3 Possible photocatalytic Mechanism of NFMA/Cu_2O/ITO Electrode for the Degradation of Rose Bangel.

2.3.5. Conclusion

In this study, a detailed analysis was performed to develop a novel NFMA/Cu_2O/ITO thin film. This film exhibited notable effectiveness in breaking down modest levels of RB in water when exposed to sunshine. The X-ray diffraction (XRD) study showed that the NFMA had a polycrystalline structure on the Cu_2O/ITO electrode. Additionally, the NFMA/Cu_2O/ITO thin film demonstrated a narrow bandgap of around 2.08 eV, indicating its promising suitability for optoelectronic uses. The RB degradation experiment demonstrated a significant degradation rate of 80% when using the NFMA/Cu_2O/ITO electrode, following first-order kinetics. The results highlight the potential of the NFMA/Cu_2O/ITO thin film for many applications, such as environmental remediation and optoelectronics, because of its excellent electrochemical properties, surface features, and optical functioning.

Conclusion General

Conclusion General

The dissertation focused on optimizing conditions for producing modified ITO/FTO glass, semiconductor, and ferrocene derivative electrodes, emphasizing synthesis, characterization, and applications. It successfully demonstrated the deposition and characterization of AgNPs/ITO, NFMA/FTO, and NFMA/Cu_2O/ITO thin films, each with unique properties and promising applications.

Ag/ITO-coated glass, and cyclic voltammetry revealed that lower scan rates increased nanoparticle deposition. The Ag/ITO films displayed crystalline structures with preferred orientation, homogeneous surface morphology, and high transmittance, indicating potential for enhancing photovoltaic technologies through improved structural and electrical properties.

The NFMA/FTO thin film showed improved stability and homogeneity compared to immersion-prepared films, with XRD revealing a shift from polycrystalline to monocrystalline structures and lower surface roughness. Its hydrophobicity, influenced by the electrodeposition method, enabled a 78% degradation rate of methylene blue under sunlight, underscoring its suitability for wastewater treatment and photocatalysis. The low bandgap of 2.4 eV also makes it a strong candidate for optoelectronic applications.

The NFMA/Cu_2O/ITO thin film achieved an 80% degradation of rose Bengal under sunlight, with XRD confirming its polycrystalline structure and a low bandgap of 2.08 eV, highlighting its potential for photocatalysis and environmental remediation. These findings emphasize the link between electrical properties, structural characteristics, and performance in electrochemical applications, suggesting that nanoscale modifications can significantly enhance functionality.

These results also pave the way for advancing photovoltaic cells and sensors. Future research could explore strategies like doping or hybrid structures to achieve even lower bandgaps, better hydrophobicity, and improved photocatalytic efficiency, broadening the scope of these materials in energy and environmental technologies.

Reference

Reference

1. Kyomuhimbo, H., et al., *Electroconductive Polyaniline–Ag-ZnO Green Nanocomposite Material. Processes 2022, 10, 457*. 2022, s Note: MDPI stays neutral with regard to jurisdictional claims in published ….
2. Granqvist, C.G., *Transparent conductors as solar energy materials: A panoramic review.* Solar energy materials and solar cells, 2007. **91**(17): p. 1529-1598.
3. Subramanyam, T., et al., *Optimization of sputtered AZO thin films for device application.* Materials Today: Proceedings, 2018. **5**(4): p. 10851-10859.
4. Aouaj, M.A., et al., *Comparative study of ITO and FTO thin films grown by spray pyrolysis.* Materials Research Bulletin, 2009. **44**(7): p. 1458-1461.
5. Kim, T.-H., et al., *Roll-to-roll sputtered ITO/Ag/ITO multilayers for highly transparent and flexible electrochromic applications.* Solar Energy Materials and Solar Cells, 2017. **160**: p. 203-210.
6. Park, Y.-S., K.-H. Choi, and H.-K. Kim, *Room temperature flexible and transparent ITO/Ag/ITO electrode grown on flexile PES substrate by continuous roll-to-roll sputtering for flexible organic photovoltaics.* Journal of Physics D: Applied Physics, 2009. **42**(23): p. 235109.
7. Kim, J.-I., et al., *Ti-doped indium tin oxide thin films for transparent field-effect transistors: Control of charge-carrier density and crystalline structure.* ACS applied materials & interfaces, 2011. **3**(7): p. 2522-2528.
8. Scroccarello, A., et al., *Plasmonic active film integrating gold/silver nanostructures for H2O2 readout.* Talanta, 2021. **222**: p. 121682.
9. Zawadzki, M., *Synthesis of nanosized and microporous zinc aluminate spinel by microwave assisted hydrothermal method (microwave–hydrothermal synthesis of ZnAl2O4).* Solid State Sciences, 2006. **8**(1): p. 14-18.
10. Thirumoorthi, M. and J.T.J. Prakash, *Structural, morphological characteristics and optical properties of Y doped ZnO thin films by sol–gel spin coating method.* Superlattices and Microstructures, 2015. **85**: p. 237-247.
11. Xia, G., Q. Zhang, and S. Wang, *High-mobility IGZO TFTs by infrared radiation activated low-temperature solution process.* IEEE Electron Device Letters, 2018. **39**(12): p. 1868-1871.
12. Lewis, E.A., C.M. Stafford, and B.D. Vogt, *Effect of adjacent hydrophilic polymer thin films on physical aging and residual stress in thin films of poly (butylnorbornene-ran-hydroxyhexafluoroisopropyl norbornene).* Journal of Polymer Science Part B: Polymer Physics, 2019. **57**(15): p. 992-1000.
13. Chopra, I., *The increasing use of silver-based products as antimicrobial agents: a useful development or a cause for concern?* Journal of antimicrobial Chemotherapy, 2007. **59**(4): p. 587-590.
14. Martínez-Castañon, G.-A., et al., *Synthesis and antibacterial activity of silver nanoparticles with different sizes.* Journal of nanoparticle research, 2008. **10**: p. 1343-1348.
15. Yang, Y., et al., *Progress in developing metal oxide nanomaterials for photoelectrochemical water splitting.* Advanced Energy Materials, 2017. **7**(19): p. 1700555.

16. Chandrasekaran, S., et al., *Recent advances in metal sulfides: from controlled fabrication to electrocatalytic, photocatalytic and photoelectrochemical water splitting and beyond.* Chemical Society Reviews, 2019. **48**(15): p. 4178-4280.
17. Luo, Z., T. Wang, and J. Gong, *Single-crystal silicon-based electrodes for unbiased solar water splitting: current status and prospects.* Chemical Society Reviews, 2019. **48**(7): p. 2158-2181.
18. Jiang, C., et al., *Photoelectrochemical devices for solar water splitting–materials and challenges.* Chemical Society Reviews, 2017. **46**(15): p. 4645-4660.
19. Serpone, N., et al., *Why do hydrogen and oxygen yields from semiconductor-based photocatalyzed water splitting remain disappointingly low? Intrinsic and extrinsic factors impacting surface redox reactions.* ACS Energy Letters, 2016. **1**(5): p. 931-948.
20. Bronstein, H., et al., *The role of chemical design in the performance of organic semiconductors.* Nature Reviews Chemistry, 2020. **4**(2): p. 66-77.
21. Khelef, A., et al., *N-Ferrocenymethyl-N-phenylpropionamide.* Acta Crystallographica Section E: Structure Reports Online, 2012. **68**(5): p. m647-m647.
22. Cho, H.-H., et al., *A semiconducting polymer bulk heterojunction photoanode for solar water oxidation.* Nature Catalysis, 2021. **4**(5): p. 431-438.
23. Braga, S.S. and A.M. Silva, *A new age for iron: antitumoral ferrocenes.* Organometallics, 2013. **32**(20): p. 5626-5639.
24. Sansook, S., et al., *Ferrocenes in medicinal chemistry; a personal perspective.* Journal of Organometallic Chemistry, 2020. **905**: p. 121017.
25. Nacer, S.N., A. Khelef, and T. Lanez, *Calculation of Diffusion Coefficients for Oxidation of ferrocene derivative synthesized at two different electrodes using Rotating Disk Electrode (RDE).* International Letters of Chemistry, Physics and Astronomy, 2013. **9**(1): p. 39-47.
26. Paul, A., et al., *Distance dependence of the charge transfer rate for peptide nucleic acid monolayers.* The Journal of Physical Chemistry B, 2010. **114**(45): p. 14140-14148.
27. Calborean, A., L. Buimaga-Iarinca, and F. Graur, *DFT charge transfer of hybrid molecular ferrocene/Si structures.* Physica Scripta, 2015. **90**(5): p. 055803.
28. Connelly, N.G. and W.E. Geiger, *Chemical redox agents for organometallic chemistry.* Chemical reviews, 1996. **96**(2): p. 877-910.
29. Vergara, M.S., et al., *Doping of molecular materials based on ferrocene and the study of their properties as organic semiconductors for their application in optoelectronic devices.* Journal of Molecular Structure, 2019. **1193**: p. 365-372.
30. Boubekri, C., et al., *Synthesis and Electrochemical Properties of N-(ferrocenylmethyl) aminobenzonitrile and N-(ferrocenylmethyl) nitroaniline Derivatives.* International Letters of Chemistry, Physics and Astronomy, 2015. **49**: p. 27--34.
31. Wong, R.A., et al., *Discerning the redox-dependent electronic and interfacial structures in electroactive self-assembled monolayers.* Journal of the American Chemical Society, 2018. **140**(42): p. 13672-13679.

32. Ortiz, M., et al., *Amperometric supramolecular genosensor self-assembled on cyclodextrin-modified surfaces.* Electrochemistry communications, 2011. **13**(6): p. 578-581.
33. Gélinas, B., D. Das, and D. Rochefort, *Air-stable, self-bleaching electrochromic device based on viologen-and ferrocene-containing triflimide redox ionic liquids.* ACS Applied Materials & Interfaces, 2017. **9**(34): p. 28726-28736.
34. Liu, K.-G., et al., *Bilateral photocatalytic mechanism of dye degradation by a designed ferrocene-functionalized cluster under natural sunlight.* Catalysis Science & Technology, 2020. **10**(3): p. 757-767.
35. Althamthami, M., et al., *Influence of hole-scavenger and different withdrawn speeds on photocatalytic activity of Co3O4 thin films under sunlight irradiation.* Ceramics International, 2022. **48**(21): p. 31570-31578.
36. Kumar, T.N., et al., *Ferrocene-functionalized polydopamine as a novel redox matrix for H 2 O 2 oxidation.* Journal of Materials Chemistry B, 2014. **2**(36): p. 6081-6088.
37. Zhou, M., et al., *Application of hydrogel prepared from ferrocene functionalized amino acid in the design of novel electrochemical immunosensing platform.* Biosensors and Bioelectronics, 2013. **49**: p. 243-248.
38. Fan, L., et al., *Ferrocene functionalized graphene: preparation, characterization and efficient electron transfer toward sensors of H 2 O 2.* Journal of Materials Chemistry, 2012. **22**(13): p. 6165-6170.
39. Dubey, R., K. Jhansirani, and S. Singh, *Investigation of solar cell performance using multilayer thin film structure (SiO2/Si3N4) and grating.* Results in Physics, 2017. **7**: p. 77-81.
40. Segets, D., *Analysis of particle size distributions of quantum dots: From theory to application.* KONA Powder and Particle Journal, 2016: p. 2016012.
41. Oliver, W.C. and G.M. Pharr, *An improved technique for determining hardness and elastic modulus using load and displacement sensing indentation experiments.* Journal of materials research, 1992. **7**(6): p. 1564-1583.
42. Greene, J.E., *Tracing the 4000 year history of organic thin films: From monolayers on liquids to multilayers on solids.* Applied physics reviews, 2015. **2**(1): p. 011101.
43. Jeon, S.O. and J.Y. Lee, *Relationship between the particle size of quantum dots and bistability of the quantum dot embedded organic memory devices.* Journal of Industrial and Engineering Chemistry, 2011. **17**(1): p. 105-108.
44. Williams, G. and G.S. Coles, *The gas-sensing potential of nanocrystalline tin dioxide produced by a laser ablation technique.* MRS Bulletin, 1999. **24**(6): p. 25-29.
45. Freund, L.B. and S. Suresh, *Thin film materials: stress, defect formation and surface evolution*. 2004: Cambridge university press.
46. Arunkumar, P., S.K. Kuanr, and K.S. Babu, *Thin film: deposition, growth aspects, and characterization.* Thin Film Structures in Energy Applications, 2015: p. 1-49.
47. Makhlouf, A., *Current and advanced coating technologies for industrial applications*, in *Nanocoatings and ultra-thin films*. 2011, Elsevier. p. 3-23.
48. Safavi, M.S., et al., *Electrodeposited hydroxyapatite-based biocoatings: Recent progress and future challenges.* Coatings, 2021. **11**(1): p. 110.

49. Hashmi, M.S.J., *Comprehensive materials processing*. 2014: Newnes.
50. Sun, L., et al., *Chemical vapour deposition.* Nature Reviews Methods Primers, 2021. **1**(1): p. 5.
51. Barbier, A., *Single and heterostructure multiferroic thin films*, in *Magnetic, Ferroelectric, and Multiferroic Metal Oxides*. 2018, Elsevier. p. 487-514.
52. Bauer, E., *Phänomenologische theorie der kristallabscheidung an oberflächen. i.* Zeitschrift für Kristallographie-Crystalline Materials, 1958. **110**(1-6): p. 372-394.
53. Venables, J. and G. Spiller, *Nucleation and growth of thin films*, in *Surface Mobilities on Solid Materials*. 1983, Springer. p. 341-404.
54. Mühlbacher, M., *High-resolution characterization of TiN diffusion barrier layers*. 2015, Linköping University Electronic Press.
55. Beer, A.C., R.K. Willardson, and T.P. Pearsall, *Materials Science and Technology: Strained-Layer Superlattices: Strained-Layer Superlattices: Materials Science and Technology*. 1991: Academic Press.
56. Figge, S., et al., *InGaN quantum dot growth in the limits of Stranski–Krastanov and spinodal decomposition.* physica status solidi (b), 2011. **248**(8): p. 1765-1776.
57. Minami, T., *Transparent conducting oxide semiconductors for transparent electrodes.* Semiconductor science and technology, 2005. **20**(4): p. S35.
58. Afre, R.A., et al., *Transparent conducting oxide films for various applications: A review.* Reviews on advanced materials science, 2018. **53**(1): p. 79-89.
59. Exarhos, G.J. and X.-D. Zhou, *Discovery-based design of transparent conducting oxide films.* Thin solid films, 2007. **515**(18): p. 7025-7052.
60. Bhachu, D., *The synthesis and characterisation of metal oxide thin films*. 2013, UCL (University College London).
61. Ginley, D.S. and C. Bright, *Transparent conducting oxides.* MRS bulletin, 2000. **25**(8): p. 15-18.
62. Goldner, R. and H. Haskal, *Indium tin oxide-coated silicon as a selective absorber.* Applied optics, 1975. **14**(10): p. 2328-2329.
63. Minami, T., *New n-type transparent conducting oxides.* MRS bulletin, 2000. **25**(8): p. 38-44.
64. Ashcroft, N.W. and N.D. Mermin, *Solid state physics*. 2022: Cengage Learning.
65. Burns, G., *High-temperature superconductivity.* 1992.
66. Schwartz, R.W., T. Schneller, and R. Waser, *Chemical solution deposition of electronic oxide films.* Comptes Rendus Chimie, 2004. **7**(5): p. 433-461.
67. Hodes, G., *Chemical solution deposition of semiconductor films*. 2002: CRC press.
68. Schneller, T., et al., *Chemical solution deposition of functional oxide thin films*. 2013: Springer.
69. Narayanan, T.S., I.-S. Park, and M.-H. Lee, *Surface modification of magnesium and its alloys for biomedical applications: opportunities and challenges.* Surface modification of magnesium and its alloys for biomedical applications, 2015: p. 29-87.
70. Xing, W., G. Yin, and J. Zhang, *Rotating electrode methods and oxygen reduction electrocatalysts*. 2014: Elsevier.

71. Navale, S., et al., *Electrochemical supercapacitor development based on electrodeposited nickel oxide film.* RSC advances, 2015. **5**(64): p. 51961-51965.
72. Lobaccaro, P., et al., *Electrodeposition of high-purity indium thin films and its application to indium phosphide solar cells.* Journal of The Electrochemical Society, 2014. **161**(14): p. D794.
73. Yadav, S., et al., *Deposition potential controlled structural and thermoelectric behavior of electrodeposited CoSb 3 thin films.* RSC advances, 2017. **7**(33): p. 20336-20344.
74. Tyagi, I., et al., *Sustainable Materials for Sensing and Remediation of Noxious Pollutants*. 2022: Elsevier.
75. Shukor, A.H., H.A. Alhattab, and I. Takano, *Electrical and optical properties of copper oxide thin films prepared by DC magnetron sputtering.* Journal of Vacuum Science & Technology B, 2020. **38**(1).
76. Ho, S.M., *Synthesis and characterization of tin oxide thin films: a review.* Der Pharma Chemica, 2016. **8**(3): p. 20-23.
77. Ho, S., *Preparation of nanocrystalline aluminum oxide thin films: a review.* Int. J. Chem. Sci, 2017. **15**: p. 115.
78. Sounder, J., et al., *ZnO thin film prepared by dip coating technique for gas sensing application.* Int. J. Res. Appl. Sci. Eng. Technol, 2017. **5**: p. 417-419.
79. Huotari, J., et al., *Pulsed laser deposition of metal oxide nanoparticles, agglomerates, and nanotrees for chemical sensors.* Procedia engineering, 2015. **120**: p. 1158-1161.
80. Ho, S. and A. Emmanuel, *A short review of recent advances in copper oxide nanostructured thin films.* Res. J. Chem. Environ, 2019. **23**: p. 138-145.
81. Suhail, M.H., I.M. Ibrahim, and G.M. Rao, *Characterization and gas sensitivity of cadmium oxide thin films prepared by thermal evaporation technique.* Int. J. Thin Film Sci. Tec, 2012. **1**(1): p. 1-8.
82. Arafat, M., et al., *Gas sensors based on one dimensional nanostructured metal-oxides: a review.* Sensors, 2012. **12**(6): p. 7207-7258.
83. Vallejos, S., et al., *Chemical vapour deposition of gas sensitive metal oxides.* Chemosensors, 2016. **4**(1): p. 4.
84. Cremers, V., R.L. Puurunen, and J. Dendooven, *Conformality in atomic layer deposition: Current status overview of analysis and modelling.* Applied Physics Reviews, 2019. **6**(2).
85. Hagen, D., M.E. Pemble, and M. Karppinen, *Atomic layer deposition of metals: Precursors and film growth.* Applied Physics Reviews, 2019. **6**(4).
86. Hauder, M., et al., *Scaling properties and electromigration resistance of sputtered Ag metallization lines.* Applied Physics Letters, 2001. **78**(6): p. 838-840.
87. Gao, L., et al., *Metalorganic chemical vapor deposition of silver thin films for future interconnects by direct liquid injection system.* Materials science in semiconductor processing, 2004. **7**(4-6): p. 331-335.
88. Amusan, A.A., et al., *Ag films grown by remote plasma enhanced atomic layer deposition on different substrates.* Journal of Vacuum Science & Technology A, 2016. **34**(1).
89. Wack, S., et al., *Two-Step approach for conformal chemical vapor-phase deposition of ultra-thin conductive silver films.* ACS applied materials & interfaces, 2020. **12**(32): p. 36329-36338.

90. Guske, J.T., et al., *Infrared surface plasmon resonance of AZO-Ag-AZO sandwich thin films.* Optics Express, 2012. **20**(21): p. 23215-23226.
91. West, G., P. Kelly, and J. Bradley, *A comparison of thin silver films grown onto zinc oxide via conventional magnetron sputtering and HiPIMS deposition.* IEEE transactions on plasma science, 2010. **38**(11): p. 3057-3061.
92. Banzai, K., S. Naka, and H. Okada, *MoO3/Ag/MoO3 anode for organic light-emitting diodes and its carrier injection property.* Japanese Journal of Applied Physics, 2015. **54**(5): p. 054101.
93. Gu, D., et al., *Ultrasmooth and thermally stable silver-based thin films with subnanometer roughness by aluminum doping.* Acs Nano, 2014. **8**(10): p. 10343-10351.
94. Huang, J., et al., *Seed-layer-free growth of ultra-thin Ag transparent conductive films imparts flexibility to polymer solar cells.* Solar Energy Materials and Solar Cells, 2018. **184**: p. 73-81.
95. Yang, Y., W. Song, and L. Ding, *Dielectric/ultrathin metal/dielectric structured transparent conducting films for flexible electronics.* Science bulletin, 2020. **65**(16): p. 1324-1326.
96. Bahlawane, N., et al., *Alcohol-Assisted CVD of Silver Using Commercially Available Precursors.* Chemical Vapor Deposition, 2007. **13**(8): p. 401-407.
97. Niskanen, A., et al., *Radical-enhanced atomic layer deposition of silver thin films using phosphine-adducted silver carboxylates.* Chemical Vapor Deposition, 2007. **13**(8): p. 408-413.
98. Kariniemi, M., et al., *Plasma-enhanced atomic layer deposition of silver thin films.* Chemistry of Materials, 2011. **23**(11): p. 2901-2907.
99. Chalker, P., et al., *Liquid injection atomic layer deposition of silver nanoparticles.* Nanotechnology, 2010. **21**(40): p. 405602.
100. Makela, M., et al., *Studies on thermal atomic layer deposition of silver thin films.* Chemistry of Materials, 2017. **29**(5): p. 2040-2045.
101. Beyene, H.D., et al., *Synthesis paradigm and applications of silver nanoparticles (AgNPs), a review.* Sustainable materials and technologies, 2017. **13**: p. 18-23.
102. Kalfagiannis, N., et al., *Plasmonic silver nanoparticles for improved organic solar cells.* Solar Energy Materials and Solar Cells, 2012. **104**: p. 165-174.
103. Fukuura, T., *Plasmons excited in a large dense silver nanoparticle layer enhance the luminescence intensity of organic light emitting diodes.* Applied Surface Science, 2015. **346**: p. 451-457.
104. Hamdi, R., et al., *Electrodeposition study of silver: Nucleation process and theoretical analysis.* Journal of Electronic Materials, 2021. **50**: p. 5507-5513.
105. Jeong, S., et al., *Electrodeposited ZnO/Cu2O heterojunction solar cells.* Electrochimica Acta, 2008. **53**(5): p. 2226-2231.
106. Musselman, K.P., et al., *Incompatible length scales in nanostructured Cu2O solar cells.* Advanced Functional Materials, 2012. **22**(10): p. 2202-2208.
107. Zhang, Q., et al., *CuO nanostructures: synthesis, characterization, growth mechanisms, fundamental properties, and applications.* Progress in Materials Science, 2014. **60**: p. 208-337.
108. Song, M.-K., et al., *Nanostructured electrodes for lithium-ion and lithium-air batteries: the latest developments, challenges, and perspectives.* Materials Science and Engineering: R: Reports, 2011. **72**(11): p. 203-252.
109. Kislyuk, V. and O. Dimitriev, *Nanorods and nanotubes for solar cells.* Journal of nanoscience and nanotechnology, 2008. **8**(1): p. 131-148.

110. Yoon, K.H., W.J. Choi, and D.H. Kang, *Photoelectrochemical properties of copper oxide thin films coated on an n-Si substrate.* Thin solid films, 2000. **372**(1-2): p. 250-256.
111. Wang, L., *Preparation and characterization of properties of electrodeposited copper oxide films*. 2006: The University of Texas at Arlington.
112. Rai, B., *Solar Cells: A Review.* Sol. Cells, 1988. **25**: p. 265.
113. Elmahdy, M.M. and A. El-Shaer, *Structural, optical and dielectric investigations of electrodeposited p-type Cu 2 O.* Journal of Materials Science: Materials in Electronics, 2019. **30**: p. 19894-19905.
114. Rahman, A.S., M.A. Islam, and K.M. Shorowordi, *Electrodeposition and characterization of copper oxide thin films for solar cell applications.* Procedia Engineering, 2015. **105**: p. 679-685.
115. Noffke, A.L., et al., *Designing organometallic compounds for catalysis and therapy.* Chemical Communications, 2012. **48**(43): p. 5219-5246.
116. Abbott, J.K., et al., *Synthesis of organometallic compounds*, in *Modern Inorganic Synthetic Chemistry*. 2017, Elsevier. p. 247-277.
117. Allendorf, M.D., et al., *A roadmap to implementing metal–organic frameworks in electronic devices: challenges and critical directions.* Chemistry–A European Journal, 2011. **17**(41): p. 11372-11388.
118. Stavila, V., A.A. Talin, and M.D. Allendorf, *MOF-based electronic and opto-electronic devices.* Chemical Society Reviews, 2014. **43**(16): p. 5994-6010.
119. Liu, J. and C. Wöll, *Surface-supported metal–organic framework thin films: fabrication methods, applications, and challenges.* Chemical Society Reviews, 2017. **46**(19): p. 5730-5770.
120. Falcaro, P., et al., *MOF positioning technology and device fabrication.* Chemical Society Reviews, 2014. **43**(16): p. 5513-5560.
121. Halls, J.E., et al., *Electrochemistry within metal-organic frameworks.* Electrochemistry, 2013. **12**: p. 187-210.
122. Gándara, F., et al., *Porous, conductive metal-triazolates and their structural elucidation by the charge-flipping method.* Chemistry–A European Journal, 2012. **18**(34): p. 10595-10601.
123. Kobayashi, Y., et al., *Conductivity, doping, and redox chemistry of a microporous dithiolene-based metal− organic framework.* Chemistry of Materials, 2010. **22**(14): p. 4120-4122.
124. Marshall, R.J. and R.S. Forgan, *Postsynthetic Modification of Zirconium Metal-Organic Frameworks.* European Journal of Inorganic Chemistry, 2016. **2016**(27): p. 4310-4331.
125. Lin, S., et al., *Electrochemical water oxidation by a catalyst-modified metal–organic framework thin film.* ChemSusChem, 2017. **10**(3): p. 514-522.
126. Hod, I., et al., *Bias-switchable permselectivity and redox catalytic activity of a ferrocene-functionalized, thin-film metal–organic framework compound.* The journal of physical chemistry letters, 2015. **6**(4): p. 586-591.
127. Chauhan, D., et al., *Effect of a metallocene catalyst mixture on CNT yield using the FC-CVD process.* Catalysts, 2022. **12**(3): p. 287.
128. Tamura, K., et al., *Charge/discharge properties of organometallic batteries fabricated with ferrocene–containing polymers.* Macromolecular rapid communications, 2008. **29**(24): p. 1944-1949.
129. Geiger, W.E., *Organometallic electrochemistry: origins, development, and future.* Organometallics, 2007. **26**(24): p. 5738-5765.

130. Kawai, T., C. Iwakura, and H. Yoneyama, *Electrochemical characteristics of poly (vinylferrocene) derivatives for battery application.* Electrochimica acta, 1989. **34**(9): p. 1357-1361.
131. Li, Y., M. Josowicz, and L.M. Tolbert, *Diferrocenyl molecular wires. The role of heteroatom linkers.* Journal of the American Chemical Society, 2010. **132**(30): p. 10374-10382.
132. Sarhan, A.E.-W., Y. Nouchi, and T. Izumi, *Synthesis and electrochemical studies of ferrocene-dithiafulvalenes (Fc-DTF) and 1, 1'-bis (dithiafulvalenyl) ferrocene (DTF-Fc-DTF). An approach towards new conducting organic materials.* Tetrahedron, 2003. **59**(33): p. 6353-6362.
133. Foucher, D.A., B.Z. Tang, and I. Manners, *Ring-opening polymerization of strained, ring-tilted ferrocenophanes: a route to high-molecular-weight poly (ferrocenylsilanes).* Journal of the American chemical society, 1992. **114**(15): p. 6246-6248.
134. Kealy, T.J. and P.L. Pauson, *A new type of organo-iron compound.* Nature, 1951. **168**(4285): p. 1039-1040.
135. Heinze, K. and H. Lang, *Ferrocene · Beauty and Function*. 2013, ACS Publications. p. 5623-5625.
136. Heo, R.W. and T.R. Lee, *Ferrocenophanes with all carbon bridges.* Journal of organometallic chemistry, 1999. **578**(1-2): p. 31-42.
137. Ruiz, J., et al., *First 17− 18− 19-Electron Triads of Stable Isostructural Organometallic Complexes. The 17-Electron Complexes [Fe (C5R5)(arene)] 2+(R= H or Me), a Novel Family of Strong Oxidants: Isolation, Characterization, Electronic Structure, and Redox Properties.* Journal of the American Chemical Society, 1998. **120**(45): p. 11693-11705.
138. Amer, W.A., et al., *Recent progress in the synthesis and applications of some ferrocene derivatives and ferrocene-based polymers.* Journal of Inorganic and Organometallic Polymers and Materials, 2010. **20**: p. 605-615.
139. Kobayashi, Y., T. Hoshi, and J.-i. Anzai, *Glucose and lactate biosensors prepared by a layer-by-layer deposition of concanavalin A and mannose-labeled enzymes: Electrochemical response in the presence of electron mediators.* Chemical and pharmaceutical bulletin, 2001. **49**(6): p. 755-757.
140. Constantinescu, C., et al., *Ferrocene carboxaldehyde thin films grown by matrix-assisted pulsed laser evaporation for non linear optical applications.* Applied Surface Science, 2014. **302**: p. 83-86.
141. Matei, A., et al., *Ferrocene, an old molecule with a bright future: Thin films grown by matrix-assisted pulsed laser evaporation for nonlinear optical applications.* Journal of Organometallic Chemistry, 2014. **751**: p. 638-643.
142. Rong, Y., et al., *Polymers of intrinsic microporosity in electrochemistry: Anion uptake and transport effects in thin film electrodes and in free-standing ionic diode membranes.* Journal of Electroanalytical Chemistry, 2016. **779**: p. 241-249.
143. Cuartero, M., et al., *Electrochemical mechanism of ferrocene-based redox molecules in thin film membrane electrodes.* Electrochimica Acta, 2017. **238**: p. 357-367.
144. Liu, K.-G., et al., *Ultrasonic-assisted fabrication of thin-film electrochemical detector of H2O2 based on ferrocene-functionalized silver cluster.* Ultrasonics Sonochemistry, 2019. **56**: p. 305-312.
145. Bi, H., et al., *Ferrocene Derivatives for Improving the Efficiency and Stability of MA-Free Perovskite Solar Cells from the Perspective of Inhibiting*

Ion Migration and Releasing Film Stress. Advanced Science, 2023. **10**(35): p. 2304790.
146. Liu, Y.-Z., et al., *Elevating the resistive memory from binary to ternary by introducing trialkyl phosphorus into binaphthol/ferrocene cores in their polystyrene composites.* Materials Today Communications, 2022. **33**: p. 105026.
147. Shao, L.-X., et al., *Layer-by-layer growth of ferrocene decorated metal–organic framework thin films and studies of their electrochemical properties.* Applied Surface Science, 2022. **596**: p. 153525.
148. Maheshwari, H., et al., *Selective detection of cysteine at a mesoporous silica film electrode functionalized with ferrocene in the presence of glutathione.* ChemElectroChem, 2020. **7**(9): p. 2095-2101.
149. Chou, S.-Y., et al., *Efficient electrocatalytic H2O2 evolution utilizing electron-conducting molecular wires spatially separated by rotaxane encapsulation.* Applied Catalysis B: Environmental, 2023. **327**: p. 122373.
150. Palfreyman, J.J., *Fabrication and functionalisation of multibit magnetic tags*. 2009, University of Cambridge.
151. De Los Santos Valladares, L., *Study of thin metal films and oxide materials for nanoelectronics applications*. 2012, University of Cambridge.
152. Forster, R.J., et al., *Voltammetry| Overview.* 2019.
153. Valladares, L.D.L.S., et al., *Fabrication of Nanogap Electrodes by Electroless-and Electro-deposition.* Vistas in Nanofabrication, 2012: p. 147.
154. Delcourt-Lancon, A., *Electrochemical analysis supported by macro and microelectrode array*. 2011, Durham University.
155. GUY, O.J., *a Kelly-Ann D. WALKER. Graphene Functionalization for Biosensor Applications.* Silicon Carbide Biotechnology-A Biocompatible Semiconductor for Advanced Biomedical Devices and Applications. 2nd Edition. Elsevier, 2016: p. 1-2.
156. Rezaei, B. and N. Irannejad, *Electrochemical detection techniques in biosensor applications*, in *Electrochemical biosensors*. 2019, Elsevier. p. 11-43.
157. Grossi, M. and B. Riccò, *Electrical impedance spectroscopy (EIS) for biological analysis and food characterization: A review.* Journal of sensors and sensor systems, 2017. **6**(2): p. 303-325.
158. Harrington, G.F. and J. Santiso, *Back-to-Basics tutorial: X-ray diffraction of thin films.* Journal of Electroceramics, 2021. **47**(4): p. 141-163.
159. Herrero, Y.R., K.L. Camas, and A. Ullah, *Characterization of biobased materials*, in *Advanced Applications of Biobased Materials*. 2023, Elsevier. p. 111-143.
160. Luo, Q., *Electron microscopy and spectroscopy in the analysis of friction and wear mechanisms.* Lubricants, 2018. **6**(3): p. 58.
161. Inkson, B.J., *Scanning electron microscopy (SEM) and transmission electron microscopy (TEM) for materials characterization*, in *Materials characterization using nondestructive evaluation (NDE) methods*. 2016, Elsevier. p. 17-43.
162. Nasrollahzadeh, M., et al., *An introduction to nanotechnology*, in *Interface science and technology*. 2019, Elsevier. p. 1-27.
163. Ghisalberti, M. and H. Nepf, *Mass transport in vegetated shear flows.* Environmental fluid mechanics, 2005. **5**: p. 527-551.

164. Jafari, S.M., *Nanoencapsulation of food bioactive ingredients: Principles and applications*. 2017: Academic Press.
165. Undavalli, V.K. and B. Khandelwal, *Impact of alternative fuels and fuel properties on PM emissions*, in *Aviation Fuels*. 2021, Elsevier. p. 71-111.
166. Patrizi, B., et al., *Dioxin and related compound detection: Perspectives for optical monitoring.* International Journal of Molecular Sciences, 2019. **20**(11): p. 2671.
167. Scharifker, B. and G. Hills, *Theoretical and experimental studies of multiple nucleation.* Electrochimica acta, 1983. **28**(7): p. 879-889.
168. Wieckowski, A., E.R. Savinova, and C.G. Vayenas, *Catalysis and electrocatalysis at nanoparticle surfaces*. 2003: cRc Press.
169. Nandiyanto, A.B.D., R. Oktiani, and R. Ragadhita, *How to read and interpret FTIR spectroscope of organic material.* Indonesian Journal of Science and Technology, 2019. **4**(1): p. 97-118.
170. Johns, I., E. McElhill, and J. Smith, *Thermal Stability of Some Organic Compounds.* Journal of Chemical and Engineering Data, 1962. **7**(2): p. 277-281.
171. Ciżman, A., et al., *The effect of Fe on the structure and electrical conductivity of sodium borosilicate glasses.* Physical Chemistry Chemical Physics, 2017. **19**(34): p. 23318-23324.
172. Allegretti, F., et al., *HREELS study of the adsorption mechanism and orientational order of 2-mercaptobenzoxazole on Cu (1 0 0).* Surface science, 2003. **539**(1-3): p. 63-71.
173. Elnady, A. and M. Nasir. *Nested multiband hysteresis current control of master-slave scheme for reliable microgrid*. in *2022 Advances in Science and Engineering Technology International Conferences (ASET)*. 2022. IEEE.
174. Hasan, G.G., et al., *Electrochemical deposition of Ag nanoparticles on ITO-coated glass: effect of different cyclic voltammetry scan rates on Ag deposition.* Ferroelectrics, 2023. **602**(1): p. 121-134.
175. Sun, N., et al., *Ferrocene peapod modified electrodes: preparation, characterization, and mediation of H2O2.* Analytical chemistry, 2006. **78**(17): p. 6050-6057.
176. Emir, G., Y. Dilgin, and R. Apak, *A New Redox Mediator (Cupric-Neocuproine Complex)-Modified Pencil Graphite Electrode for the Electrocatalytic Oxidation of H2O2: A Flow Injection Amperometric Sensor.* ChemElectroChem, 2020. **7**(3): p. 649-658.
177. Althamthami, M., et al., *Improved photocatalytic activity under the sunlight of high transparent hydrophilic Bi-doped TiO2 thin-films.* Journal of Photochemistry and Photobiology A: Chemistry, 2023. **443**: p. 114818.
178. Muraro, P.C.L., et al., *Silver nanoparticles from residual biomass: Biosynthesis, characterization and antimicrobial activity.* Journal of Biotechnology, 2022. **343**: p. 47-51.
179. Mohammed Mohammed, H.A., et al., *A novel biosynthesis of MgO/PEG nanocomposite for organic pollutant removal from aqueous solutions under sunlight irradiation.* Environmental Science and Pollution Research, 2023. **30**(19): p. 57076-57085.
180. da Silva, W.L., et al., *Petrochemical residue-derived silica-supported titania-magnesium catalysts for the photocatalytic degradation of imidazolium ionic liquids in water.* Separation and Purification Technology, 2019. **218**: p. 191-199.

181. Silva, W.L.d., M.A. Lansarin, and C.C. Moro, *Synthesis, characterization and photocatalytic activity of nanostructured TiO2 catalysts doped with metals.* Química Nova, 2013. **36**: p. 382-386.

Appendixes

Hasan, Gamil Gamal, Abdelhamid Khelef, Nacer Chaabia, Hamdi Ali Mohammed, Mohammed Laid Tedjani, and Mohammed Althamthami. "Fabrication and characterization of NFMA/FTO electrochemical thin film by electrodeposition and immersion techniques: An effective detector for H_2O_2 and sunlight-driven MB degradation." *Journal of Photochemistry and Photobiology A: Chemistry* 445 (2023): 115112. https://doi.org/10.1016/J.JPHOTOCHEM.2023.115112

Hasan, Gamil Gamal, Hamdi Ali Mohammed, Mohammed Althamthami, Abdelhamid Khelef, Salah Eddine Laouini, and Souhaila Meneceur. "Synergistic effect of novel biosynthesis SnO_2@ Fe_3O_4 nanocomposite: A comprehensive study of its photocatalytic of Dyes & antibiotics, antibacterial, and antimutagenic activities." *Journal of Photochemistry and Photobiology A: Chemistry* 443 (2023): 114874.

https://doi.org/10.1016/J.JPHOTOCHEM.2023.114874

Hasan, Gamil Gamal, Abdelhamid Khelef, Nacer Chaabia, Mohammed Laid Tedjani, and Mohammed Althamthami. "Electrochemical deposition of Ag nanoparticles on ITO-coated glass: effect of different cyclic voltammetry scan rates on Ag deposition." *Ferroelectrics* 602, no. 1 (2023): 121-134. https://doi.org/10.1080/00150193.2022.2149307

Hasan, Gamil Gamal, Salah Eddine Laouini, Abdelhamid Khelef, Hamdi Ali Mohammed, Mohammed Althamthami, Souhaila Meneceur, Fahad Alharthi, Sohad A. Alshareef, and Farid Menaa. "Efficient treatment of oily wastewater, antibacterial activity, and photodegradation of organic dyes using biosynthesized Ag@ Fe3O4 nanocomposite." *Bioprocess and Biosystems Engineering* 47, no. 1 (2024): 75-90. https://doi.org/10.1007/s00449-023-02946-6

International Conferences:

Synergistic effect of NFMA/Cu_2O deposited on ITO Thin Film by Electrodeposition and Immersion Techniques for degradation Rose bengal from aqueous wastewater.

4th International Conference on Engineering and Applied Natural Sciences November 20-21, 2023 : Konya, Turkey

https://doi.org/10.59287/as-proceedings.325

National Conferences:

Nucleation and Optical studies of ITO/Ag Electrodeposition.

The first national Seminar on Green Chemistry and Natural Products (GCNP’22)